REDUCED-ORDER MODELS FOR ROBUST IDENTIFICATION AND DAMAGE MODELING OF BLISKS

by

Andrew C. Madden

A dissertation submitted in partial fulfillment
of the requirements for the degree of
Doctor of Philosophy
(Mechanical Engineering)
in The University of Michigan
2011

Doctoral Committee:

Associate Professor Bogdan Epureanu, Chair
Professor Gregory M. Hulbert
Professor Nickolas Vlahopoulos
Assistant Professor Kenn R. Oldham
Visiting Research Scholar Matthew P. Castanier

In memory of my grandparents
For giving me part pragmatism, part inspiration

ACKNOWLEDGEMENTS

I would like to express my gratitude to Professor Bogdan Epureanu for serving as my current advisor and chair of my doctoral committee. I would also like to thank Dr. Matthew Castanier who advised me during the first years of my doctoral work. The support, both professionally and personally, from both of my advisors have made this work possible. I would like to thank the other members of my doctoral committee, Professor Hulbert, Professor Oldham, and Professor Vlahopoulos for their valuable comments and suggestions.

I would like to thank the sponsor GE Aviation through the University Strategic Alliance (USA) program, with Dr. Sergio Filippi and Dr. Steve Manwaring as the technical contacts and Dave Bulman as the program manager. I would like to thank Dr. Filippi and the other members of the GE community who have offered their suggestions and guidance for this work.

I would also like to thank the current and former members of the Vibrations and Acoustics Laboratory who have helped me with many fruitful conversations and for their friendship: Geng Zheng, Eric Baik, Jia Li, Soo-Yeol Lee, Zhijiang He, Keychun Park, Sang Heon Song, Olivier Poudou, Joosup Lim, Kiran D'Souza, Andrew Sloboda, Darren Holland, Tian Shen, Sung-Kwon Hong, Chulwoo Jung, Woo Chul Nam, Olguta Marinescu, Jason Rodgers, Anish Joshi, and Niraj Shah. I would especially like to thank Akira Saito who was an important mentor and friend for me. His help, encouragement, and friendship along the way is greatly appreciated.

I would like to thank my parents for their support over the many years. I would also like to thank Lang, Clark and the rest of my family for their support and patience along the way. Finally, I would like to thank the many friends who have made my time in Ann Arbor enjoyable.

TABLE OF CONTENTS

LIST OF FIGURES

Figure

LIST OF TABLES

Table

CHAPTER I

Introduction

1.1 Dissertation Objective

Predicting the dynamic response of complicated structures is important to many engineering fields. One such area is related to engineering of turbomachinery. Turbomachinery contains many stages of integrally bladed disks, or blisks. The distinguishing feature of a blisk is that it is made out of a single piece of material and has no assembled components. Blisks are often subject to small or large mistuning, that is, deviations from the cyclic symmetry of the structure. As a result, these systems can have unpredictable responses in the presence of small or large mistuning and therefore can be exposed to unpredictably high stress levels. Also, these blisks are exposed to harsh environments and an extremely high cycling. As a result, high cycle fatigue failure is of concern and can have devastating consequences, either in the form of costly maintenance or catastrophic failures. This research focuses on both predicting the dynamic response and identification of system parameters of mistuned structures.

Models of blisks are becoming increasingly more complicated and higher accuracy predictions are in demand. The finite element models of industrial blisks can often have millions of degrees of freedom (DOFs). Furthermore, the presence of mistuning in blisks restricts one common technique usage of performing calculations on a sector of the sym-

metric system and then expansion to the full system. Therefore, there is a need to develop high accuracy reduced order models (ROMs) to predict the system response and identify the system parameters. ROMs greatly improve the computational efficiency while maintaining accuracy, thus enabling more rapid design and analysis.

Motivated by these concerns, this work aims to explore reduced order models used to predict the structural dynamics and identify mistuning of complicated systems. This will require both a better understanding of the physics of the systems being studied and the mathematics involved in creating accurate and robust ROMs. Specifically, this work aims to do the following:

- To gain an understanding of why ROMs used to generate predictions do not achieve equally accurate system identification results.
- To develop a robust identification procedure for identifying mistuning in blisks.
- To explore the physics of blisks specifically in higher frequency ranges and understand why current ROMs cannot be used in these ranges to identify mistuning.
- To develop a mistuning identification procedure that can be used in higher frequency ranges.
- To develop a new ROMs that can model both small and large mistuning without incurring large computational costs to generate the ROMs.

1.2 Dissertation Background

1.2.1 Mistuning modeling

Small deviations in the structural properties of the blades in an otherwise cyclically symmetric integrally bladed disk, or blisk, can result in significant changes to the forced

response behavior of the structure. These small blade-to-blade deviations, called mistuning, can arise due to reasons such as manufacturing tolerances, general wear over the life cycle, and damage. Cyclically symmetric blisks do not suffer from localization [1, 2] and therefore the vibrational energy is uniformly distributed among sectors. However, in the presence of only slight mistuning, the system can be subject to localization. Localization caused by mistuning has been shown to significantly increase the forced response for blisks [3]. Ultimately, blisks exposed to extremely high rotating speeds and increase forced response can be subject to high cycle fatigue failure. This can result in costly maintenance or catastrophic failure [4].

Due to mistuning, the cyclic symmetry of the system is destroyed along with the possibility of using efficient cyclic symmetry solvers to predict the vibration response. Early analyses of mistuning focus on small mistuning using lumped parameter models [5–12]. As computational availability increased, reduced order models (ROMs) based on finite element models (FEM) became available. A large body of research exists on constructing ROMs of mistuned blisks based on tuned system and/or component modes. [13–23]. An excellent review on modeling of mistuned bladed disks was provided by Castanier and Pierre [24].

Component mode mistuning (CMM) [23] serves as a methodology to tackle mistuning for much of this work. A CMM model is built by first projecting the mistuned system matrices onto a truncated basis of tuned system modes. Then, the portions of the matrices associated with mistuning (assumed to be only blade DOF) are further projected onto tuned cantilevered blade modes. This has a few key advantages over competing methods. For example, the number of cantilevered blade modes determines the number of mistuning parameters that the system can have because CMM projects mistuning onto cantilevered blade modes. This gives the CMM approach additional flexibility to accurately model

complicated mistuning. Furthermore, CMM has the possibility of modeling mistuning that is not proportional to the mass and stiffness matrices of the tuned system, a significant improvement over other methods.

1.2.2 Robust Mistuning Identification

Several research efforts have focused on the identification of mistuning parameters using experimentally measured system response data. These system-based mistuning identification procedures are critical for the case of blisks (manufactured as a single piece), because the blades cannot be separated from the disk and tested individually. Mistuning identification results can also be used for evaluating manufacturing processes and identifying wear and damage during maintenance checks. Work in this area has ranged from simple lumped parameter models [25, 26] to more advanced approaches requiring information from a FEM [27–40]. Lim *et al.* [36] and Sinha *et al.* [40] present identification techniques that are flexible enough to identify the properties of blisks that are not restricted to proportional mistuning. The difference between these techniques is that the former identifies blade mistuning whereas the latter directly identifies the parameters of the mistuned system.

Sensitivity to the FEM and measurement data and their use in the ROM is important to mistuning identification. Judge *et al.* [27] found that the identified mistuning parameters were sensitive to errors in the FEM or in the measurement data. Later, Lim *et al.* [36] found that the identification results showed especially high sensitivity to errors in the tuned system eigenvalues for the modes used in the ROM. It is noted that CMM based mistuning identification makes use of a least squares solution which can have high residuals in the presence of erroneous information or information that results in ill-conditioning. This can occur if any two basis vectors are too similar, a phenomenon that is possible when

considering a reduced number of physical DOFs due to experimental limitations. Pichot *et al.* [41] presented a mistuning identification procedure where the measured modes were filtered using the best achievable eigenvectors [42] approach in order to reduce the errors that occur in the measurement data.

Work on modeling and identification of mistuning in blisks has made it possible to accurately model blisks at a fraction of the computational cost compared to a full-order finite element analysis. However, these techniques have only been validated for predictions in lower frequency ranges. Most reduced-order modeling methods to date have not addressed the issues specific to mistuning in higher frequency ranges. Many methods are specifically formulated for isolated, lower-frequency families of blade-dominated modes [34], which is a restriction that prevents accurate modeling across all frequency ranges. The exception is the CMM method developed by Lim *et al.* [22,23], which allows different mistuning patterns for different blade-alone modes. This method was validated numerically for a higher frequency range with two overlapping families of blade-dominated modes [23]. However, the CMM-based mistuning identification method [36–38] has only been validated in lower frequency ranges. There are several additional challenges that arise as a result of higher frequency ranges. For example, the topology of the blade motion becomes more complicated, unlike the more uniform blade motion seen at lower frequencies. Considering the need to gather experimental data for mistuning identification techniques, extra emphasis is placed on optimally choosing the locations on the blade where measurements should be taken. Also, as the blade motion is less uniform, capturing mistuning associated with physical parameter variations localized in a small portion of the blade is sensitive to the modes used in the ROMs and to the specific points where measurements are collected. Furthermore, isolated blade mode families of high modal density no longer exist. In high frequency ranges, the existence of these regions is a key in obtaining simple ROMs to be

used for the inverse problem in the low frequency ranges because these regions are quite sensitive to parameter variations in the system. The absence of these regions in the high frequency ranges increases the need to strategically select a ROM and measurement data that offers sensitivity to mistuning.

1.2.3 Modeling of Large Mistuning and Damage

Accurate predictions of the structural dynamics of turbomachinery blisks is needed to ensure reliability and prevent high cycle fatigue failure [4]. Modeling blisks using full order FEMs is inefficient, especially in the presence of mistuning because these models can have extremely high numbers of DOFs. Mistuning can be small or large deviations in what is otherwise usually a cyclically symmetric blisk. It is often desirable to consider small mistuning from a probabilistic perspective, thus making the solution of full-order FEMs restrictive. Therefore, work in this area focuses mainly on the development of ROMs to approximate the full-order FEM. Early work in blisk modeling focused primarily on small mistuning. Various efficient approaches for reduced-order modeling of blisks with small mistuning have been developed [13–23]. The other category of mistuning is large mistuning. The distinction between large and small mistuning is that large mistuning cannot be accurately modeled by only a change in blade alone frequencies.

Some work has been done for developing ROMs for blisks with large mistuning. Lim *et al.* [22] developed a modeling technique to encompass both small and large mistuning. Those ROMs use tuned modes and virtual mistuned components in a component mode synthesis (CMS) [43] (hybrid interface) technique. The resulting basis consists of a truncated set of tuned normal modes, tuned-system attachment modes, and constraint modes for the mistuning components. However, this method results in prohibitively large models. Following their work, an approach to address large mistuning specifically in order

to reduce the model size was proposed [44] . This method projects the blisk dynamics onto a basis of tuned system modes compensated using quasi-static modes according to a mode acceleration approach. The models obtained by this approach are much smaller, but they do not consider small, random mistuning. Ganine *et al.* [45] added the small, random mistuning to the static mode compensation (SMC) approach in a similar manner to CMM [23]. This was followed by a study of the convergence properties of the SMC technique and a suggestion for a new technique based on a Jacobi-Davidson correction of the modes [46] . It was noted that SMC is most appropriate only when modes are closely spaced and the FEM is not too large, whereas the Jacobi-Davidson had better convergence for large scale FEM and regions where mode family interaction is important. A unique approach was suggested by Sinha [47, 48] where tuned modes are chosen for the basis based on proper orthogonal decomposition (POD) features. The ROM size generated by that approach can be larger than SMC based ROMs since it is the product of the number of tuned modes and the number of POD features, but the approach allows for the possibility to model random large mistuning.

Mbaye *et al.* [49, 50] modeled the dynamics of blisks with intentional geometric mistuning with the possibility of adding random mistuning [51]. In this approach, cyclic symmetry analysis is applied to each individual sector to compute modes to be used in the basis for reduction. Cyclic symmetry modes are then strategically assembled according to the physical DOFs corresponding to each sector to build up each full mode shape. To do this, it was necessary to introduce a modal scale factor to match phases and ultimately modify the modes of each sector before compatibility was enforced on the interface. This unique approach offers a convenient and efficient way to model a system that is intentionally geometrically mistuned.

The work of Mbaye *et al.* [49] focused on intentional mistuning, but lacked the gener-

alization need to model all forms of large mistuning. The approach by Mbaye *et al.* [49] used a modal scaling factor computed using the inner product between a nominal sector and the sectors of the actual system. This factor cannot be directly applied to a system having missing material because the number of DOFs do not match from sector to sector. For systems with large bends, this factor could also lead to a false phase matching. This is because the actual location of the DOFs between adjacent sectors are different. Also, each of the cyclic modes for each sector are assembled for the same mode without additional normalization. Hence, it is possible that the basis could be insufficient for certain systems which have large parameter changes. Such an example is a case where only the modulus of elasticity is changed for one entire sector. In this particular case, the mode shapes for the modified sector would be the same as the nominal tuned sector. This would make the basis in this approach precisely the tuned system modes. However, it is well known that the mistuned system with a large enough change in modulus of elasticity cannot be modeled using tuned system modes [23].

1.3 Dissertation Outline

Chapter II introduces a procedure for constructing a ROM referred to as an inverse ROM (or IROM) that is well suited for solving the mistuning identification inverse problem. First, a quantitative metric is defined to characterize and rank the tuned system modes with respect to their suitability for constructing IROMs. This metric is based on both satisfying the assumptions made in the CMM ROM [23] and also on the sensitivity of the modes to mistuning. This metric is then used to select the order of importance of the tuned mode shapes to be included in the IROM. Then, the direct problem is solved using a larger direct ROM (or DROM) with prescribed mistuning in order to interrogate and validate the performance of various IROMs as modes are added. It is demonstrated that the use

of DROM-generated surrogate data enables the rapid automatic construction of suitable IROMs and improves the overall accuracy and robustness of mistuning identification.

Chapter III studies the key challenges of mistuning identification in higher frequency regimes. Procedures are presented and evaluated for reduced-order modeling and mistuning identification of blisks at frequency ranges beyond the first few families of blade-dominated modes. First, a discussion is offered as to why it is unique to CMM-based ROMs that one might identify mistuning in higher frequency ranges and how that has important implications on the accuracy of predictions. Next, an iterative measurement point selection technique is introduced to strategically select measurement points that are sensitive to mistuning but insensitive to noise. To do this, the effective independence distribution vector (EIDV) [52, 53] is used to evaluate measurement points. These are used in an advanced surrogate data algorithm which simultaneously considers the best measurement points for each IROM to be evaluated. It is shown that mistuning patterns can be identified for higher mode families, and the mistuning pattern for each family is generally unique when the physical mistuning is not uniform throughout each blade. Finally, given unique mistuning patterns that have been identified, a formulation is introduced which can relate these values to physical parameter variations in discrete locations of the blades.

Chapter IV introduces a Craig-Bamptom component mode synthesis (CB-CMS) [54] ROM for modeling large mistuning in blisks. It is first demonstrated that using tuned system modes as a basis for a system with large mistuning is insufficient. Then a CB-CMS ROM is introduced where each sector of the blisk is considered to be a component and the component interfaces are at sector-sector boundaries. This was demonstrated to be an accurate basis for predicting the modes of the nominal rogue system. In addition, a secondary reduction was suggested. This is also based on using CB-CMS and assuming that some of the components from the first reduction can be combined. This provides

additional reduction of the ROM dimensions, but allows for components associated with the rogue sectors to remain unreduced. This makes it possible to rapidly exchange rogue blades and generate a new ROM to be considered. Ultimately, the CB-CMS modes are expanded to predict the full nominal rogue modes, which serve as the basis for projecting the mistuned system. Finally, an extended CMM [23] procedure is used to add small mistuning. It is extended by allowing the rogue DOFs from the nominal rogue system modes to be projected onto rogue cantilevered blade modes instead of tuned cantilevered blade modes.

Chapter V introduces a new reduced order modeling approach for both large and small mistuning. First, a novel basis which makes use of a pristine, rogue, interface modal expansion (PRIME) is introduced. The PRIME basis is a new basis composed of modes computed only from cyclic symmetry analyses. By strategically projecting a finite element model from the physical space onto the new basis, it is possible to accurately and efficiently model large mistuning. It is then demonstrated that it is possible to generate this ROM using only sector level quantities and therefore can be applied to highly refined, realistic models of industrial size. In addition, it is demonstrated that the new method can account for both large and small mistuning simultaneously using an extension of the component mode mistuning approach [23]. Finally, the PRIME basis is modified to further reduce the system and improve the conditioning of the basis.

Chapter VI offers a brief summary of contributions of the work in this dissertation, and suggests ideas for future work.

CHAPTER II

Reduced-Order Model Construction Procedure for Robust Mistuning Identification of Blisks

2.1 Introduction

Small deviations among the structural properties of the blades in an otherwise cyclically symmetric bladed disk can result in significant changes to the forced response behavior of the structure. These small blade-to-blade deviations, called mistuning, can arise due to reasons such as manufacturing tolerances, general wear over the life cycle, and damage. Mistuning has been shown to increase the forced response for a bladed disk which can be a concern for high cycle fatigue. [4] Furthermore, due to mistuning, the cyclic symmetry of the system is destroyed along with the possibility of using efficient cyclic symmetry solvers to predict the vibration response. As a result, a large body of research exists on constructing reduced-order models (ROMs) of mistuned bladed disk vibration based on tuned system and/or component modes. [14, 16–18, 21–23].

With capabilities to model and study mistuning of bladed disks in place, several recent research efforts have focused on the identification of the mistuning parameters using experimentally measured system response data. Such system-based mistuning identification procedures are essential for the case of bladed disks manufactured as a single piece (called blisks), because the blades cannot be separated from the disk and tested individually. Mis-

tuning identification results can also be used for evaluating manufacturing processes and identifying wear and damage during maintenance checks. Work in this area has ranged from simple lumped parameter models [25, 26] to more involved reduced-order modeling techniques [27–30, 32–36, 38, 39]. Judge *et al.* [27] found that the identified mistuning parameters were sensitive to errors in the finite element model (FEM) or measurement data. Later, Lim *et al.* [36] found that the identification results showed especially high sensitivity to errors in the tuned system eigenvalues for the modes used in the ROM.

Sensitivity to the FEM and measurement data and their use in the ROM is the subject of this work. Pichot *et al.* [41] recently presented a mistuning identification procedure where the measured modes were filtered using the Best Achievable Eigenvectors [42] approach in order to reduce the errors that occur in the measurement data. The work presented here considers the component mode mistuning (CMM) approach to mistuning identification [36,38] and explores ways to enhance the procedure given the modeling technique and the limitations of the experimental portion of the approach. In order to select tuned system normal modes that will best fit the assumptions of the CMM approach, a parameter based on cantilevered blade participation factors and blade-disk interface motion is introduced. Using modes selected as favorable for the ROM according to this parameter can result in increased accuracy for the mistuning identification procedure. In this work, a procedure is introduced for constructing a ROM referred to as an inverse ROM (or IROM) that is well suited for solving the mistuning identification inverse problem. Also, representing the mode shapes using a limited number of measured degrees of freedom (DOF) is accounted for because of the likely possibility that the corresponding modal matrix is rank deficient. Limitations for the types of mode shapes that can be used are discussed. Finally, a method is presented that can be used to determine a suitable IROM size. By using an assumed mistuning pattern, a forward problem can be formulated and used to generate surrogate

data, which are then used to identify the mistuning in the inverse problem and thus assess the accuracy of the IROM.

2.2 Theory

2.2.1 Background: Mistuning Identification and Model Updating Based on the CMM Method

Consider the equations of motion in the frequency domain for an elastic structure with structural damping, expressed as

$$-\omega^2 \mathbf{M}\mathbf{x} + (1 + j\gamma)\,\mathbf{K}\mathbf{x} = \mathbf{f}, \tag{2.1}$$

where ω is the response frequency, γ is the structural damping constant, and $\mathbf{f}$ is harmonic forcing. If the structure of interest is a mistuned bladed disk or blisk, the CMM method developed by Lim *et al.* [22, 23] can be implemented. The CMM procedure treats the tuned system as a free-interface component and the mistuned portions of the system are treated as fixed-interface components. Using component mode synthesis (CMS) [43, 55], the following is obtained for the tuned system

$$\begin{aligned}
\mu^s &= \begin{bmatrix} \mathbf{I} & \boldsymbol{\Phi}^{s^T}\mathbf{M}^s\boldsymbol{\Psi}^s \\ \boldsymbol{\Psi}^{s^T}\mathbf{M}^s\boldsymbol{\Phi}^s & \boldsymbol{\Psi}^{s^T}\mathbf{M}^s\boldsymbol{\Psi}^s \end{bmatrix}, \\
\kappa^s &= \begin{bmatrix} \boldsymbol{\Lambda}^s & \boldsymbol{\Phi}^{s^T}\mathbf{K}^s\boldsymbol{\Psi}^s \\ \boldsymbol{\Psi}^{s^T}\mathbf{K}^s\boldsymbol{\Phi}^s & \boldsymbol{\Psi}^s_A \end{bmatrix}, \\
\mathbf{x}^s &= \begin{bmatrix} \boldsymbol{\Phi}^s_O & \boldsymbol{\Phi}^s_O \\ \boldsymbol{\Phi}^s_A & \boldsymbol{\Phi}^s_A \end{bmatrix} \begin{Bmatrix} \mathbf{p}^s_\Phi \\ \mathbf{p}^s_\Psi \end{Bmatrix},
\end{aligned} \tag{2.2}$$

where μ^s and κ^s are reduced mass and stiffness matrices of the tuned system, $\mathbf{p}^s_\Phi$ and $\mathbf{p}^s_\Psi$ are modal coordinates, O and A refer to omitted and active (where mistuning exists) DOF, respectively, and s denotes the tuned system. Also, $\boldsymbol{\Phi}^s$ and $\boldsymbol{\Psi}^s$ are the tuned system normal

modes and constraint modes corresponding to mistuned DOF, respectively, while $\mathbf{M}^s$ and $\mathbf{K}^s$ are the tuned mass and stiffness matrices. The mistuned portion is represented only as constraint modes because all of the mistuning DOF are considered interface DOF so that

$$\begin{aligned} \mu^\delta &= \mathbf{M}^\delta, \\ \kappa^\delta &= \mathbf{K}^\delta, \\ \mathbf{x}^\delta &= \mathbf{x}^\delta_\Psi. \end{aligned} \tag{2.3}$$

Here, δ denotes the mistuned portion of the system, and Ψ indicates the modal coordinates associated with the interface DOF. The CMS synthesized equations follow as

$$\begin{aligned} \mu^{syn}_{CMS} &= \mu^s + \begin{bmatrix} \boldsymbol{\Phi}^{s^T}_A \mathbf{M}^\delta \boldsymbol{\Phi}^s_A & \boldsymbol{\Phi}^{s^T}_A \mathbf{M}^\delta \boldsymbol{\Psi}^s_A \\ \boldsymbol{\Psi}^{s^T}_A \mathbf{M}^\delta \boldsymbol{\Phi}^s_A & \boldsymbol{\Psi}^{s^T}_A \mathbf{M}^\delta \boldsymbol{\Psi}^s_A \end{bmatrix}, \\ \kappa^{syn}_{CMS} &= \kappa^s + \begin{bmatrix} \boldsymbol{\Phi}^{s^T}_A \mathbf{K}^\delta \boldsymbol{\Phi}^s_A & \boldsymbol{\Phi}^{s^T}_A \mathbf{K}^\delta \boldsymbol{\Psi}^s_A \\ \boldsymbol{\Psi}^{s^T}_A \mathbf{K}^\delta \boldsymbol{\Phi}^s_A & \boldsymbol{\Psi}^{s^T}_A \mathbf{K}^\delta \boldsymbol{\Psi}^s_A \end{bmatrix}, \\ \mathbf{p}^{syn}_{CMS} &= \begin{Bmatrix} \mathbf{p}^s_\Phi \\ \mathbf{p}^s_\Psi \end{Bmatrix}. \end{aligned} \tag{2.4}$$

Next, one assumes that the tuned system modes used in the ROM have natural frequencies from within small frequency band. According to work by Yang and Griffin [18, 56], this suggests that the mistuned normal modes are also in a small frequency band and therefore can be represented by a small set of tuned system normal modes in the frequency range of interest. This implies that other normal modes and static modes can be ignored. Equation 2.4 leads to a reduced order formulation expressed as

$$\begin{aligned} \mu^{syn} &= \mathbf{I} + \boldsymbol{\Phi}^{s^T}_A \mathbf{M}^\delta \boldsymbol{\Phi}^s_A, \\ \kappa^{syn} &= \boldsymbol{\Lambda}^s + \boldsymbol{\Phi}^{s^T}_A \mathbf{K}^\delta \boldsymbol{\Phi}^s_A, \\ \mathbf{p}^{syn} &= \mathbf{p}^s_\Phi = \mathbf{p}. \end{aligned} \tag{2.5}$$

Combining Eq. 2.1 with Eq. 2.5 and neglecting mass mistuning ($\mathbf{M}^{\delta}$) yields

$$-\omega^2\mathbf{p} + (1+j\gamma)\left[\mathbf{\Lambda}^s + \mathbf{\Phi}^{s^T}\mathbf{K}^{\delta}\mathbf{\Phi}^s\right]\mathbf{p} = \mathbf{\Phi}^{s^T}\mathbf{f}. \tag{2.6}$$

In Lim *et al.* [36, 37], an additional term was added to this equation to account for the difference between the parent tuned system FEM and the virtual tuned system of an actual bladed disk. This term allows the tuned FEM to be updated using the mistuning procedure in order to more closely match the tuned portion of the actual bladed disk being examined. Adding this term to Eq. 2.6, one obtains

$$\begin{aligned} -\omega^2\mathbf{p} + (1+j\gamma)\left[\mathbf{\Lambda}^s + \mathbf{\Phi}^{s^T}\left(\mathbf{K}^{\delta,s} + \mathbf{K}^{\delta}\right)\mathbf{\Phi}^{\mathbf{s}}\right]\mathbf{p} &= \mathbf{\Phi}^{s^T}\mathbf{f}, \\ -\omega^2\mathbf{p} + (1+j\gamma)\left[\mathbf{\Lambda}^s + \mathbf{\Lambda}^{\delta,s} + \mathbf{\Phi}^{s^T}\mathbf{K}^{\delta}\mathbf{\Phi}^s\right]\mathbf{p} &= \mathbf{f}^s, \end{aligned} \tag{2.7}$$

where $\mathbf{\Lambda}^{\delta,\mathbf{s}}$ is the matrix of deviations of the system eigenvalues from those assumed, and $\mathbf{K}^{\delta,\mathbf{s}}$ is the deviation of the nominal tuned system stiffness matrix from that of the actual tuned system. The term $\mathbf{\Phi}^{s^T}\mathbf{K}^{\delta}\mathbf{\Phi}^s$ corresponds to the mistuned portion of the stiffness matrix. It should be noted that this term is not decoupled/diagonalized using this modal decomposition. In order to decouple this portion of the equation and to further reduce the model, the blade portion of the system normal modes, $\mathbf{\Phi}^s$ is represented using a basis of cantilevered blade normal modes denoted by $\mathbf{\Phi}^{cb}$. Furthermore, in these coordinates, the off-diagonal terms are considered negligible [37]. Assuming that $\mathbf{\Phi}^s = \mathbf{\Phi}^{cb}\mathbf{q}$ (where $\mathbf{q}$ are participation factors between the cantilevered blade modes and the blade portion of the tuned system mode), Eq. 2.7 can be written as

$$\begin{aligned} -\omega^2\mathbf{p} + (1+j\gamma)\left[\mathbf{\Lambda}^s + \mathbf{\Lambda}^{\delta,s} + \mathbf{q}^T\mathbf{\Phi}^{cb^T}\mathbf{K}^{\delta}\mathbf{\Phi}^{cb}\mathbf{q}\right]\mathbf{p} &= \mathbf{f}^s, \\ -\omega^2\mathbf{p} + (1+j\gamma)\left[\mathbf{\Lambda}^s + \mathbf{\Lambda}^{\delta,s} + \mathbf{q}^{\mathrm{T}}\mathbf{\Lambda}^{\delta,cb}\mathbf{q}\right]\mathbf{p} &= \mathbf{f}^s. \end{aligned} \tag{2.8}$$

Eq. 2.8 can be rearranged as follows

$$(1+j\gamma)\left[\mathbf{\Lambda}^{\delta,s}+\mathbf{q}^T\mathbf{\Lambda}^{\delta,cb}\mathbf{q}\right]\mathbf{p}=\mathbf{f}^s+\omega^2\mathbf{p}-(1+j\gamma)\,\mathbf{\Lambda}^s,$$

or

$$(1+j\gamma)\left[\mathbf{\Lambda}^s\left(\mathbf{\Lambda}^{s^{-1}}\mathbf{\Lambda}^{\delta,s}\right)+\mathbf{q}^T\mathbf{\Lambda}^{cb}\left(\mathbf{\Lambda}^{cb^{-1}}\mathbf{\Lambda}^{\delta,cb}\right)\mathbf{q}\right]\mathbf{p}=\mathbf{f}^s+\omega^2\mathbf{p}-(1+j\gamma)\,\mathbf{\Lambda}^s. \quad (2.9)$$

Since $\mathbf{p}$ is a complex quantity, it can be written as $\mathbf{p}=\mathbf{p}_r+j\mathbf{p}_i$. Substituting this into Eq. 2.9 and using $(1+j\gamma)\,(\mathbf{p}_r+j\mathbf{p}_i)=(\mathbf{p}_r-\gamma\mathbf{p}_i)+j\,(\mathbf{p}_i+\gamma\mathbf{p}_r)$ yields

$$\begin{aligned}\left[\mathbf{\Lambda}^s\left(\mathbf{\Lambda}^{s^{-1}}\mathbf{\Lambda}^{\delta,s}\right)+\mathbf{q}^T\mathbf{\Lambda}^{cb}\left(\mathbf{\Lambda}^{cb^{-1}}\mathbf{\Lambda}^{\delta,cb}\right)\mathbf{q}\right]\left[(\mathbf{p}_r-\gamma\mathbf{p}_i)+j\,(\mathbf{p}_i+\gamma\mathbf{p}_r)\right]=\\ \mathbf{f}^s+\omega^2\,(\mathbf{p}_r+j\mathbf{p}_i)-\mathbf{\Lambda}^s\left[(\mathbf{p}_r-\gamma\mathbf{p}_i)+j\,(\mathbf{p}_i+\gamma\mathbf{p}_r)\right].\end{aligned} \quad (2.10)$$

Eq. 2.10 can be split into two equations corresponding to real and imaginary parts as

$$\begin{aligned}\mathbf{\Lambda}^s\left(\mathbf{\Lambda}^{s^{-1}}\mathbf{\Lambda}^{\delta,s}\right)(\mathbf{p}_r-\gamma\mathbf{p}_i)+\mathbf{q}^T\mathbf{\Lambda}^{cb}\left(\mathbf{\Lambda}^{cb^{-1}}\mathbf{\Lambda}^{\delta,cb}\right)\mathbf{q}\,(\mathbf{p}_r-\gamma\mathbf{p}_i) &= \\ \mathbf{f}^s+\omega^2\mathbf{p}_r-\mathbf{\Lambda}^s\,(\mathbf{p}_r-\gamma\mathbf{p}_i)\,,& \\ \underbrace{\mathbf{\Lambda}^s}_{\mathbf{a}_{c1}}\left(\mathbf{\Lambda}^{s^{-1}}\mathbf{\Lambda}^{\delta,s}\right)\underbrace{(\mathbf{p}_i+\gamma\mathbf{p}_r)}_{\mathbf{a}_{c2}}+\underbrace{\mathbf{q}^T\mathbf{\Lambda}^{cb}}_{\mathbf{a}_{s1}}\left(\mathbf{\Lambda}^{cb^{-1}}\mathbf{\Lambda}^{\delta,cb}\right)\underbrace{\mathbf{q}\,(\mathbf{p}_i+\gamma\mathbf{p}_r)}_{\mathbf{a}_{s2}} &= \\ \underbrace{\omega^2\mathbf{p}_i-\mathbf{\Lambda}^s\,(\mathbf{p}_i+\gamma\mathbf{p}_r)}_{\mathbf{b}}.&\end{aligned} \quad (2.11)$$

The diagonal matrices associated with quantities to be identified are organized into column vectors and the rest of the equation is reshaped accordingly. The final matrix equation is represented by

$$\begin{bmatrix}\mathbf{A}_c & \mathbf{A}_s\end{bmatrix}\begin{bmatrix}\mathbf{d}^{cyc}\\ \mathbf{d}^{mist}\end{bmatrix}=\mathbf{b}, \quad (2.12)$$

where $\mathbf{d}^{cyc}=\mathrm{diag}\left[\mathbf{\Lambda}^{s-1}\mathbf{\Lambda}^{\delta,s}\right]$, $\mathbf{d}^{mist}=\mathrm{diag}\left[\mathbf{\Lambda}^{cb^{-1}}\mathbf{\Lambda}^{\delta,cb}\right]$, while matrices $\mathbf{A}_c$ and $\mathbf{A}_s$ are comprised of a reorganized version of $\mathbf{a}_{c1}$ and $\mathbf{a}_{c2}$, and of $\mathbf{a}_{s1}$ and $\mathbf{a}_{s2}$.

2.2.2 Selection Ratio (SR)

The CMM approach to mistuning identification presented in the previous section assumes that the system modes have certain properties typically present in blisks in frequency ranges with high modal density and blade-dominated motion. Therefore, a parameter called the selection ratio is introduced here to categorize modes according to how closely they match the assumptions and thereby how well they model the system.

One assumption is that the blade motion in the system modes of interest can be represented using a linear combination of cantilevered blade modes, that is $\mathbf{\Phi}^s = \mathbf{\Phi}^{cb}\mathbf{q}$. In order to check this assumption, the participation of the cantilevered blade normal mode(s) in the current system normal mode is computed. The participation factor with respect to the stiffness matrix for each blade in the system forms the matrix

$$\mathbf{q}_{\Phi}^{cb} = (\mathbf{F}\otimes\mathbf{I}) \underset{h=1,\ldots,P}{\tilde{\mathbf{B}}\mathbf{diag}} \left[\tilde{\mathbf{q}}_h^{cb}\right], \tag{2.13}$$

where $\underset{h=1,\ldots,P}{\tilde{\mathbf{B}}\mathbf{diag}}[\cdot]$ indicates a pseudo-block diagonal matrix, $\mathbf{F}$ denotes the real-valued Fourier matrix, and

$$\tilde{\mathbf{q}}_h^{cb} = \left[\mathbf{\Lambda}^{cb}\right]^{-1} \left(\mathbf{\Phi}^{cb^T}\mathbf{K}^{cb}\mathbf{\Phi}^s\right) \tag{2.14}$$

is the participation of the cantilevered blade normal modes in the cyclic system normal mode for harmonic h [22]. The matrix $\mathbf{\Lambda}^{cb}$ contains the cantilevered blade eigenvalues and the matrix $\mathbf{K}^{cb}$ is the stiffness matrix for the cantilevered blade. Large participation factors for each blade indicate that the motion of the blade in the system normal mode is well represented by the motion of the cantilevered blade normal mode and would be an advantageous choice to use in the ROM for the mistuning problem.

A second assumption in the CMM formulation of the mistuning identification problem is that the displacements at the interface between the blade and the disk are small for the system modes used in the ROM. These displacements can be written as $\mathbf{\Phi}^{s,\Gamma}$, where Γ

denotes the boundary between the blades and the disk. If this motion is small relative to the motion of the blades for a given system normal mode, then this mode is a favorable choice for the IROM used for mistuning identification.

Using these two assumptions, a new criterion is formed to effectively evaluate the candidate system normal modes for the IROM used for mistuning identification. This criterion, called the Selection Ratio (SR), is defined as

$$SR_j = \frac{\|\mathbf{q}_{\Phi,j}^{cb}\|}{\|\mathbf{\Phi}_j^{s,\Gamma}\|}, \tag{2.15}$$

where j denotes the j^{th} system normal mode. This parameter accounts for the two assumptions inherent to the CMM formulation of the mistuning identification problem that have been identified as important for the mistuning identification procedure. System normal modes with large SR values agree favorably with both of the noted CMM assumptions and therefore would be good candidates for the IROM used for mistuning identification.

Although the SR was derived specifically for the CMM approach to mistuning identification, it has a more general interpretation as well. For solving the mistuning identification problem, which is an inverse problem, the ROM should ideally contain only modes that show sensitivity to mistuning. In other words, any mode of the tuned system that would not be changed much by the mistuning is not helpful for solving the mistuning identification problem. Now, consider that the numerator of the SR is related to how strongly a change in a cantilevered blade eigenvalue (i.e., mistuning) affects the system eigenvalue, and the denominator of the SR is related to the strength of the blade-to-disk (and thus blade-to-blade) coupling. Thus, the SR is essentially a mistuning-to-coupling ratio for each system mode. It has been shown by Hodges [2] that the degree of mode localization increases monotonically with an increase in the mistuning-to-coupling ratio. Therefore, the SR is a metric that provides a quantitative assessment of the sensitivity of each system mode to

blade mistuning. It is believed that similar metrics could be used with other mistuning identification techniques.

2.2.3 Physical to Modal Transformation

The CMM approach to mistuning transforms the analysis from physical to modal coordinates in order to reduce the model size. In general, consider the transformation from physical coordinates $\mathbf{x}$ to modal coordinates $\mathbf{p}$ expressed as

$$\mathbf{x} = \mathbf{\Phi}^s \mathbf{p}. \tag{2.16}$$

In order to reduce the model size, the matrix of tuned normal mode shapes $\mathbf{\Phi}^s$ is truncated. Typically, this truncation simply depends upon the frequency range of interest. The physical coordinates and tuned normal mode shapes are known, and the modal coordinates must first be found from Eq. 2.16, which is a least squares problem (since $\mathbf{\Phi}^s$ is truncated).

Measuring very many points per blade is prohibitively expensive. Hence, the mistuning identification procedure is based on experimentally measuring the vibration at only a few points on each blade. These measurement points also correspond to the DOF kept in the modal matrix used for the entire procedure. In this work, the measurement points are chosen using the Effective Independent Distribution Vector (EIDV) procedure introduced by Penny *et al.* [53]. Using a selected basis of tuned system normal modes, the EIDV algorithm selects DOF from a candidate set that will result in the modes being most distinguishable. It has been shown that the mistuning pattern can be effectively identified using as few as one point per blade [39]. Such a restrictive limit on the number of measured points introduces additional restrictions on the modes that can be used in the IROM. To correctly solve for $\mathbf{p}$ using Eq. 2.16, the number of measured DOF on the structure must be greater than or equal to the number of tuned system normal modes. Otherwise, the modal matrix, $\mathbf{\Phi}^s$, with the reduced number of DOF is rank deficient and that can adversely affect

the mistuning identification results.

It should be noted that the modal matrix may become rank deficient even when it has more measurement points than system normal modes, i.e., in cases where multiple system normal modes cannot be distinguished with the given set of measurement points. An example of such a situation occurs in the case when only one point per blade is measured and different tuned system normal modes having the same number of nodal diameters are kept in the IROM. In this case, only one point is not enough to distinguish the modes with the same nodal diameter content, and therefore the modal matrix is rank deficient. In such a case, more DOF per blade must be used to achieve a modal matrix with full rank.

2.2.4 Solution of Known Mistuned Eigenvalue Problem to Generate Numerical Results

Sections 2.2 and 2.2 discussed ways of evaluating tuned system normal modes that are used as a basis for the mistuning identification procedure. With experience, a modeler could choose an appropriate ROM for the mistuning identification problem. In order to increase robustness and reduce the modeling expertise required to build a ROM for performing mistuning identification, a procedure to automatically construct an appropriate IROM is presented next.

Consider Eq. 2.8. Lim [37] suggested that, if damping is small and measurements are taken at resonant frequencies, then $\mathbf{f}^s$ and γ can be set to zero. This results in

$$-\omega^2\mathbf{p} + \left[\mathbf{\Lambda}^s + \mathbf{\Lambda}^{\delta,s} + \mathbf{q}^{\mathrm{T}}\mathbf{\Lambda}^{\delta,cb}\mathbf{q}\right]\mathbf{p} = \mathbf{0}, \tag{2.17}$$

which can be viewed as an eigenvalue problem with ω as the eigenvalue and $\mathbf{p}$ as the eigenvector.

Here, it is suggested to first generate a blade stiffness mistuning pattern, $\mathbf{\Lambda}^{\delta,cb}_{gen}$, and the cyclic model updating pattern, $\mathbf{\Lambda}^{\delta,s}_{gen}$. It should be noted that the normalization of

the eigenvalue changes by the nominal eigenvalues typically associated with mistuning has been dropped for convenience. At this point, the eigenvalue problem is solved for $\mathbf{p}$ using the generated mistuning pattern, $\mathbf{\Lambda}_{gen}^{\delta,cb}$ and $\mathbf{\Lambda}_{gen}^{\delta,s}$. Note that the values of $\mathbf{p}$ must be perturbed in order to avoid a trivial solution where any IROM will give accurate results for the mistuning parameters. The solutions, ω and $\mathbf{p}$, are then used as surrogate data in Eq. 2.17 (inverse problem) where the blade stiffness mistuning, $\mathbf{\Lambda}^{\delta,cb}$, and the cyclic model updating, $\mathbf{\Lambda}^{\delta,s}$, are no longer considered known. This formulation represents the typical mistuning identification (inverse) problem, which can be solved for the mistuning parameters denoted by $\mathbf{\Lambda}_{id}^{\delta,cb}$ and $\mathbf{\Lambda}_{id}^{\delta,s}$. Of course, an exact identification gives $\mathbf{\Lambda}_{id}^{\delta,cb} = \mathbf{\Lambda}_{gen}^{\delta,cb}$ and $\mathbf{\Lambda}_{id}^{\delta,s} = \mathbf{\Lambda}_{gen}^{\delta,s}$. Here, gen stands for generated mistuning parameters that are used to solve the direct problem, and id stands for the mistuning parameters identified in the inverse procedure.

With perturbed values of $\mathbf{p}$, different IROMs can be evaluated by comparing the generated mistuning parameters with those solved by the mistuning identification procedure. By generating a mistuning pattern and solving for surrogate measurement data as suggested above, a mistuning pattern can be identified using the IROM. An error can be associated with the difference between the known and the identified values as $\| \mathbf{\Lambda}_{gen}^{\delta,cb} - \mathbf{\Lambda}_{id}^{\delta,cb} \|_2$ and $\| \mathbf{\Lambda}_{gen}^{\delta,s} - \mathbf{\Lambda}_{id}^{\delta,s} \|_2$ for the blade stiffness mistuning and the cyclic modeling error. Using these error metrics, the effectiveness of various IROMs for identifying mistuning parameters can be evaluated.

2.3 Effect of IROM on Mistuning Parameter Identification

It is not necessarily simple to select the best IROM for the identification of mistuning parameters. Certain modes are less compatible with the assumptions made in the CMM formulation of the mistuning identification procedure. As mentioned in Section 2.2, a

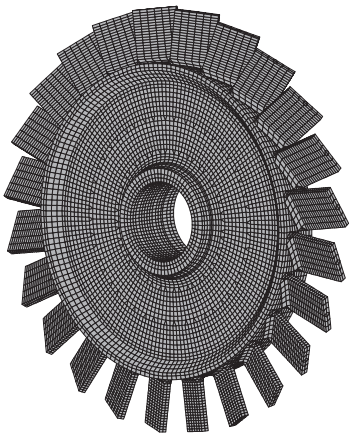

Figure 2.1: FEM of the blisk with 24 blades.

method of evaluating the suitability of various modes for the IROM has been developed. Also, the limited number of measurement points used for obtaining forced response data (which also corresponds to the DOF used to represent the tuned system normal modes in the IROM) has a significant impact on which modes should be selected for the mistuning identification procedure.

In this work, we use a 24-bladed disk (shown in Fig. 2.1) for validations. Only the first flexural cantilevered blade mode is used in the mistuning procedure, and the candidate tuned system normal modes come from the 0-5000 Hz frequency range, which envelopes the first flexural blade mode family as can be seen in the frequency versus nodal diameter plot in Fig. 2.2. The surrogate measurement data used in this section is comprised of the vibration response measured at each system resonance for a given frequency sweep. The surrogate measurement data is generated numerically using single-point harmonic excitation applied at blade 1.

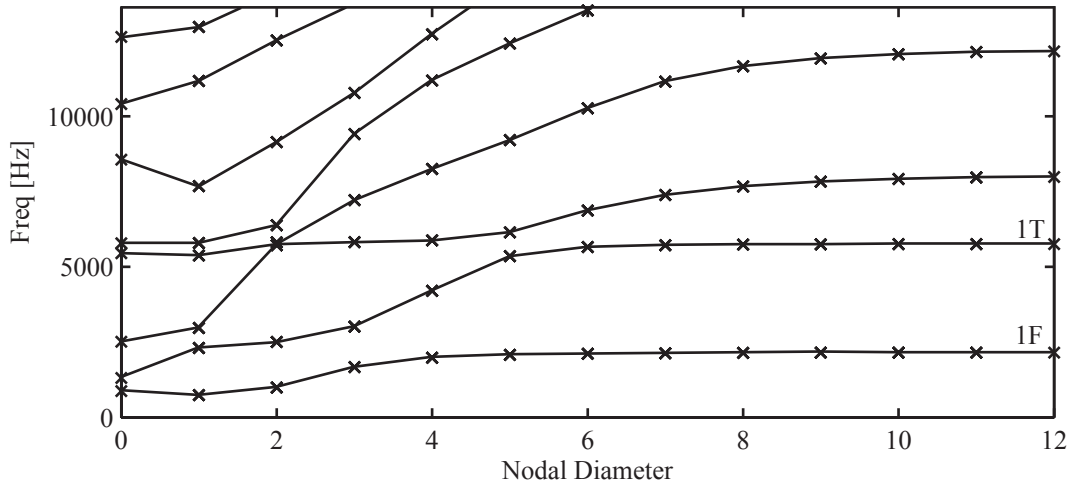

Figure 2.2: Natural frequencies versus nodal diameters for the blisk.

2.3.1 Selection Ratio

In Section 2.2, the SR factor was presented to evaluate the tuned system normal modes that are candidates for the IROM used for mistuning identification. Using a sector of the FEM, the tuned system normal modes are computed in cyclic coordinates. Using only these modes, the SR values are computed for each mode. The modes are then ranked according to their SR values, with the highest SR value corresponding to most favorable mode. Thus, IROMs of increasing size can be constructed using this mode ordering. That is, at each iteration, the tuned system normal mode with the highest available SR value is added to the IROM. Figure 2.3 shows the mode shapes in the frequency range from 0 to 5000 Hz, which are most closely related to the first flexural cantilevered blade mode. It can be seen in Figs. 2.3(a) and 2.3(b) that the higher nodal diameter modes tend to have higher participation factors and smaller blade-disk interface motion. This indicates that these modes have more blade-dominant motion, whereas modes at lower nodal diameters (in the veering region) have significant disk motion. The blade-dominant modes typically

have the largest SR values. These SR values are shown in Fig. 2.3(c) where the size of each circle denotes the SR value, and the numbers indicate the SR-based mode ordering. Figure 2.4 depicts the information in Fig. 2.3(c) in a way that more clearly shows the SR values. In particular, the modes with low SR values, below the dotted line at SR value of 0.1, should not be used for constructing the IROM for mistuning identification.

The importance of the IROM construction with respect to yielding accurate mistuning identification results can be seen in Figs. 2.5 and 2.6. The measurement data used was from the frequency range 0-5000 Hz. The results from the mistuning identification formulation presented in this work (denoted by MistID) are compared with FEM values computed using ANSYS®. Figure 2.5 shows the blade stiffness mistuning, $\mathbf{\Lambda}^{\delta,cb}$ and cyclic modeling error, $\mathbf{\Lambda}^{\delta,s}$, in the case where all of the modes in the 0 to 5000 Hz frequency range are used in the IROM. Figure 2.5(a) shows that the general pattern of mistuning is not captured. Similarly, the cyclic modeling error values shown in Fig. 2.5(b) exhibit extremely large errors compared to their exact value of 0.01.

Figure 2.6 shows the mistuning identification results using a model that contains only the 15 modes that have SR values above the threshold value of 0.1 (see Fig. 2.4). It is clear that the results for both blade stiffness mistuning shown in Fig. 2.6(a) and cyclic modeling error shown in Fig. 2.6(b) have improved significantly from those shown in Fig. 2.5. These results indicate that the automatic mode selection based on SR values performed well in this case.

It should also be noted that the SR values provide useful information about the tuned system modes in general. Under the assumption that the blade motion in the system modes of interest can be represented using a cantilevered blade mode or combination of a few modes, one can determine to which family of blade modes the system mode belongs. In Fig. 2.3(a), the cantilevered blade mode used to compute the participation factors was the

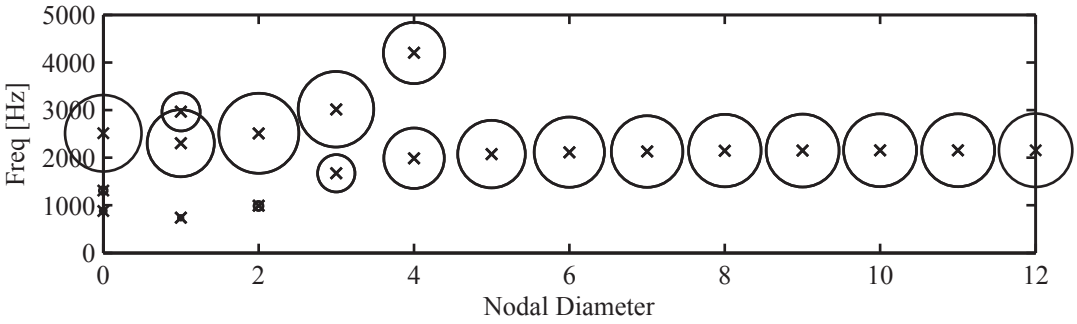

(a) Participation factors.

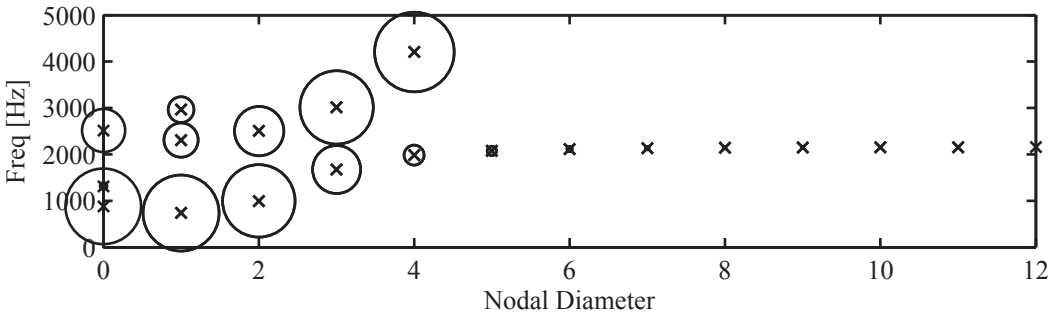

(b) Interface motion factors.

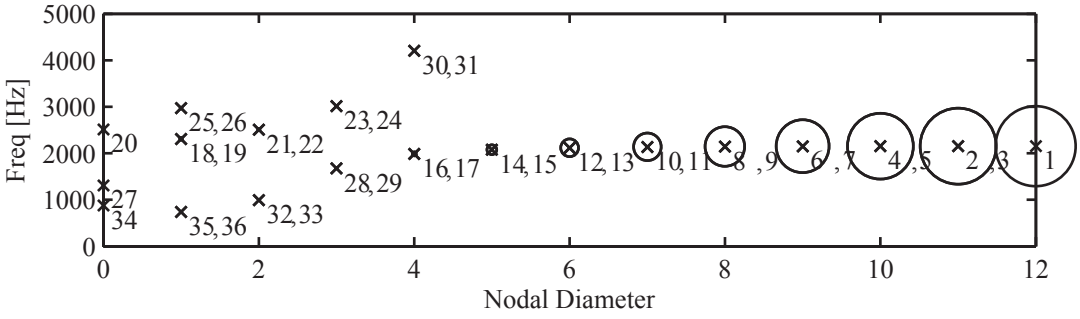

(c) Selection ratio (SR) factors. Numbers denote the mode selection order.

Figure 2.3: Parameters for IROM selection. The diameter of each circle indicates the magnitude of the parameter.

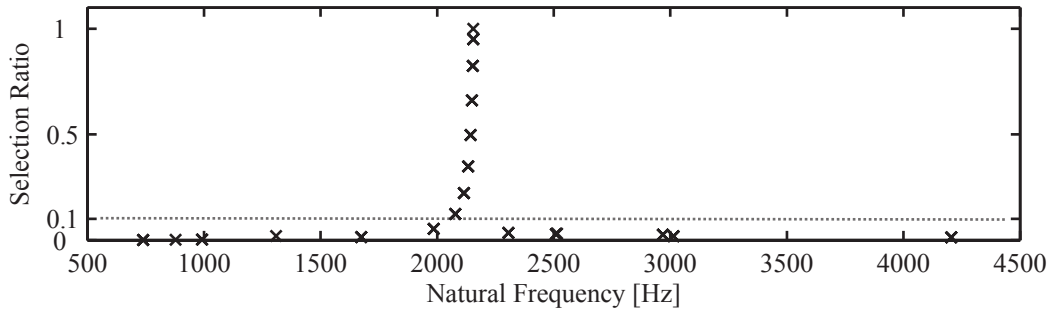

Figure 2.4: SR values versus natural frequency.

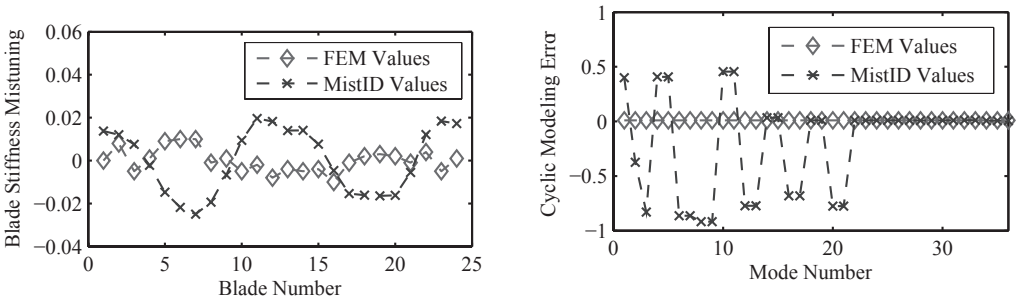

(a) Blade Stiffness Mistuning. (b) Cyclic Modeling Error.

Figure 2.5: Parameters for model updating using 36-DOF IROM (all modes in 0-5000 Hz).

first flexural blade mode. Therefore, the modes that belong to the first flexural blade mode family are shown by larger circles in Fig. 2.3(c). The interface motion in Fig. 2.3(b) helps to adjust the selection ratio to show modes that most closely fit in that blade mode family.

2.3.2 Restriction on Nodal Diameter Representation based on a Limited Measurement Points

One key consideration while choosing the IROM for mistuning identification is the rank of the modal matrix containing the tuned system normal modes. This matrix can be rank deficient because only DOF physically measured on the structure are used to represent

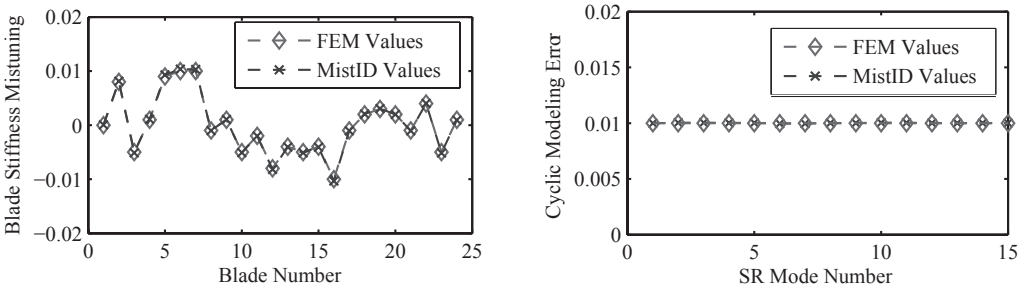

(a) Blade Stiffness Mistuning. (b) Cyclic Modeling Error.

Figure 2.6: Parameters for model updating using 15-DOF IROM (modes in 0-5000 Hz with SR value above 0.1).

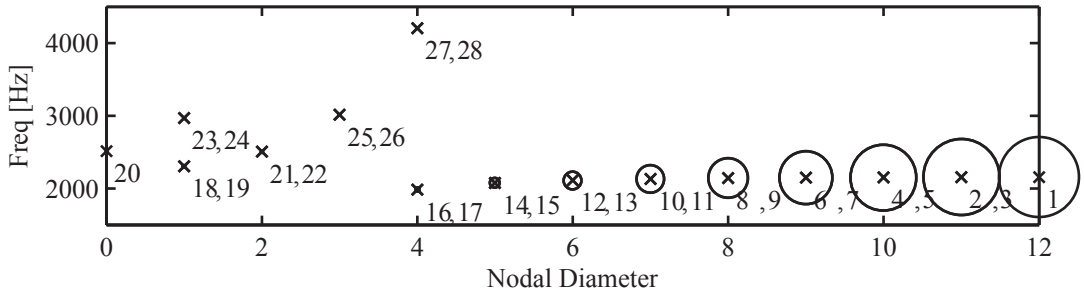

Figure 2.7: Mode ordering based strictly on SR values.

the mode shapes. For example, the matrix can become rank deficient when trying to distinguish between modes having the same nodal diameter when too few measurement points are used.

Figure 2.7 depicts the selection order of the mode shapes represented using only one measurement point per blade contained in the 1900-5000 Hz frequency range. The ordering of these modes is based strictly upon the SR values. It should be noted that the 23^{rd} and 24^{th} modes are the second mode pair added for the first nodal diameter. However, it is not until the 25^{th} and 26^{th} modes that the third nodal diameter is represented.

The rank of the modal matrix, given one measurement DOF per blade, is tracked in

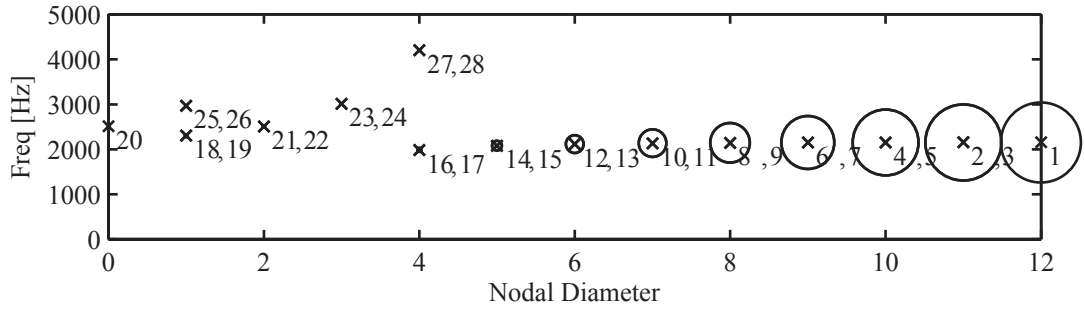

Figure 2.8: Mode ordering based on both SR values and nodal diameter content.

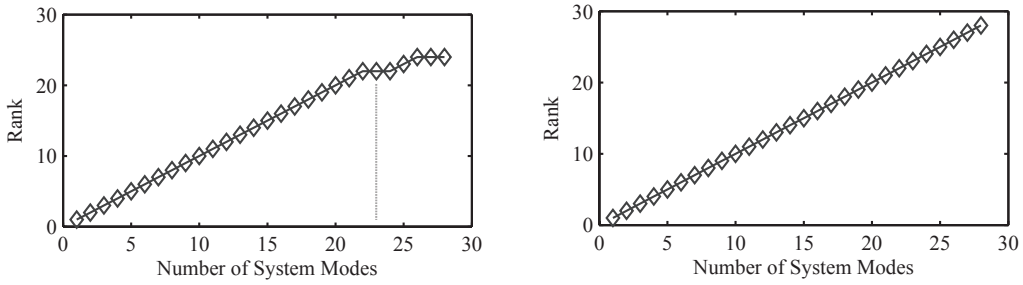

(a) One measurement DOF per blade. (b) Two measurement DOF per blade.

Figure 2.9: Rank of the modal matrix as the IROM is built up by adding modes based strictly on the SR values.

Fig. 2.9(a) as it is built up using the mode shapes ordered as shown in Fig. 2.7. Upon addition of the 23^{rd} mode to the IROM, the modal matrix becomes rank deficient. However, in Fig. 2.9(b), where two measurement DOF per blade are used, the modal matrix does not become rank deficient. In contrast to Fig. 2.7, the plot in Fig. 2.8 shows the ordering of the tuned system normal modes based upon the SR values with the exception of modes that would cause duplicity of the mode or mode pair for a given nodal diameter. Any mode or mode pair that would be the second for a given nodal diameter is not added until each nodal diameter has been represented by a mode or mode pair. As opposed to the ordering in Fig. 2.7, the ordering in Fig. 2.8 for the 23^{rd} and 24^{th} modes has changed to be at nodal

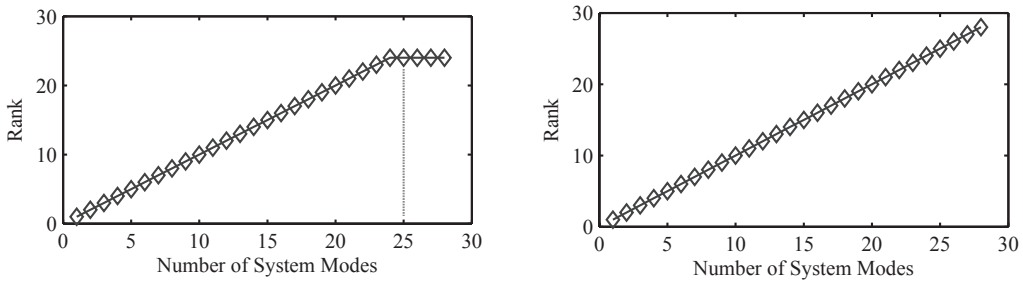

(a) One measurement DOF per blade. (b) Two measurement DOF per blade.

Figure 2.10: Rank of the modal matrix as the IROM is built up by adding modes based on both the SR values and nodal diameter content.

diameter 3, which was previously only represented with the 25^{th} and 26^{th} modes.

The benefit of this selection procedure is that with one measurement point per blade (24 total measurement points), modes with differing nodal diameter content are far more distinguishable, and therefore will not result in a rank deficient matrix. This is shown in Fig. 2.10(a) where it is clear that the rank deficiency occurs at mode 25 which is the first mode added that duplicates a nodal diameter. Using the algorithm that ensures that all nodal diameter content is represented before duplicating nodal diameter modal content is recommended because of the limited number of DOF used to represent the mode shape. It can be seen in Fig. 2.10(b) that using a second measurement DOF per blade generates a modal matrix with full rank. In general, the restriction of nodal diameter content of modes can be eliminated by measuring more DOFs per blade than the number of modes or mode pairs of a given nodal diameter that will be used in the IROM.

2.4 Evaluation of the Inverse ROM by Prescribing Surrogate Data

The results in Section 2.3 and show that IROM selection can be improved using the ideas presented in Sections 2.2.2-2.2.3. However, an arbitrary lower threshold value of 0.1 for the SR values was used to determine the size of the IROM. This requires experience

to generate an input to the procedure. Following the analysis presented in Section 2.2.4, a more systematic and automatic method for selecting the IROM size is further examined.

Figure 2.11 shows a flowchart of the procedure that makes use of the analysis of Section 2.2.4. The first step involves generating (i.e. prescribing) a mistuning pattern. It would generally be advisable to select a random mistuning pattern that has roughly the same level of mistuning that is expected in order to most effectively evaluate the IROMs used for mistuning identification. At this point, it is important to distinguish between a ROM used to solve the direct problem (direct ROM or DROM) and a ROM used to solve the inverse problem (inverse ROM or IROM). The accuracy of the DROM with respect to the parent FEM increases monotonically as modes are added. Therefore, a DROM constructed from all the available modes in a given frequency range can be used in place of the FEM for solving the direct problem and generating the test data for a prescribed mistuning pattern. In contrast, the accuracy of the IROM does not increase monotonically as modes are added due to the nature of the least squares approximations used in Eq. 2.16 and in the solution of the inverse identification problem.

The generated/prescribed mistuning pattern is then plugged into the DROM where all of the modes for a given frequency range are employed. The governing equation for the DROM can viewed as an eigenvalue problem where the eigenvalue is ω and the eigenvector is $\mathbf{p}$. Solving for the eigenvalue and eigenvector yields preliminary surrogate data. Before this data can be used as surrogate measurement data, the eigenvector is perturbed. This avoids the trivial solution when the inverse problem is solved. If the data generated is unperturbed, all possible IROMs will yield nearly the same results and the identified mistuning will match with the generated mistuning with negligible error. Once the noise is added, the surrogate test data set is formed of perturbed eigenvectors and unperturbed eigenvalues of the DROM. This surrogate data is then plugged into the IROM, where the

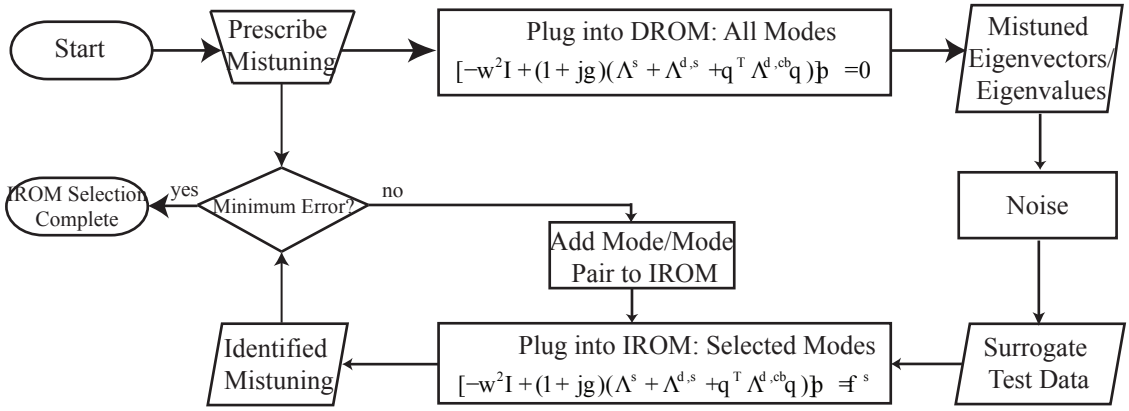

Figure 2.11: Flow diagram for IROM evaluation using surrogate data.

mistuning parameters are unknown. The IROM is made of a subset of the modes used in the DROM. Using the IROM with the surrogate data, a mistuning pattern can be computed. This mistuning pattern can be compared to the generated/prescribed mistuning pattern using the error presented in Section 2.2.4. After the error is evaluated, additional modes are added to the IROM and another mistuning pattern is generated. The new resulting error can be computed. If the error reaches a minimum or a satisfactory level, the IROM selection is complete. This IROM can then be trusted to identify mistuning from real measured data. In this manner, the performance of various IROMs can be evaluated quantitatively while working only within the reduced-order modeling framework, and the IROM construction procedure can be fully automated.

In this section, the frequency range for possible mode shapes is 0-5000 Hz. The frequency range for measurement data is 1900-2160 Hz. Figure 2.12 shows absolute error results obtained by comparison of the known mistuning from FEM and the mistuning values generated using the mistuning identification procedure. First, the benefit of using the SR-based mode ordering is clear, as both stiffness mistuning and cyclic modeling error

have smaller absolute error when the SR values are used. The detailed view of the stiffness mistuning in Fig. 2.12(a) shows that the error is suitably low in the range of 15–24 modes. However, the goal is to be able to predict what IROM will produce low absolute error without knowing the solution from a FEM.

For the direct problem, the level of perturbation to the eigenvectors $\mathbf{p}$ to produce the surrogate data was $\pm 1\%$ of $\mathbf{p}$. Figure 2.13 shows absolute error results obtained by comparison of the known mistuning from obtained by solving the direct problem with a larger DROM and a prescribed mistuning pattern as detailed in this section and the mistuning values generated using the mistuning identification procedure. From the plots in Fig. 2.13, it is evident that the general trends of absolute error can be predicted using a larger DROM for reference. According to Fig. 2.13(a), relatively low absolute error occurs for SR-ordered IROMs of size 13 through 19. Figure 2.14 shows the absolute errors for the direct problem, but with additional information about the blades. The sensitivity to modeling errors in the inverse problem is not uniform across all blades. So, it is possible for the error to be affected by the mistuning pattern. However, we observed that in general the error does not change significantly. This predicts that the selected IROM is a good choice for the mistuning identification procedure with respect to stiffness mistuning. Similar to the plot in Fig. 2.12(b), Fig. 2.13(b) shows steadily increasing values of absolute error. Therefore, these results indicate that the error trends could be used to determine an IROM size that yields robust and accurate mistuning identification results.

2.5 Conclusions

Techniques to more effectively identify mistuning parameters of blisks using the CMM approach to mistuning were presented. A quantitative metric, the SR value, was introduced to systematically evaluate the tuned system modes used for forming the IROM in the CMM

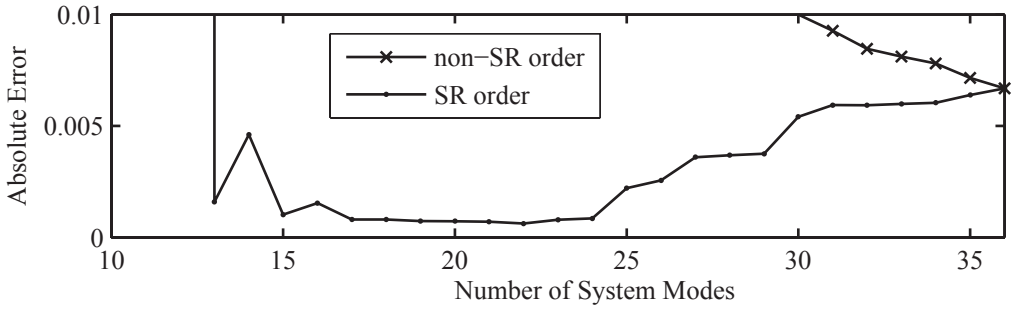

(a) Absolute Error of Blade Stiffness Mistuning.

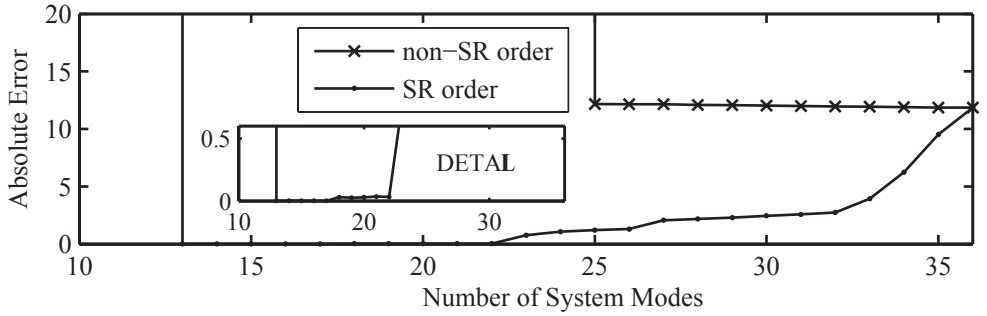

(b) Absolute Error of Cyclic Modeling Error.

Figure 2.12: Absolute error of model updating parameters by comparison with known FEM values with identified values obtained by adding candidate modes in the 0-5000 Hz range.

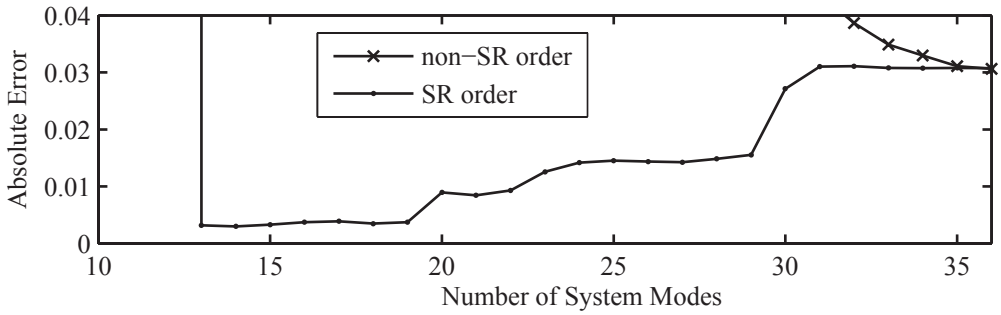

(a) Absolute Error of Blade Stiffness Mistuning.

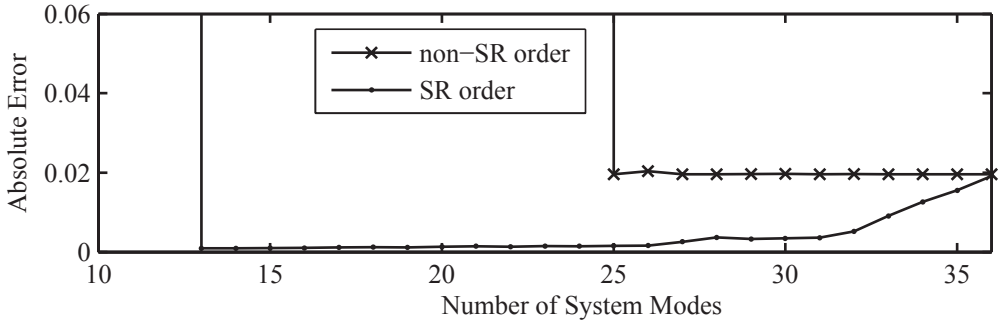

(b) Absolute Error of Cyclic Modeling Error.

Figure 2.13: Absolute error of model updating parameters by comparison with known values obtained using a DROM with identified values obtained by adding candidate modes in the 0-5000 Hz range.

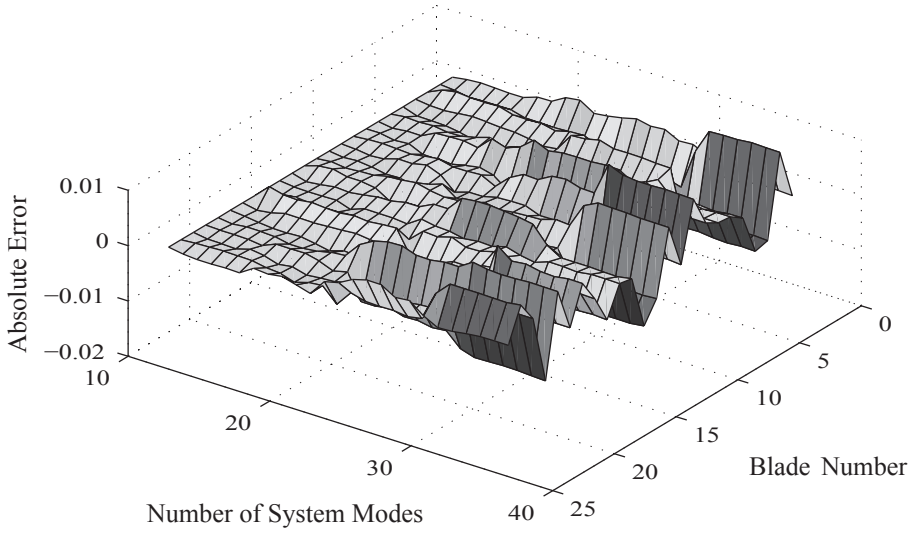

Figure 2.14: Absolute Error of Blade Stiffness Mistuning Across 24 Blades.

approach to mistuning identification. The SR values take into account the two assumptions made in the CMM technique, namely that the cantilevered blade normal mode shapes are similar to the blade portion tuned system normal mode shapes and that the blade-disk interface motion is small compared to the cantilevered blade motion. The SR values are generated using only information from the tuned system normal modes generated from the tuned FEM. Using these SR values, an effective IROM can be formed using tuned system normal modes. Using IROMs without ordering modes according to SR values can result in inaccurate mistuning identification. For these same cases, ordering modes according to the SR values leads to accurate mistuning parameters. Therefore, using this metric to select modes for the IROM can dramatically improve the accuracy of the mistuning identification results. It was also noted that these SR values could be used to categorize modes in a quantitative fashion according to blade mode families.

The effect of using a limited number of measurement points to represent the forced response and modes shapes was also considered. Because the current mistuning identifi-

cation formulation is intended for use with experimental data, tuned system mode shapes are represented with a reduced number of DOF. This places a limitation on the number and type of tuned system modes that can be used in the IROM for mistuning identification. If there are not enough measurement points, the reduced modal matrix is rank deficient. An important example of such rank deficiency occurs when representing modes having the same nodal diameter content, as demonstrated in this paper. To use multiple modes with the same nodal diameter content, it was shown to be necessary to use more measurement DOF per blade than the number of modes (in the ROM) which have the same nodal diameter.

In addition, a novel technique has been developed to determine automatically a suitable IROM size for solving the mistuning identification inverse problem. The approach is to prescribe a blade mistuning pattern and compute surrogate measurement data numerically using a larger ROM for the direct problem. This measurement data is produced by solving the forward problem and then perturbing the solution before plugging it into the inverse solver. The inverse formulation assumes that the mistuning is unknown and the IROM used is a subset of the ROM used for the direct problem. The solution to the inverse problem can then be compared directly to the prescribed mistuning pattern in order to check the performance of the IROM as modes are added. The results presented show that this process enables the automated construction of an IROM, and thus improve the overall accuracy and robustness of the mistuning identification. Furthermore, the automation of the procedure guarantees a systematic identification that does not demand the expertise that other current procedures require.

CHAPTER III

Mistuning Identification of Blisks at Higher Frequencies

3.1 Introduction

Structures that consist of a cyclic assembly of identical substructures are said to possess cyclic symmetry. The design of a single stage of a turbomachinery rotor, or bladed disk, typically features cyclic symmetry. Using cyclic symmetry routines in commercial finite element software enables one to analyze the entire bladed disk using a model of only one sector, which results in considerable reduction of computational costs. However, there are always small structural deviations among blades, called mistuning. Although mistuning is typically small (e.g., blade-alone natural frequency variations of up to about 5%), it can lead to a dramatic increase in the maximum blade stress, and is a major driver for high cycle fatigue in turbine engines. From a modeling perspective, mistuning destroys the cyclic symmetry, such that the full bladed disk needs to be modeled. Therefore, several efficient approaches for reduced-order modeling of mistuned bladed disks have been developed [14, 16–18, 21–23, 47]. Two groups of approaches are component based reduced order modes, [14, 16, 17] and models where the system is projected onto a subset of tuned system modes [18, 21]. Other approaches offer more flexibility in modeling and provide the possibility of modeling non-proportional mistuning [22,23,47]. Specifically, a method by Lim et al. [22,23] suggested a component based technique where the components con-

sist of the tuned and mistuned portions of the system which are projected onto the modes of the tuned system. More recently, a reduced order model (ROM) based on choosing tuned modes which have been perturbed based on proper orthogonal decomposition features was presented [47].

Many of these ROMs treat mistuning as a variation in natural frequencies for one or more modes of an isolated blade. That is useful because for bladed disks with inserted blades, one can measure the natural frequencies of manufactured blades directly. However, this is not possible with integrally bladed disks (blisks), which are becoming more prevalent in newer and next-generation engines. For blisks, several mistuning identification methods have been developed that use experimental response data for the full blisk in order to extract individual blade mistuning parameters. These methods range from techniques based on lumped parameter models [25, 26] to more advanced approaches requiring information from a finite element model [27–40]. Lim et al. [36] and Sinha et al. [40] present identification techniques that are flexible enough to identify the properties of blisks that are not restricted to proportional mistuning. The difference between these techniques is that the former identifies blade mistuning whereas the latter directly identifies the parameters of the mistuned system.

The combination of work on modeling and identification of mistuning in blisks has made it possible to accurately model blisks at a fraction of the computational cost compared to finite element analysis. However, in general, the current techniques have only been validated for predictions in lower frequency ranges. Most reduced-order modeling methods to date have not addressed the issues specific to mistuning in higher frequency ranges. In fact, some methods are specifically formulated for isolated, lower-frequency families of blade-dominated modes [34]. One exception is the component mode mistuning (CMM) method developed by Lim et al. [22,23], which allows different mistuning pat-

terns for different blade-alone modes. The method was validated numerically for a higher frequency range with two overlapping families of blade-dominated modes [23]. However, the CMM-based mistuning identification method [36–38] has only been validated in lower frequency ranges.

This work is an extension of previous results of the authors [57] on improving robustness of the CMM-based mistuning identification technique. The previous results considered only lower frequency regimes. The focus of this work is to extend CMM-based mistuning identification to higher frequency ranges. There are several additional challenges that arise as a result of higher frequency ranges. For example, the topology of the blade motion can become complicated, unlike the more uniform blade motion seen at lower frequencies. Considering the need to gather experimental data for mistuning identification techniques, extra emphasis must be placed on optimally choosing the locations on the blade where measurements should be taken. Also, as the blade motion is less uniform, capturing mistuning associated with physical parameter variations localized in a small portion of the blade can become sensitive to the modes used in the ROM and to the specific points where measurements are collected. Furthermore, isolated blade mode families of high modal density no longer exist. The existence of these regions is a key in obtaining simple ROMs to be used for the inverse problem in the low frequency ranges because these regions are quite sensitive to parameter variations in the system. The absence of these regions in the high frequency ranges increases the need to strategically select a ROM and measurement data that offers sensitivity to mistuning. This challenge is addressed in this paper by a novel approach.

The work is organized as follows. First, this work tackles the issue of selecting measurement points to use for mistuning identification which considers the vibration of smaller regions of the blade for higher modes. To this end, the effective independence distribution

vector (EIDV) [52, 53]method is used in an iterative approach to identify measurement points that yield the highest accuracy for mistuning identification given a limited amount of measurement data to be collected. Second, this work considers the identification of multiple mistuning patterns for the same blisk in different frequency ranges. Demonstrating that the mistuning identification method can identify such multiple mistuning patterns ensures that the appropriate mistuning parameters can be identified for the realistic case of non-uniform physical mistuning in each blade. Finally, a novel approach to identify physical parameter variations using the multiple mistuning patterns identified is presented.

3.2 Theory

3.2.1 Component Mode Mistuning Overview

The basic ROM used for the mistuning identification procedure is CMM [23]. The CMM model uses hybrid interface component mode synthesis (CMS). The formulation uses the nominal tuned system as a free interface component and a virtual substructure that represents the mistuned portion of the system which is a fixed interface component. The interface is defined as all degrees of freedom (DOF) which contain mistuning (specifically those DOF on the blades). Using the results of Yang and Griffin [56] which suggested that mistuned modes in a range of high modal density can be represented by tuned modes in the same region, it is possible to ignore the static modes of the synthesized equations. This results in the following simplified model that contains only system modes as a basis

$$-\omega^2\mathbf{p} + (1+j\gamma)\left[\mathbf{\Lambda}^s + \mathbf{\Lambda}^{\delta,s} + \mathbf{\Phi}^{s^{\mathrm{T}}}\mathbf{K}^\delta\mathbf{\Phi}^s\right]\mathbf{p} = \mathbf{f}^s. \tag{3.1}$$

The variable $\mathbf{p}$ is the modal amplitude coordinate, $\mathbf{\Lambda}^{\delta,cb}$ are the deviations of the cantilevered blade eigenvalues from the tuned and mistuned models, $\mathbf{q}$ are the participation factors of the cantilevered blade modes in the blade portion of the tuned system modes, and $\mathbf{f}^s$ is the modal forcing. The diagonal matrix $\mathbf{\Lambda}^{\delta,s}$ contains the differences in the eigen-

values of the assumed nominal tuned system and the actual tuned system as suggested in Lim et al. [36, 37], and is referred to as cyclic modeling error. Equation 3.1 has a dimension equal to the number of tuned system modes used as a basis for the ROM. This equation can be simplified by assuming that the blade portion of the tuned mode shapes can be represented as a linear combination of cantilevered blade mode shapes as follows

$$\begin{aligned} -\omega^2\mathbf{p} + (1+j\gamma)\left[\mathbf{\Lambda}^s + \mathbf{\Lambda}^{\delta,s} + \mathbf{q}^{\mathrm{T}}\mathbf{\Phi}^{cb^{\mathrm{T}}}\mathbf{K}^{\delta}\mathbf{\Phi}^{cb}\mathbf{q}\right]\mathbf{p} &= \mathbf{f}^s, \\ -\omega^2\mathbf{p} + (1+j\gamma)\left[\mathbf{\Lambda}^s + \mathbf{\Lambda}^{\delta,s} + \mathbf{q}^{\mathrm{T}}\mathbf{\Lambda}^{\delta,cb}\mathbf{q}\right]\mathbf{p} &= \mathbf{f}^s, \end{aligned} \tag{3.2}$$

where $\mathbf{q}$ represents the participation the cantilevered blade mode shape in the system blade mode shape, and $\mathbf{\Phi}^{cb}$ are the cantilevered blade modes shapes. The change in the cantilevered blade eigenvalues between the tuned and mistuned blisks is $\mathbf{\Lambda}^{\delta,cb}$.

The use of cantilevered blade mode shapes to represent the blade portion of system modes implies that mistuning appears in the equations as $\mathbf{\Lambda}^{\delta,cb}$. This also means that one tuned system normal mode (blade portion) can be represented as a linear combination of multiple cantilevered blade mode shapes. At lower frequencies, modes tend to be closely spaced in frequency, and the blade motion can be well represented by the cantilevered blade mode shape. As frequencies increase and veerings become more common, the motion of the blades can be a complicated combination of multiple cantilevered blade mode shapes. Therefore, to obtain accurate predictions, one should include as many cantilevered blade mode shapes as necessary to predict the blade portion of the system normal mode. The diagonal matrix $\mathbf{\Lambda}^{\delta,cb}$ contains the deviations of the cantilevered blade eigenvalues from their nominal. In the case where multiple cantilevered blade normal modes are needed to represent the blade portion of the system normal mode, the matrix has multiple entries for each blade. This corresponds to eigenvalue deviations for each blade for each cantilevered blade mode used. This formulation accounts for the cases where mistuning

is manifested differently for each cantilevered blade mode shape, and leads to an accurate reduced-order model.

3.2.2 Iterative Measurement Point Selection for Mistuning Identification

The previous work by the authors [57] introduced the concept of an inverse ROM (IROM). IROMs were distinguished from traditional ROMs, referred to as the direct ROMs (DROMs), because it was determined that some modes are insensitive to mistuning and they may lead to larger errors in approximately following the assumptions of the CMM-based ROM. Although accurate for direct problems (such as forced response predictions), these errors can prove detrimental for inverse problems. When coupled with the least-squares solutions performed in the mistuning identification procedure, the use of DROMs (and insensitive modes) can lead to large errors in the identified mistuning. Thus, making use of the IROM concept is essential to systematically generating robust ROMs that can accurately identify mistuning. In the past, this study was performed only in low frequency ranges encompassing only a few isolated blade mode families which had high modal density. Furthermore, the motion of the structure at those frequencies was relatively simple.

Extending the previous work [57] to higher frequency ranges is not trivial and represents one of the novel contributions of this paper. The CMM-based ROM transforms the governing equations from physical coordinates $\mathbf{x}$ to modal coordinates $\mathbf{p}$ in order to reduce the model size using the equation

$$\mathbf{x} = \mathbf{\Phi}^s \mathbf{p}, \tag{3.3}$$

where $\mathbf{\Phi}^s$ is the tuned modal matrix (mass normalized). To reduce the size of the model, $\mathbf{\Phi}^s$ is truncated to include only a select group of modes in the frequency range of interest. For mistuning identification, only a few physical points are measured experimentally. The tuned system normal modes can be found easily from the finite element model (FEM) of

the tuned system using cyclic symmetry. Using this information, the modal coordinates $\mathbf{p}$ can be found. However, there are two key reasons why determining the appropriate modal coordinates is challenging. First, only a significantly reduced subset of points can be measured because the physical coordinates $\mathbf{x}$ are determined experimentally. This means that points must be strategically chosen to best represent the physical motion and thereby the mode shapes. Second, Eq. 3.3 is a least squares problem which is solved for the modal coordinates (because the number of modes used for the ROM is smaller than the total number of DOF). The quality of the solution of the least squares problem depends on the quality of the measurement points taken in the physical domain.

In addition, the increase in complexity of the response of the structure in higher frequency ranges makes it more difficult to identify mistuning. For example,consider a case (often found in the higher frequency ranges) where the topology of the blade motion is highly complicated. This motion could have many nodal lines and antinodes. If measurement points are chosen such that they are on nodal lines, then it would be impossible to identify mistuning because values of $\mathbf{p}$ would be erroneously measured to be zero. This is an extreme case, but it demonstrates the difficulty of correctly selecting points that are sensitive to mistuning especially in higher frequency ranges where the blade motion is more complex. Similarly, it also becomes important to optimally choose the measurement points as to be able to distinguish between mode shapes when only a small number of points are used per blade in the higher frequency ranges. For example,consider another scenario where a measurement point is chosen at the leading edge tip of the blade. It is possible that several modes have similar displacements at that particular point on the blade, but are otherwise dissimilar. If only one measurement point is used per blade, then the physical-to-modal transformation is ill conditioned and results in a poor set of modal coordinates to be used in the IROM. To address this issue a novel approach is presented

herein, where measurement points are chosen for each IROM in a manner that ensures good conditioning (by ensuring the independence of the vectors used in Eq. 3.3), this issue is avoided. This technique is essential because in the higher frequency ranges there are a limited number of modes that are optimally sensitive to mistuning.

The modal density for blade-alone families decreases with increasing frequency, it is necessary to choose the most sensitive modes. Previously [57], it was possible to choose a frequency range from which the IROM was selected. Using all the modes in that range, appropriate measurement points were selected, and that was sufficient to identify mistuning with high levels of accuracy. However, as the modal density decreases, it becomes more important to have accurate measurement points for the IROM selected. This is due to the sensitivity of the response (which occurs in a small frequency range) to slight parameter variations. Any change to one mode in that small frequency range affects the response throughout the frequency range. Such a behavior indicates that those modes are very sensitive to mistuning. Typically, predictions made using DROMs (which include insensitive modes) only suffer from the fact that the DROM has slightly too many DOF. However, in the case of IROMs, the inclusion of insensitive modes leads to inaccurate mistuning identification results. Results have shown that in certain cases there are not enough sensitive modes to identify mistuning. Also, results have shown that the number of modes must be at least equal to half of the number of blades in order to have an acceptable model. Including as many mistuning-sensitive modes as possible in the model also addresses another potential scenario. For example, consider a case in which a blade has only variations in one of its regions. The modes that have a high response in that region and are sensitive to physical changes in that region should be included. In addition, choosing to use those modes requires an optimal selection of the measurement points as well. The measurement points should be optimally selected to exploit favorable sensitivity. In general, it is essen-

tial to select the modes with the highest sensitivity to mistuning. Because of that, the most effective measurement points need to be chosen to represent the mode shapes for each IROM size considered. The paper addresses these coupled challenges.

Since the selection of the measured points used to represent the response in the physical domain is important, an algorithm is developed to choose the most appropriate points. Generalizing our earlier work [57], the DROM concept is extended. The previous application of DROMs made use of numerically generated test data in modal coordinates, in essence creating sets of surrogate data $\mathbf{p}$. With this information, the system could be interrogated to determine the correct number of tuned system mode shapes $\mathbf{\Phi}^s$ to be used in the model. For the algorithm herein, the technique is modified to generate surrogate *physical* data $\mathbf{x}$ to account for the error created in the least squares transformation from physical to modal coordinates. This approach better describes how actual data affects the transformation. Also, in the previous work, the measurement points were chosen only once for all modes by using the effective independent distribution vector (EIDV) [52, 53]. That approach is employed here in a novel iterative fashion. The DROM interrogates the system and determines which set of tuned system modes provides the best basis for identifying mistuning. In the previous work, a candidate set of modes was used to determine the EIDV measurement points. However, for each subset of the candidate modes, the EIDV measurement points are not optimal. In this work, the EIDV algorithm is used for each set of possible IROM modes to determine measurement points which are best suited for the identification procedure. Using DROM generated data for all possible EIDV measurement point combinations, each IROM can be interrogated with the optimal set of EIDV measurement points. This novel approach provides the best set of measurement points for the best set of basis modes to be used in the mistuning identification procedure.

The algorithm for the iterative measurement point selection can be seen in Fig. 3.1.

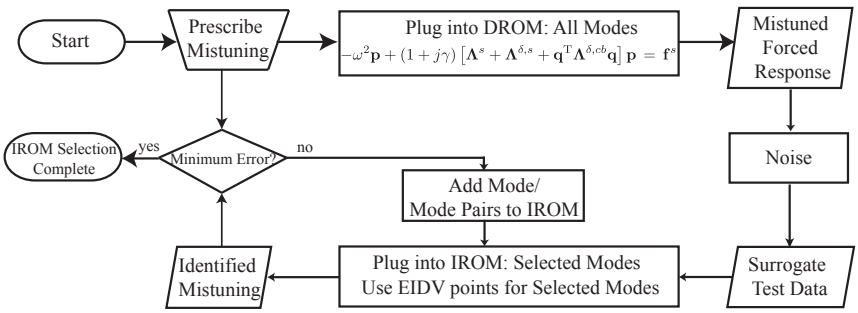

Figure 3.1: Flow diagram for IROM evaluation using surrogate data and EIDV measurement iteration.

First, randomly chosen mistuning values are prescribed for each blade in the blisk. These values, along with a given forcing are inserted into Eq. 3.2. The only unknown in that equation is the modal response $\mathbf{p}$, which is computed. Next, $\mathbf{p}$ is expanded using Eq. 3.3 to compute the physical mistuned forced response $\mathbf{x}$. Next, noise is added to simulate experimental noise. At this point it is necessary to know which modes are used in the IROM. With these IROM modes, the EIDV procedure is used to compute the optimal measurement points. The physical response is then converted back to modal response by inverting Eq. 3.3 where the matrix $\mathbf{\Phi}^s$ contains only the chosen measurement points for each set of IROM modes. This surrogate test data is then plugged into Eq. 3.2 which has been formed using the same number of IROM modes. At this point, the mistuning can be identified and compared with the known (chosen) values of the mistuning. This procedure is repeated for each IROM size until a minimum error in the identified mistuning is reached. The entire process is also repeated for additional mistuning patterns to ensure that the IROM chosen is statistically the best for any mistuning pattern that might be present in the actual system.

3.2.3 Multiple Mistuning Patterns

The CMM-based mistuning identification algorithm offers a unique benefit of being able to identify multiple mistuning patterns. A benefit of having multiple distinct patterns, or multiple sets of parameters for a given system, is using these sets of parameters in the modal space to determine information about parameter variations in the physical space. This section introduces a novel approach to identifying physical parameter variations in the blades of blisks. The theory is developed using the knowledge that parameter variations in the modal domain must be a function of parameter variations in the physical domain. Note that this paper discusses small mistuning. Hence, it is possible to avoid nonlinear analyses. Thus, we can identify physical parameter variations using a small system of linear equations. Also, the concept is flexible and can be applied to blisks with different mistuning patterns and physical parameter variations by using only a tuned sector model. This flexibility is obtained by first mapping the effects of the physical parameter variations into mistuning values for a number of mode families.

In the following, we consider the case where there are variations in blade properties characterized by n independent variables. These variables are denoted by α_n. The physical meaning of these variables depends on each particular application. In this work, we consider each blade to be conceptually divided into N regions of interest. A small change in structural properties at each location n on each blade is represented by α_n (one α_n for each blade). The quantity α_n can be any small change in a parameter of that region of the blade (such as a change in mass, stiffness or geometry). The mistuning of cantilevered blade mode family m for the entire blade caused by local mistuning at the n^{th} location in the blade is defined as

$$\Delta\lambda_n{}^m = f^m(\alpha_n) = f^m\,|_{\alpha_n=0} + \left.\frac{df^m}{d\alpha_n}\right|_{\alpha_n=0} \alpha_n + O(\alpha_n{}^2), \tag{3.4}$$

where f is a complicated, unknown function which is zero for a tuned system. Hence, assuming that mistuning is proportional to the change in the blade, and neglecting higher order terms, Eq. 3.4 becomes

$$\Delta\lambda_n{}^m = f^m(\alpha_n) = \left.\frac{\partial f^m}{\partial \alpha_n}\right|_{\alpha_n=0} \alpha_n. \tag{3.5}$$

Similarly, the mistuning for mode m for the entire blade with N mistuning locations can be written using the same assumptions as

$$\Delta\lambda^m = f^m(\boldsymbol{\alpha}) = \left.\frac{\partial f^m}{\partial \alpha_1}\right|_{\boldsymbol{\alpha}=\mathbf{0}} \alpha_1 + \cdots + \left.\frac{\partial f^m}{\partial \alpha_n}\right|_{\boldsymbol{\alpha}=\mathbf{0}} \alpha_N, \tag{3.6}$$

where $\boldsymbol{\alpha} = [\alpha_1, \ldots, \alpha_N]^T$. If one uses the mistuning identification procedure [38, 57], in general it is possible to determine multiple distinct mistuning patterns related to different blades. Then consider the case when N distinct mistuning values are determined for N modes

$$\begin{aligned} \Delta\lambda^1 &= \left.\frac{\partial f^1}{\partial \alpha_1}\right|_{\boldsymbol{\alpha}=\mathbf{0}} \alpha_1 + \cdots + \left.\frac{\partial f^1}{\partial \alpha_N}\right|_{\boldsymbol{\alpha}=\mathbf{0}} \alpha_N, \\ &\vdots \\ \Delta\lambda^N &= \left.\frac{\partial f^N}{\partial \alpha_1}\right|_{\boldsymbol{\alpha}=\mathbf{0}} \alpha_1 + \cdots + \left.\frac{\partial f^N}{\partial \alpha_N}\right|_{\boldsymbol{\alpha}=\mathbf{0}} \alpha_N, \end{aligned} \tag{3.7}$$

where the matrix $\mathbf{C}$ has entries $C_{mn} = \left.\frac{\partial f^m}{\partial \alpha_n}\right|_{\alpha_n=0}$.

At this point, a single blade may be mapped for a given type of physical parameter variation α_n. This is done by solving Eq. 3.5 for the individual coefficients $C_{mn} = \left.\frac{\partial f^m}{\partial \alpha_n}\right|_{\alpha_n=0}$. To solve for the individual coefficients, the blade is first sectioned into N parts. Note that we consider the case where each parameter α_n refers to one of the N distinct regions of the blade. Then, a physical parameter α_n is changed for section n only. Using a simple (blade-level) finite element modal analysis on both the original cantilevered blade and the modified cantilevered blade, the change in the cantilevered blade eigenvalue, or

mistuning ($\Delta\lambda$), can be computed for N cantilevered blade modes. Using the N mistuning patterns and the single parameter variation, N coefficients $C_{m,n}$ can be computed for $m = 1, 2, ..., N$ using Eq. 3.5. Finally, this is repeated for each of the remaining sections/parts of the blade to acquire the coefficients associated with those sections/parts of the blade.

Mistuning patterns are related to the deviations in the eigenvalues of a given cantilevered blade mode. It is possible that a particular blade mode has very little motion in a particular region of the blade or is otherwise insensitive to the area of the blade where the physical parameter variation (mistuning) is present. Therefore, this method of identifying physical parameter variations using variations in modal parameters may lead to ill-conditioned matrices. To avoid this ill-conditioning, a unique technique is suggested. First, a number of mistuning patterns greater than the number of physical locations to be identified is chosen. These patterns are slightly perturbed. Then, the physical parameter variations are computed. These are then immediately plugged back into the system to check if the original prescribed mistuning patterns are recovered accurately. If the patterns are not recovered accurately, then one can conclude that one of the mistuning patterns is insensitive to the physical parameter variations at the locations being considered. By iterating on this sequence of equations, one can ensure through a computationally inexpensive way that the identification will provide accurate results. This has proven to be more reliable than placing a criterion on the value of the condition number of the matrix C.

3.3 Results

The results presented are related to the tuned finite element model shown in Fig. 3.2(a). The model has two moduli of elasticity shown by different colors. At this point, even though there are multiple material parameters in the model, it is still cyclically symmetric,

and therefore tuned. In Fig. 3.2(b), the frequency versus nodal diameter map is shown up to 20 kHz, which is the effective range for the first six cantilevered blade mode families. It is noted that at the higher frequency ranges, significant veering regions are present. These regions make mistuning identification more difficult because of an assumption in the basic CMM formulation that mistuned modes closely spaced in frequency can be represented by tuned modes in that same frequency range, a concept introduced by Yang and Griffin [56]. As veering regions become more dominant, this assumption is violated even in regions of high modal density. Therefore, this system is suitable to test the novel methods proposed herein.

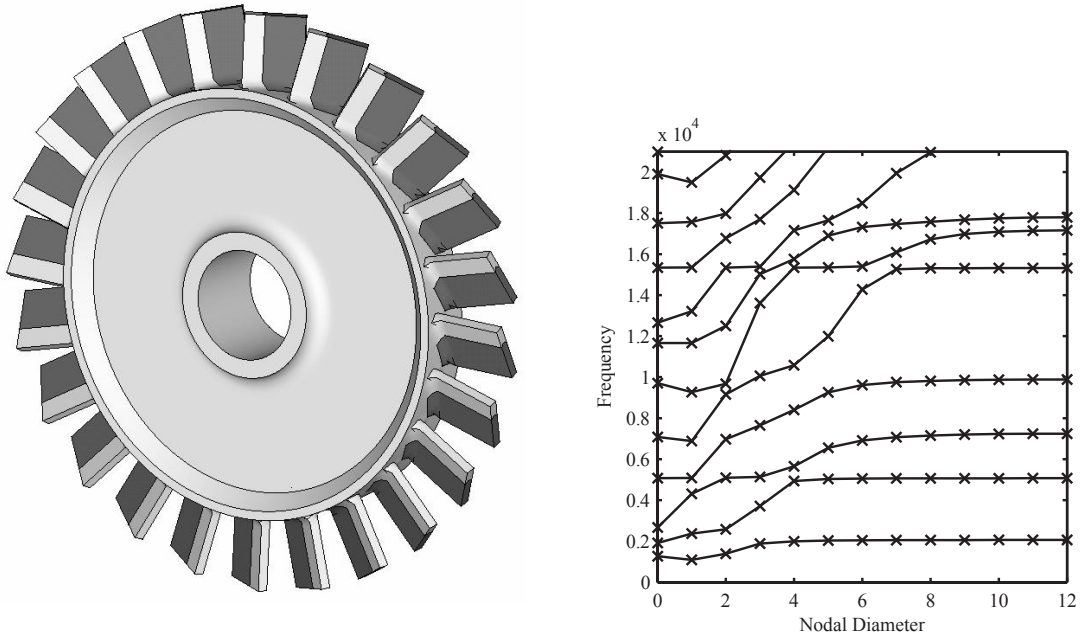

(a) FEM of the blisk with 24 blades. (b) Frequency vs. Nodal Diameter.

Figure 3.2: Overview of the tuned FEM of a blisk with 24 blades.

3.3.1 Iterative Measurement Point Selection for Mistuning Identification

The algorithm for the proposed iterative method is shown in Fig. 3.1. This approach features two improvements compared to the previous work of the authors [57]. First, for the forward problem, the forced response analysis is used to generate surrogate data for the identification procedure. This takes into account the error that comes from the transformation from physical to modal coordinates. The second improvement compared to the previous work is the iteration on the EIDV measurement points which is an essential part of identifying mistuning in higher frequency ranges.

Considering Fig. 3.3, the necessity of being selective for the limited amount of measurement points becomes obvious. Although these are not the system modes that EIDV uses to determine the measurement points, it is important to remember that CMM uses the cantilevered blade mode to approximate the blade portion of the system modes. In Fig. 3.4(a), the mistuning results are presented for family six using a valid but suboptimal EIDV measurement point (per blade) for the given frequency range, and then the optimal point for the IROM selected modes. It is clear that results with lower accuracy are obtained if a suboptimal point is used. Figure 3.4(b) shows the mistuning error over all possible IROM sizes. The DROM forced response surrogate data used with the mistuning algorithm determines that the optimal set of modes happens to be all of the modes in the regions. It should be noted that it is coincidental that all of the modes are used.

(a) 1st cantilevered blade mode (2106 Hz).

(b) 6th cantilevered blade mode (17861 Hz).

Figure 3.3: Comparison of the response of blade portions for different CB modes.

The ANSYS® generated forced response results for suboptimal EIDV measurement points indicate that a different mode set would be used and the minimum error would be only slightly less than the error for the optimal point (at that number of modes). However, it is clear that, with the optimal EIDV measurement point in conjunction with the optimal number of modes, the error is minimized with the given set of measurement points. It should also be noted that the DROM surrogate data is obtained using several random mistuning patterns to compute the forced response. Then, the algorithm selects the worse error out of those patterns for a given number of IROM modes. This explains why the DROM curve has more error than the optimal curve.

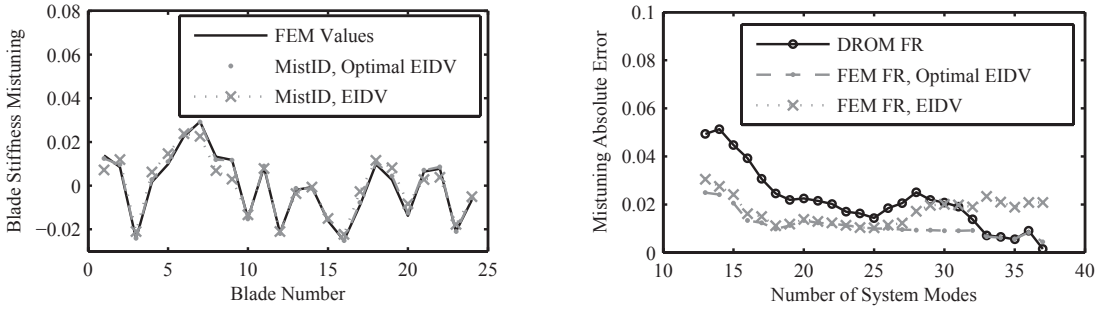

(a) Model updating parameters for 6th CB mode

(b) Mistuning error vs. mode number for 6th CB mode

Figure 3.4: Justification of iterative EIDV procedure using 6th cantilevered blade mode.

3.3.2 Multiple Mistuning Patterns

To demonstrate the approach, multiple mistuning patterns are investigated for the 24-bladed disk in Fig. 3.2(a), which is modified such that the blade portion is divided into four segments with differing modulus of elasticity. The subsequent mistuned model generated from the tuned 24-blade disk is shown in Fig 3.5. Note that each section of the blade has a distinct random change in modulus of elasticity of under 5%. These physical changes result in a different mistuning pattern for the six different cantilevered blade modes used

in the model. This is demonstrated by comparing results for the first cantilevered blade mode family and the fifth in Fig. 3.6.

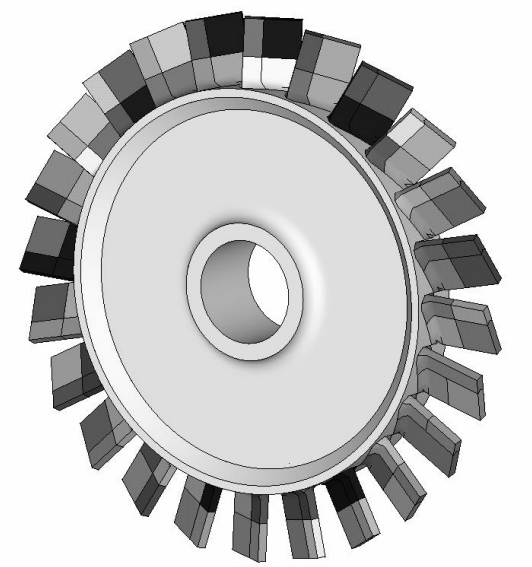

Figure 3.5: FEM of blisk with multiple mistuning patterns.

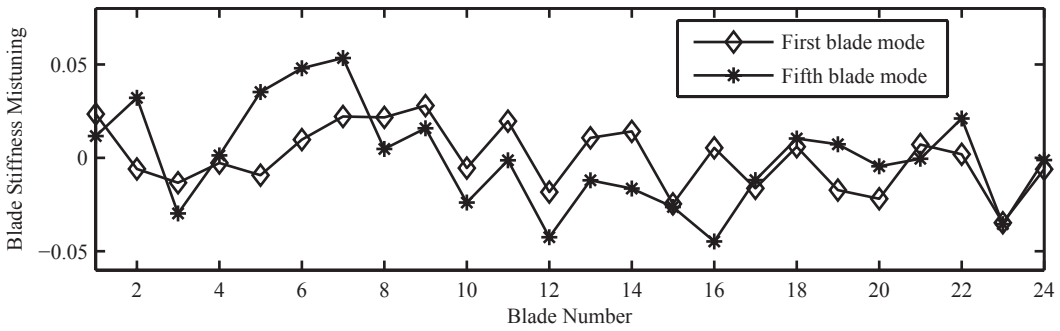

Figure 3.6: Model updating parameters for 1st and 5th cantilevered blade modes.

To demonstrate the current capabilities of the mistuning identification algorithm, Figs. 3.7(a)-3.7(f) show that these different mistuning patterns can indeed be identified. It should be noted that the current mistuning identification procedure makes use of a combination of the author's previous work [57], and the measurement point iteration algorithm

which is presented in the following section. It is clear from Figs. 3.7(a)-3.7(f) that the mistuning can be well identified for each cantilevered blade mode family. Since the last cantilevered blade mode family has a contributions up to 20kHz, the results are sufficient to suggest that mistuning can be identified in higher frequency ranges without significant loss of accuracy. As it is well known that forced response amplitudes of mistuned systems are highly sensitive to mistuning, the ability to identify mistuning and subsequently model mistuning is critical to get accurate predictions. Furthermore, these results demonstrate that six distinct mistuning patterns can be identified, which allows for the modeling of non-proportional mistuning.

Because distinct mistuning patterns exist in this case, it is possible that one may be able to extract information about the location and amount of mistuning from a physical perspective. Consider Fig. 3.3(a) and 3.3(b) which show the first and six cantilevered blade modes. It is evident that changing the frequencies of each of these cantilevered blade modes will have different effects on the same physical location of the blade. This general idea was employed to back out variations in the modulus of elasticity of four locations on a blade using the mistuning identification. As mentioned in Sec. 3.23.2.3, it is theoretically possible to identify these four locations with the first four mistuning patterns. However, in practice, this results in the inversion of an ill-conditioned matrix $\mathbf{C}$, which heavily places reliance on the accuracy of the mistuning results. Physically, ill conditioning is caused by the fact that the first four cantilevered blade mode families are not distinguishable enough to accurately determine these parameters. As more cantilevered blade mode families are added, additional sensitivity to specific locations of a blade is added. Therefore, to improve the conditioning of matrix $\mathbf{C}$, additional mistuning patterns were identified.

It was determined that only four mistuning patterns are needed to obtain accurate predictions of the physical mistuning. The patterns that were used came from the 1st, 3rd, 5th,

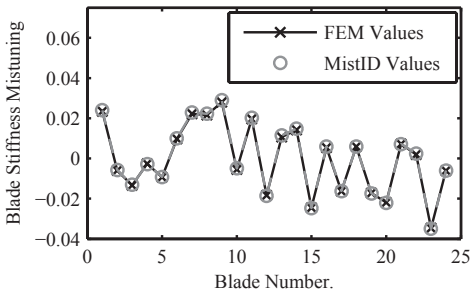

(a) Blade stiffness mistuning for 1st CB mode.

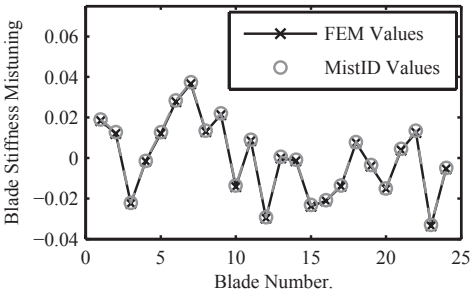

(b) Blade stiffness mistuning for 2nd CB mode.

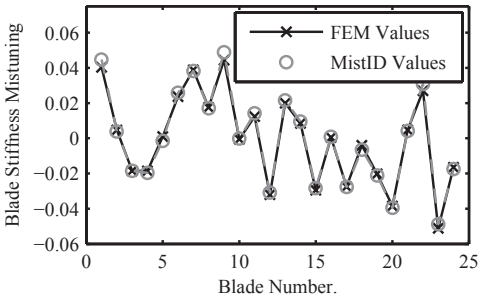

(c) Blade stiffness mistuning for 3rd CB mode.

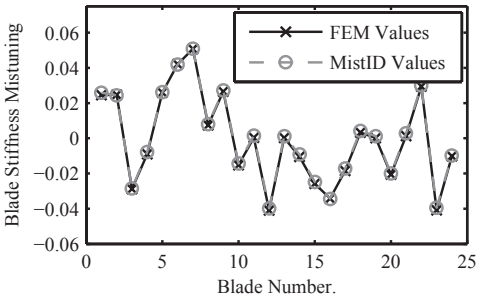

(d) Blade stiffness mistuning for 4th CB mode.

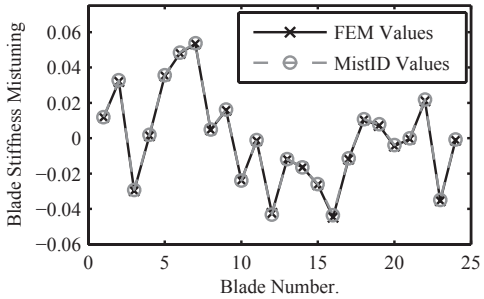

(e) Blade stiffness mistuning for 5th CB mode.

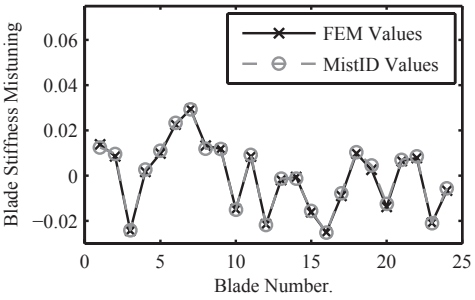

(f) Blade stiffness mistuning for 6th CB mode.

Figure 3.7: Model updating parameters for 1st through 6th cantilevered blade modes (0-18000 Hz). MistID values represent mistuning values obtained using the proposed mistuning identification approach.

and 6th cantilevered blade mode families. The results are shown in Fig. 3.8. Modulus of elasticity variations were identified for four different locations for each blade. Although the theoretical limit to the number of locations to identify is the number of elements, clearly there are practical limits to the resolution that can be obtained.

In general, a particular set of mistuning patterns is best for identifying the modulus of elasticity variations in the blade. Next, a novel way is proposed to practically determine which mistuning families are needed to obtain accurate predictions. The variations in modulus of elasticity are computed by inverting the coefficient matrix $\mathbf{C}$ as described in Sec. 3.23.2.3, and multiplying it by mistuning values from various cantilevered blade mode families for a given physical blade. It is rather inexpensive to get the coefficient matrix $\mathbf{C}$ and surrogate mistuning patterns by applying a mistuning pattern to a cantilevered blade and computing the modal frequency. This can done before collecting expensive measurement data. With a greater number surrogate mistuning patterns than the physical locations to be identified and with the corresponding coefficient matrix $\mathbf{C}$, it is possible to compute variations in the modulus of elasticity. By slightly perturbing the mistuning patterns for less than the maximum expected patterns, identifying variations in the modulus of elasticity, and then recomputing the mistuning patterns, one can compute a residual. If the residual is low for all mistuning families, it is likely that the computed variation in modulus of elasticity is correct. However, if the residual is high for any one of the mistuning families, then more or different mistuning patterns are needed to determine the change in modulus of elasticity. The concept is demonstrated in Fig. 3.9. The plot shows that using only mistuning families one through four yields the line with circles. These results demonstrate that family six is not accurately represented and that more or different families must be used. The line with diamonds shows that an improved identification of variations in the modulus of elasticity are obtained by using mistuning families one, two,

five, and six. Note that all mistuning families had low residuals in this case, including families two and four.

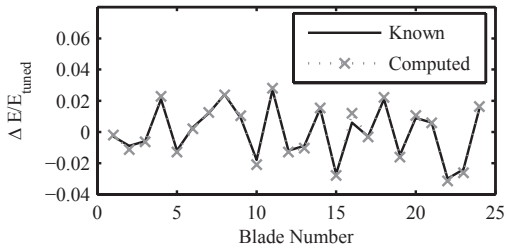

(a) Variation at the leading edge root.

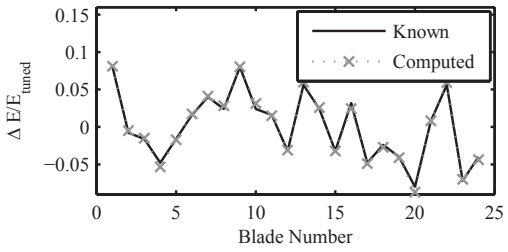

(b) Variation at the trailing edge root.

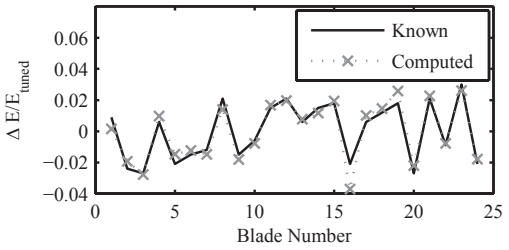

(c) Variation at the leading edge tip.

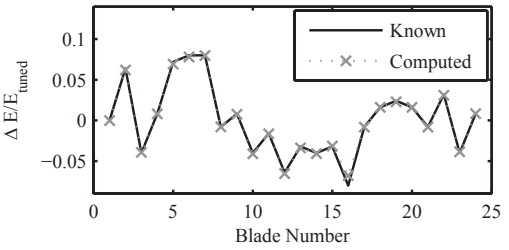

(d) Variation at the trailing edge tip.

Figure 3.8: Identification of modulus of elasticity variations at specified blade locations using MistID results.

3.4 Discussion and Conclusions

In higher frequency ranges, one is more likely to observe system modes that feature a combination of blade and disk motion. Moreover, it is more likely that the blade portion of system normal modes will respond like a combination of blade-alone mode shapes rather than one single mode shape. Another difficulty with higher frequencies is the localization of motion in certain portions of the blade. At lower frequencies, the response is relatively uniform throughout the blade. Also, it is generally assumed that mistuning is constant for the entire blade. However, the physical sources of mistuning (e.g., variation in blade thickness from the nominal design) are generally not uniform throughout the blade,

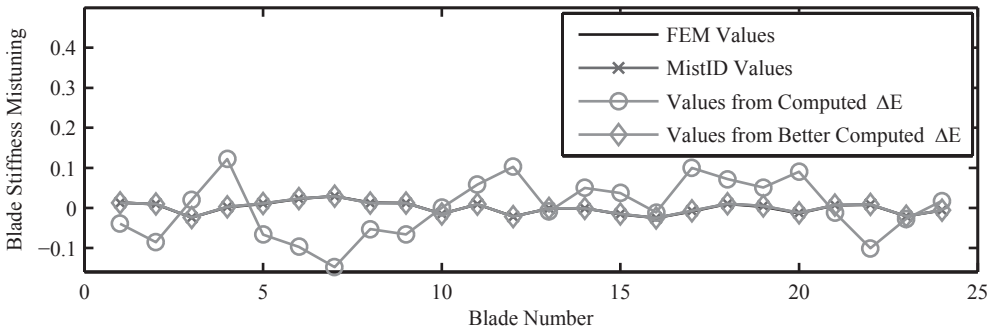

Figure 3.9: Improvement of modulus of elasticity variation using residual calculations for 6th CB mode.

and therefore the mistuning pattern changes for different blade-alone mode shapes if they feature different motions in different regions of the blade. This is important for higher frequency modes as blades exhibit motion localized to smaller regions.

To address this issue, mistuning identification and reduced-order model updating in higher frequency ranges has been discussed. The identification of multiple mistuning patterns and how these affect modeling results at higher modes was considered. The specific geometric location of blade imperfections that cause mistuning becomes more important at higher frequencies, because the wavelength decreases and the blade response features higher amplitudes in smaller regions of each blade. Thus, it becomes necessary to determine how each mode is affected by mistuning by identifying a (unique) set of mistuning values for each blade mode type. Using the CMM-based mistuning identification method, it is possible to identify multiple mistuning patterns. It is also possible to subsequently determine the locations of the physical mistuning sources. A method has also been proposed to improve the accuracy of such results using surrogate mistuning patterns and computing residuals using the identified physical parameters. The importance of the multiple mistuning patterns on the blisk modeling at higher modes has been highlighted.

Conceptually, the difficulties in choosing measurement points (and modes to be used in the IROM) are affected by two important factors. First, at higher frequencies, there is an increase in the complexity of the motion of the structure that makes systematically choosing sensitive and high responding data points difficult. Second, the modal density for blade-alone families is much lower at high frequencies than at low frequencies. This means that it is likely that the mistuned modes in a given frequency range can no longer be represented with the modes in that frequency range. Both of these issues conspire to make solving for the mistuning in higher frequency ranges impossible using current capabilities. Both of these issues must be addressed by using ROMs optimally created based on the modes with the highest sensitivity to mistuning and by using the most appropriate measurement points for those modes.

Due to more complicated blade response shapes at higher frequencies, the limitation of experimentally measuring only a few points per blade is very important. To select points that well represent the system mode shapes used in the CMM model, the EIDV procedure is used in an iterative manner for multiple sets of candidate modes in order to determine the best EIDV measurement points. This is done by first using a set of EIDV measurement points chosen from a candidate mode set. The mistuning identification procedure computes the EIDV measurement points for each considered IROM mode set. This allows for a better set of measurement points for the modes actually used in the identification procedure. These measurement points are more sensitive to mistuning and better able to represent the mode shapes used in the reduced-order model for predictions.

The proposed method has been validated numerically, but not experimentally. Some limitations related to experimental efficiency of the approach exist. For example, typically experimental data is likely to be gathered from an axial direction using a laser vibrometer. However, depending on the stagger angle and the curvature of the blade, availability of

measurement points might be limited. Furthermore, in much higher frequency ranges, the mode shapes of the system can become highly disk dominated making the blade response low. In such cases, noise in the measurement data is likely to create challenges. Nevertheless, overall the approaches presented in this work significantly enhance the identification and modeling of mistuning in higher frequency ranges. Therefore, this work helps enable the design and analysis of blisks throughout the entire operating range.

CHAPTER IV

Reduced Order Models for Large Geometric Mistuning of Blisks Based on Nested Component Mode Synthesis

4.1 Introduction

Accurate modeling of turbomachinery blisks is needed to ensure reliability and prevent high cycle fatigue failure. Modeling blisks using full order finite element models (FEMs) is inefficient, especially in the presence of mistuning. Mistuning can be small or large deviations in what is otherwise usually a cyclically symmetric blisk. It is often desirable to consider small mistuning from a probabilistic perspective, thus making the solution of full-order FEMs restrictive. Therefore, work in this area focuses mainly on the development of reduced order models (ROMs) to approximate the full-order FEM. Early work on blisk modeling focused primarily on small mistuning. Various efficient approaches for reduced order modeling of blisks with small mistuning have been developed [14, 16–18, 21–23]. The other category of mistuning is large mistuning. The distinction between large and small mistuning is that large mistuning cannot be accurately modeled by only a change in blade alone frequencies.

Recently, work related to modeling of blisks having large mistuning has emerged. Lim *et al.* [22] introduced a general ROM to model small and large mistuning based on using tuned modes and virtual mistuned components in a hybrid interface technique. The ba-

sis consisted of a truncated set of tuned normal modes, tuned-system attachment modes, and constraint modes for the mistuning components. The model had high accuracy, but resulted in models too large to be considered efficient ROMs. Lim *et al.* [44] changed direction and focused on a model based on static mode compensation that would efficiently model large mistuning only. This method projected the dynamics of the system onto tuned system modes compensated using quasi-static modes according to a mode acceleration approach, resulting in a dramatically smaller ROM. However, this model did not consider small mistuning. Ganine *et al.* [45] added the small, random mistuning to this approach in a similar manner to component mode mistuning [23], and continued the work [46] by studying the convergence properties of the static mode compensation (SMC) technique. It was noted that SMC is most appropriate only when modes are closely spaced and the FEM is not too large, whereas the Jacobi-Davidson algorithm had better convergence for large scale FEMs and regions where mode family interaction is important. Sinha [48] suggested a ROM where tuned modes for the basis are chosen based on proper orthogonal decomposition (POD) features. The ROM size can be rather large depending on the flexibility desired (i.e., depending on the number of POD features included).

This work suggests a different approach to large mistuning. As suggested in by Yang *et al.* [18], we first chose a basis of nominal system modes onto which the system can be projected. The basis consists of the modes of the rogue system (i.e., a system having large mistuning) in the absence of small mistuning. The basis is generated using fixed-interface component mode synthesis (CMS) [54] where the sector-to-sector interfaces are assumed to be the interface degrees of freedom (DOFs) used in the CMS procedure. These modes are computed using CMS in order to reduce the computational cost. Bladh *et al.* [16] used a CMS-based approach to model small mistuning. In their study, they considered the components to be each of the blades and the disk. However, current FEM of blisks have

a large number of DOFs at the blade-disk interface. Therefore, in this work each sector is viewed as a component and the sector-to-sector interfaces result in fewer DOF than blade-disk interfaces. Also noted in Bladh *et al.* [16] was the introduction of a secondary modal reduction to further reduce DOFs from the original reduction step. In this work, we propose a secondary CMS-based reduction that is done on only a portion of the ROM. This has the benefit of further reducing DOFs for which there is no need to access, while leaving the components associated with largely mistuned sectors free. In this manner, it is possible to rapidly generate ROMs of systems having differing rogue sectors. Ultimately, these ROMs are used to approximate the full nominal rogue mode shape (from systems having large mistuning, but no small mistuning). The system matrices are then projected onto these nominal rogue mode shapes.

The mistuned portions of the system matrices are further projected onto cantilevered blade modes using an extended component mode mistuning (CMM) approach [23]. This is done by projecting system modes of blade DOFs without large mistuning onto tuned cantilevered blade mode shapes as usual. However, the system modes of blade DOFs having large mistuning are projected onto rogue cantilevered blade mode shapes. This makes it possible to model large and small mistuning simultaneously, while allowing for the large mistuning to have any form (missing mass, bends, etc.).

4.2 Methodology

The basic method is inspired by the subset of nominal (SNM) [18] and component mode mistuning (CMM) [23] procedures. The concept in these works is that equations of motion can be reduced by projecting the mass and stiffness matrices onto the tuned system modes. This has been shown to work for frequency ranges where there is high modal density [56]. In CMM, the mistuned portions of the mass and stiffness matrices are further

projected onto tuned cantilevered blade modes through the system modes. This method has only been applied to systems that are nominally assumed to be cyclic symmetric or tuned.

The first modification to CMM for this method is the use of rogue system modes instead of tuned system modes in order to improve the basis. This allows the ROM to effectively capture the known large mistuning. This is also necessary to ensure that the base geometries of the system match. The other modification is that mistuning in the rogue blades is further projected onto the cantilevered blade modes of the rogue system. This leads to the need to project the system modes for the rogue blade onto a set of cantilevered blade modes from the same rogue blade. The final difference to the procedure used in CMM stems from the computation of the basis modes. For the small mistuning methodology where tuned modes are used, the tuned system modes are computed efficiently using cyclic symmetry analysis. However, in the large mistuning case where the otherwise-tuned rogue system modes are used, the rogue system modes cannot be computed using cyclic symmetry analysis. To efficiently compute the rogue system modes, a CMS routine is implemented. For the CMS technique, the interface DOF are those along what were previously considered sector interfaces. The system is reduced using CMS through a Craig-Bampton reduction, the modes are computed in the reduced space, and then expanded.

4.2.1 Computation of Rogue System Modes using CMS

Consider the equation of motion of an undamped, rogue blisk expressed as

$$\mathbf{M}^r\ddot{\mathbf{X}} + \mathbf{K}^r\mathbf{X} = \mathbf{F}, \tag{4.1}$$

where r denotes the rogue system. The vector $\mathbf{X}$ can be partitioned and represented using Craig-Bampton CMS reduction as

$$\mathbf{X} = \begin{bmatrix} \mathbf{X}_\alpha \\ \mathbf{X}_\beta \end{bmatrix} = \begin{bmatrix} \mathbf{\Phi}^r_\alpha & \mathbf{\Psi}^r_\alpha \\ \mathbf{0} & \mathbf{I} \end{bmatrix} \begin{bmatrix} \mathbf{P}^s_\Phi \\ \mathbf{P}^s_\Psi \end{bmatrix} = \mathbf{\Phi}^r_{CB}\mathbf{P}^r, \tag{4.2}$$

where α denotes internal DOFs, β denotes interface DOFs, s denote system level quantities, and CB denotes Craig-Bampton coordinate transformation from physical coordinates $\mathbf{X}$ to reduced coordinates ($\mathbf{P}^s_\Phi$ (removed) and $\mathbf{P}^s_\Psi$ (kept)). The DOFs associated with internal DOFs, $\mathbf{X}_\alpha$, are all of the DOF for each sector of the blisk, with the exception of the sector-to-sector interfaces. The remaining DOF, $\mathbf{X}_\beta$, are the sector-to-sector interfaces. The goal is to compute the modes of the blisk governed by Eq. 4.2. To do this, the mass and stiffness matrices are projected onto the Craig-Bampton matrix as follows

$$\mathbf{M}_{CB} = {\mathbf{\Phi}^r_{CB}}^{\mathrm{T}}\mathbf{M}^r\mathbf{\Phi}^r_{CB}, \tag{4.3}$$

$$\mathbf{K}_{CB} = {\mathbf{\Phi}^r_{CB}}^{\mathrm{T}}\mathbf{K}^r\mathbf{\Phi}^r_{CB}. \tag{4.4}$$

Using the reduced mass and stiffness matrices from Eqs. 4.3 and 4.4, the mode shapes for this reduced system can be found (and denoted Φ_{red}), as well as the eigenvalues of the full system, $\mathbf{\Lambda}^{red}$, where red denotes reduced. To obtain the complete modal information for the full rogue system, $\mathbf{\Phi}^r$ and $\mathbf{\Lambda}^r$, the reduced mode shapes are expanded as follows

$$\mathbf{\Phi}^r = \mathbf{\Phi}^r_{CB}\mathbf{\Phi}_{red}. \tag{4.5}$$

This way of computing the basis vectors is useful because it is possible to rapidly change the rogue blade to consider an alternate case due to the component nature of the approach. To consider a different rogue blade, it is only necessary to compute the normal and constraint modes for the new rogue sector.

4.2.2 Secondary CMS Reduction for Rogue System Modes

It may be desirable to compute many responses associated with systems having different rogue sectors. The CMS-based approach allows for the rapid replacement of a component such as a rogue sector without reducing the remaining components of the model again. Bladh *et al.* [16] suggested a CMS-based approach, but the component interfaces were between the blade and the disk. This was necessary for the projection of small mistuning. This work has no such restriction because CMM has the unique property that small mistuning is projected through mode shapes. In this work, we switch to using the interface between the sectors because it is noted in many industrial blisks, the number of DOFs on the interface between a single blade and a disk is far greater than the number of DOFs on the sector-to-sector interface. Bladh *et al.* [16] also introduced a secondary modal analysis on the CMS-reduced model to further reduce DOFs. Here, it is not desirable to reduce the model again using a secondary modal analysis because then it is impossible to quickly swap out rogue sectors. Instead, it is proposed here to perform an additional CMS substructuring procedure to reduce interface DOF while still allowing for the rogue sectors to not undergo additional reduction. In this manner, the total number of DOFs of the ROM used to compute mode shapes can be reduced to speed up calculations. At the same time, the reduction procedure can still be performed rapidly.

Consider again

$$\mathbf{X} = \begin{bmatrix} \mathbf{X}_\alpha \\ \\ \mathbf{X}_\beta \end{bmatrix} = \begin{bmatrix} \boldsymbol{\Phi}^r_\alpha & \boldsymbol{\Psi}^r_\alpha \\ \\ \mathbf{0} & \mathbf{I} \end{bmatrix} \begin{bmatrix} \mathbf{P}^s_\Phi \\ \\ \mathbf{P}^s_\Psi \end{bmatrix}. \tag{4.6}$$

The kept DOFs, $\mathbf{P}^s_\Psi$ can be further partitioned into DOFs to be kept,$\mathbf{P}^s_{\Psi_\Psi}$, and DOFs to be

reduced,$\mathbf{P}^s_{\Psi_\Phi}$ in the secondary reduction. This leads to

$$\begin{bmatrix} \mathbf{X}_\alpha \\ \mathbf{X}_\beta \end{bmatrix} = \begin{bmatrix} \boldsymbol{\Phi}^r_\alpha & \boldsymbol{\Psi}^r_{\alpha_\Phi} & \boldsymbol{\Psi}^r_{\alpha_\Psi} \\ \mathbf{0} & \mathbf{I} & \mathbf{I} \end{bmatrix} \begin{bmatrix} \mathbf{P}^s_\Phi \\ \mathbf{P}^s_{\Psi_\Phi} \\ \mathbf{P}^s_{\Psi_\Psi} \end{bmatrix}. \tag{4.7}$$

One then allows the substitutions

$$\begin{bmatrix} \boldsymbol{\Phi}^r_\alpha & \boldsymbol{\Psi}^r_{\alpha_\Phi} \\ \mathbf{0} & \mathbf{I} \end{bmatrix} = \begin{bmatrix} \tilde{\boldsymbol{\Phi}}^r_\alpha \\ \tilde{\boldsymbol{\Phi}}^r_\beta \end{bmatrix}, \quad \mathbf{P}^s_{\tilde{\Phi}} = \begin{bmatrix} \mathbf{P}^s_\Phi \\ \mathbf{P}^s_{\Psi_\Phi} \end{bmatrix}, \tag{4.8}$$

for convenience of writing the matrix equations. Using this substitution, Eq. 4.7 can be written as

$$\begin{bmatrix} \mathbf{X}_\alpha \\ \mathbf{X}_\beta \end{bmatrix} = \begin{bmatrix} \tilde{\boldsymbol{\Phi}}^r_\alpha & \boldsymbol{\Psi}^r_{\alpha_\Psi} \\ \tilde{\boldsymbol{\Phi}}^r_\beta & \mathbf{I} \end{bmatrix} \begin{bmatrix} \mathbf{P}^s_{\tilde{\Phi}} \\ \mathbf{P}^s_{\Psi_\Psi} \end{bmatrix}. \tag{4.9}$$

Now, the secondary reduction can be applied using CMS by letting

$$\begin{bmatrix} \mathbf{P}^s_\Phi \\ \mathbf{P}^s_{\Psi_\Psi} \end{bmatrix} = \begin{bmatrix} \boldsymbol{\Phi}^r_{\text{nest}} & \boldsymbol{\Psi}^r_{\text{nest}} \\ \mathbf{0} & \mathbf{I} \end{bmatrix} \begin{bmatrix} \mathbf{P}^s_{\Phi_{\text{nest}}} \\ \mathbf{P}^s_{\Psi_{\text{nest}}} \end{bmatrix} = \boldsymbol{\Phi}^{\text{nest}}_{CB} \mathbf{P}^{\text{nest}}, \tag{4.10}$$

where nest denotes nesting or secondary modal reduction. Here $\boldsymbol{\Phi}^r_{\text{nest}}$ is computed from a fixed interface modal analysis on the system defined by Eqs. 4.3 and 4.4 on the modal DOFs, $\mathbf{P}^s_{\tilde{\Phi}}$. Similarly, the constraint modes, $\boldsymbol{\Psi}^r_{\text{nest}}$, are computed from the system defined by Eqs. 4.3 and 4.4 on the modal DOFs $\mathbf{P}^s_{\Psi_\Psi}$. The resulting system is defined as

$$\mathbf{M}^{\text{nest}}_{CB} = {\boldsymbol{\Phi}^{\text{nest}}_{CB}}^{\text{T}} \mathbf{M}_{CB} \boldsymbol{\Phi}^{\text{nest}}_{CB}, \tag{4.11}$$

$$\mathbf{K}^{\text{nest}}_{CB} = {\boldsymbol{\Phi}^{\text{nest}}_{CB}}^{\text{T}} \mathbf{K}_{CB} \boldsymbol{\Phi}^{\text{nest}}_{CB}, \tag{4.12}$$

This nesting can be performed similarly multiple times in order to obtain more reduction. Also, the reduction can be performed in several components in order to avoid solving one large modal analysis, given a large number of constraint DOFs from the initial reduction step.

4.2.3 CMM-Based ROM for Large Mistuning

Modeling of both large and small mistuning are discussed in this section. The analysis provided here is condensed from a longer analysis which is provided in the Appendix to this work.

Consider the equation of motion of a damped, harmonically forced, rogue mistuned blisk expressed as

$$-\omega^2 \left[\mathbf{M}^r + \mathbf{M}^\delta\right] \mathbf{X} + (1 + j\gamma) \left[\mathbf{K}^r + \mathbf{K}^\delta\right] \mathbf{X} = \mathbf{f}^r, \tag{4.13}$$

where r denotes the nominal rogue system, γ is the structural damping coefficient, δ denotes small mistuning. It was determined by Yang *et al.* [56] that mistuned modes in a high modal density region can be represented using tuned modes in the same region. We further this assumption that the system modes of a nominally rogue system with small mistuning can be represented using the rogue modes without small mistuning. This means that all static constraint modes may be ignored and we transform to modal coordinates using the transformation $\mathbf{X} = \mathbf{\Phi}^r \mathbf{p}^r_\Phi$. This yields

$$-\omega^2 {\mathbf{\Phi}^r}^{\mathrm{T}} \left[\mathbf{M}^r + \mathbf{M}^\delta\right] \mathbf{\Phi}^r \mathbf{p}^r_\Phi + (1 + j\gamma) {\mathbf{\Phi}^r}^{\mathrm{T}} \left[\mathbf{K}^r + \mathbf{K}^\delta\right] \mathbf{\Phi}^r \mathbf{p}^r_\Phi = {\mathbf{\Phi}^r}^{\mathrm{T}} \mathbf{f}^r, \tag{4.14}$$

It is noted that the $\mathbf{\Phi}^r$ is mass normalized. Also, it is noted that mistuning is assumed to be in the blade DOFs (Γ) only. This yields the equation

$$-\omega^2 \left[\ \mathbf{I} + {\mathbf{\Phi}^r_\Gamma}^{\mathrm{T}} \mathbf{M}^\delta \mathbf{\Phi}^r_\Gamma \ \right] \mathbf{p}^r_\Phi + (1 + j\gamma) \left[\ \mathbf{\Lambda}^r + {\mathbf{\Phi}_\mathbf{\Gamma}}^{r\,\mathrm{T}} \mathbf{K}^\delta \mathbf{\Phi}^r_\Gamma \ \right] \mathbf{p}^r_\Phi = {\mathbf{\Phi}^r}^{\mathrm{T}} \mathbf{f}^r. \tag{4.15}$$

It is desirable to represent the blade portion of the system normal modes with a set of component modes of a tuned blade or rogue blade in this extension of the method. For

convenience, Eq. 4.15 can be expressed as

$$-\omega^2 \left[\mathbf{I} + {\mathbf{\Phi}_\Gamma^r}^{\mathrm{T}} \begin{bmatrix} \mathbf{M}_{ii}^\delta & \mathbf{M}_{ib}^\delta \\ \mathbf{M}_{bi}^\delta & \mathbf{M}_{bb}^\delta \end{bmatrix} \mathbf{\Phi}_\Gamma^r \right] \mathbf{p}_\Phi^r + ... \\ + (1 + j\gamma) \left[\mathbf{\Lambda}^r + {\mathbf{\Phi}_\Gamma^r}^{\mathrm{T}} \begin{bmatrix} \mathbf{K}_{ii}^\delta & \mathbf{K}_{ib}^\delta \\ \mathbf{K}_{bi}^\delta & \mathbf{K}_{bb}^\delta \end{bmatrix} \mathbf{\Phi}_\Gamma^r \right] \mathbf{p}_\Phi^r = {\mathbf{\Phi}^r}^{\mathrm{T}} \mathbf{f}^r. \tag{4.16}$$

Lim *et al.* [23] minimized the contribution of the constraint modes and found the following relationship between the blade portion of the system modes and the component modes of the cantilevered blade modes

$$\mathbf{\Phi}_\Gamma^r = \begin{cases} \left(\mathbf{I} \otimes \begin{bmatrix} \mathbf{\Phi}^b & \mathbf{\Psi}^{b,m} \\ \mathbf{0} & \mathbf{I} \end{bmatrix} \right) \begin{bmatrix} \mathbf{q}_\Phi^m \\ \mathbf{q}_\Psi^m \end{bmatrix} \\ \text{or} \\ \left(\mathbf{I} \otimes \begin{bmatrix} \mathbf{\Phi}^b & \mathbf{\Psi}^{b,k} \\ \mathbf{0} & \mathbf{I} \end{bmatrix} \right) \begin{bmatrix} \mathbf{q}_\Phi^k \\ \mathbf{q}_\Psi^k \end{bmatrix} \end{cases}, \tag{4.17}$$

where b denotes cantilevered blade.

Next, Eq. 4.17 is substituted into Eq. 4.17. If one assumes that the boundary portion of the blade motion is relatively small, and one ignores the contribution of boundary modes, Eq. 4.17 becomes

$$-\omega^2 \left[\mathbf{I} + \sum_{n=1}^{N} {\mathbf{q}_{\Phi,n}^m}^{\mathrm{T}} {\mathbf{\Phi}^b}^{\mathrm{T}} \mathbf{M}_{ii,n}^\delta \mathbf{\Phi}^b \mathbf{q}_{\Phi,n}^m \right] \mathbf{p}_\Phi^r + ... \\ ... + (1 + j\gamma) \left[\mathbf{\Lambda}^r + \sum_{n=1}^{N} {\mathbf{q}_{\Phi,n}^k}^{\mathrm{T}} {\mathbf{\Phi}^b}^{\mathrm{T}} \mathbf{K}_{ii,n}^\delta \mathbf{\Phi}^b \mathbf{q}_{\Phi,n}^k \right] \mathbf{p}_\Phi^r = {\mathbf{\Phi}^r}^{\mathrm{T}} \mathbf{f}^r, \tag{4.18}$$

where the blade portion of the rogue system normal mode is represented solely using a basis of cantilevered blade normal modes. Finally, it is assumed that mass mistuning does not exist, and ${\mathbf{\Phi}^b}^{\mathrm{T}} \mathbf{K}_{ii,n}^\delta \mathbf{\Phi}^b$ is approximated with $\mathbf{\Lambda}_n^{\delta,b}$ to obtain

$$-\omega^2 \mathbf{p}_\Phi^r + (1 + j\gamma) \left[\mathbf{\Lambda}^r + \sum_{n=1}^{N} {\mathbf{q}_{\Phi,n}^k}^{\mathrm{T}} \mathbf{\Lambda}_n^{\delta,b} \mathbf{q}_{\Phi,n}^k \right] \mathbf{p}_\Phi^r = {\mathbf{\Phi}^r}^{\mathrm{T}} \mathbf{f}^r, \tag{4.19}$$

where $\mathbf{\Lambda}_n^{\delta,b}$ are the differences in the tuned cantilevered blade eigenvalues from the mistuned cantilevered blade eigenvalues.

4.3 Results

In this section, a brief discussion of studies related to this method are presented. Most of the results discussed are related to the rogue FEM shown in Fig. 4.1(a). The model has a single blade with large geometric mistuning shown in Fig. 4.1(b) as well as small mistuning in all blades.

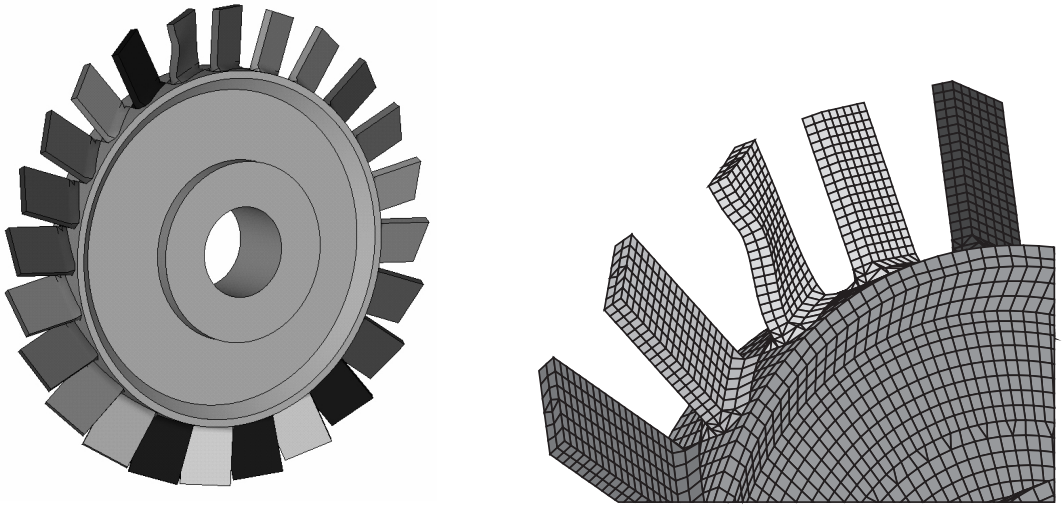

(a) FEM of a blisk with 24 blades and 1 rogue blade.

(b) Close up view of rogue blade.

Figure 4.1: Overview of the rogue FEM of a blisk with 24 blades.

4.3.1 Nominal Rogue System Modal Basis

The current CMM based large mistuning ROM requires a basis of nominal rogue system modes. Nominal rogue system modes are those that have a blade with some large mistuning, but are otherwise tuned. The CMM approach developed by Lim *et al.* [23] used for small mistuning only assumes that tuned system modes can span the space of

the mistuned modes. Figure 4.2(a) shows the residual when the tuned modes are used to represent the mistuned modes. The residual is small over all of the modes, and therefore the assumption holds. To demonstrate the tuned modes cannot represent a nominal rogue system without small mistuning, a similar residual is shown in Fig. 4.2(b). The residual is roughly an order of magnitude greater than the previous case, verifying that tuned modes cannot be used as a basis for large mistuning. The CMM used for large mistuning assumes that the rogue system with mistuning can be represented by the rogue system modes without mistuning. Figure 4.2(c) shows that the residual is small, and therefore is a suitable basis for modeling large and small mistuning using the CMM procedure.

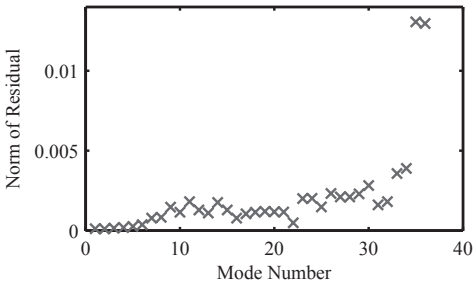

(a) Relative residual from representing mistuned (small) modes with tuned modes.

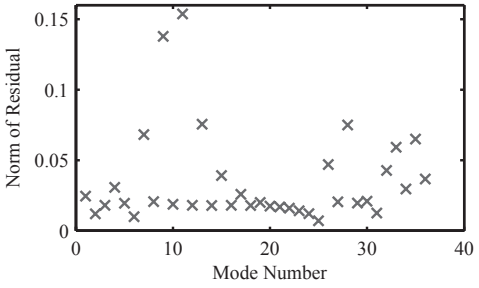

(b) Relative residual from representing mistuned (large) modes with tuned modes.

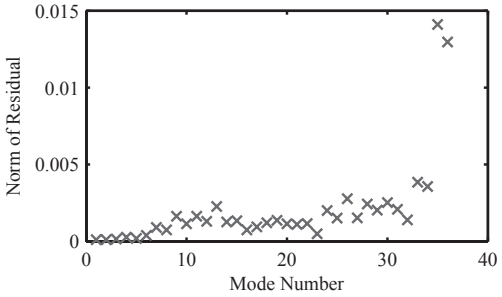

(c) Relative residual from representing mistuned (large and small) modes with nominal mistuned modes.

Figure 4.2: Relative residual from representing mistuned modes with tuned modes.

Because the basis no longer comes from a tuned model, it is no longer possible to use

cyclic symmetry analysis to compute the modes. Therefore, a CMS approach is implemented in order to efficiently compute the nominal rogue system modes. To do this, each component must be chosen such that rogue blades are separate components from tuned blades. It is possible to consider the disk as one component and all of the blades as separate components. Due to the fact that the root of the blade experiences high stresses and therefore is modeled with more nodes, it proved more advantageous to consider each sector as a separate component. The sector interfaces are not modeled with as many nodes, and therefore the number on constraint modes that need to be computed is reduced.

Using 30 normal modes and all of the constraint modes for each component yielded rogue modes that closely matched those computed from a full FEM for a frequency range of 0-5000 Hz. Figure 4.3(a) shows the modal assurance criterion (MAC) for the CMS and FEM generated modes. The MAC is nearly unity for all modes, showing that the modes are nearly the same. A close eigenvalue match can be seen in Fig. 4.3(b). Therefore, it is possible to efficiently compute the rogue system modes using CMS without appreciable loss in accuracy as compared to the the FEM solution. The solution using CB-CMS is

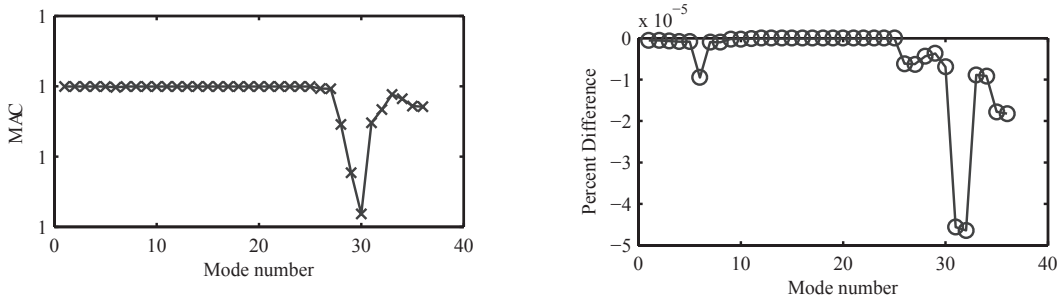

(a) Modal assurance criterion for modes computed using full FEM vs. CMS.

(b) Eigenvalue comparison for modes computed using full FEM vs. CMS.

Figure 4.3: Comparison of modes computed using full FEM vs. CMS.

accurate enough to approximate the desired nominal rogue modes. However, the number of constraint modes on the interface can result a system that is still large. Furthermore, the

sparsity of the system matrices decreases and therefore the eigensolver cannot make use of algorithms based on sparsity. Therefore, it is desirable to further reduce the system using nested substructuring. It is possible to substructure the entire CB-CMS ROM as in Bladh *et al.* [16]. However, it is preferable to maintain access to rogue components in order to simply swap components. Therefore, two different levels of nesting are considered. The first is 2-sector nesting where two adjacent sector components are combined into a single component. This is repeated around the blisk. The second is a 4-sector nesting, where 4 adjacent sectors are combined into a single component.

Table 4.1 compares the number of DOFs at each step in the reduction/expansion procedure for the blisk used Fig. 4.1(a). It is noted that the both 2-sector and 4-sector nesting

	Number of DOFs for 2-sector nesting	Number of DOFs for 4-sector nesting
Full Model	47040	47040
1st CB-CMS	22656	22656
2nd CB-CMS	11328	5664
ROM Modal Analysis	11328	5664
1st Expansion	22656	22656
2nd Expansion	47040	47040

Table 4.1: Comparison of modes computed using full FEM vs. nested CMS.

procedures have 22656 DOFs at the first CB-CMS reduction step. It is the secondary reduction where the 2-sector nesting has 11328 DOFs and the 4-sector nesting has 5664 DOFs where the difference is seen. The second CB-CMS reduction is also where it was decided to compute the modal analysis of the entire system. Therefore, it is significantly more efficiently to do repetitive calculations on the 4-sector nested model. Finally, it is clear that the two expansion steps lead to the same number of DOF until the full model prediction is reached. Figure 4.3.1 demonstrates that there is no appreciable difference in

accuracy for the natural frequencies of the system between the 2-sector or 4-sector nesting algorithms. It is also noted that both of these predictions match the full-order FEM solution well.

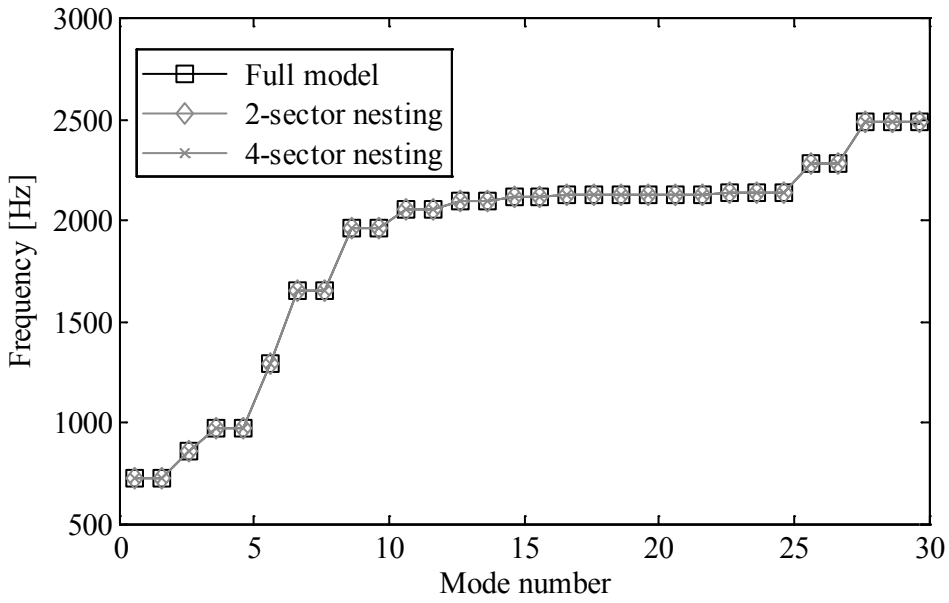

Figure 4.4: Natural frequencies of the nominal rogue blisk computed using nested CMS.

An important consideration in this analysis is the time that it takes to generate the ROM. It is desirable to be able to rapidly generate ROMs for large mistuning. Figure 4.5 shows both the processing time and actual elapsed time for the 2-sector nesting to be performed in ANSYS®. It is noted that the largest processing time was consumed relatively equally between the nesting, modal analysis, and the expansion steps. Reduction of the components and translating a single component to make the full model are nearly negligible in processing time. However, it is important to consider the actual elapsed time due to memory concerns. Due to creation of and writing of large amounts of data internally, it is clear that the full expansion of the modes begins to dominate the computation time.

Similarly, the computational time for 4-sector nesting was considered. In this case, it is

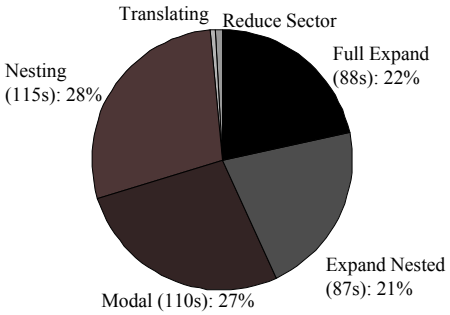

(a) CPU time for 2-sector nesting.

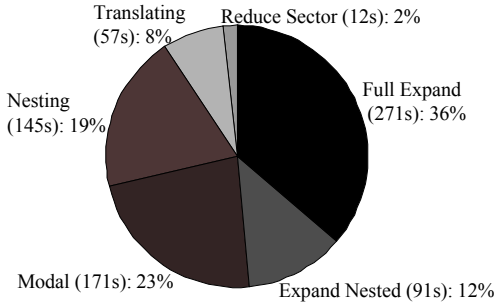

(b) Elapsed time for 2-sector nesting.

Figure 4.5: Breakdown of computation time for 2-sector nesting.

clear that the nesting step becomes more expensive and dominates the processing time. However, it is still surpassed by the full modal expansion in actual elapsed time. It is noted that the final modal analysis in 4-sector nesting is performed on a system with much fewer DOFs than in 2-sector nesting. This results in a dramatic reduction in modal analysis costs.

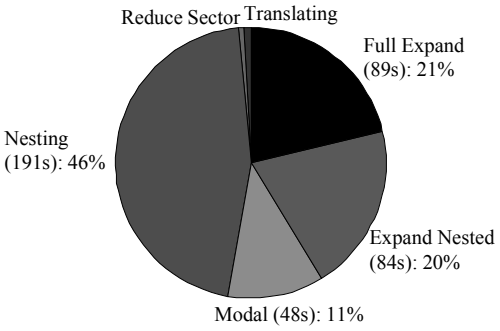

(a) CPU time for 4-sector nesting.

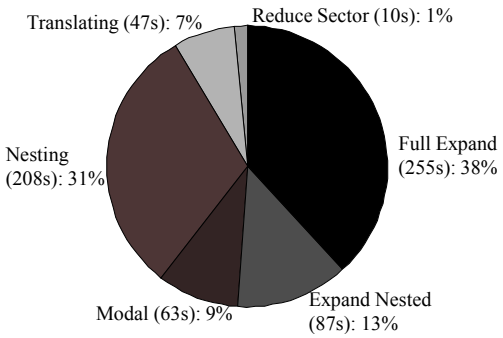

(b) Elapsed time for 4-sector nesting.

Figure 4.6: Breakdown of computation time for 4-sector nesting.

The use of CMS to compute the nominal rogue modes is done to increase efficiency. Table 4.2 compares the total time to generate full system modes using a full modal analysis,

	CPU time (s)	Elapsed time (s)
Full modal analysis	81	123
2-sector nested ROM	406	745
4-sector nested ROM	418	671

Table 4.2: Computational time for 2-sector and 4-sector nested CMS methods.

2-sector nesting, and 4-sector nesting. Clearly, simply computing modes using the full modal analysis is the least expensive in terms of total time while 2-sector nesting is the most expensive. The full modal analysis however, must be performed in its entirety each time a new rogue system is considered. Furthermore, for the cases of industrial blisks having a much larger number of DOFs, a full modal analysis will become prohibitively inefficient or impossible.

An interesting result is that the final modal analysis for the 2-sector nesting actually takes more time than the full-order modal analysis even though the 2-sector ROM has far fewer DOFs. This is likely caused by the lack of sparsity in the CMS-reduced system. In this case, the sparse eigensolver cannot be used, likely resulting increased computational time. Therefore, it suggested that the DOFs must be more reduced to create a beneficial ROM.

Considering again Figs. 4.5 and 4.6, it is clear that a significant portion of time is spent either doing the intermediate CB-CMS step or in expanding the modes. Therefore, if only a component or two must be swapped to consider a new rogue system, the efficiency will increase relative to the full analysis. The commercial FE code ANSYS® was used to perform the nesting and expansion of the system. It is noted that ANSYS® generates a significant amount of large files and consumes a lot of the memory resources available. This is one explanation for why the elapsed time is significantly greater than the CPU time.

In the case of, large industrial rotors, the use of ANSYS® to perform this reduction is likely to be prohibitive. It is suggested, to perform the expansion outside of ANSYS® for only the needed DOFs to improve computational efficiency.

4.3.2 CMM-based Large Mistuning ROM vs. FEM

With a basis of nominal rogue modes, the CMM procedure is applied. This provides an efficient means for exploring the space of small mistuning patterns for a given large mistuning scenario. As described in Lim *et al.* [23], CMM makes use of a few assumptions that can affect the accuracy of the results. First, the basis vectors used should span the space of the actual mode shapes of the mistuned system, which was addressed in Section 4.3.1. Since the blade portion of the mode shapes is represented by cantilevered blade (CB) modes alone for the purpose of mistuning projection, it is required that the CB modes can well represent the system mode. Also, the mistuning is more accurately captured if the motion between the blade and the disk is small.

Figure 4.7(a) shows the natural frequencies given a system with large and small mistuning for both FEM and ROM. Figure 4.7(b) shows the percentage error in the eigenvalues assuming that the FEM is the baseline. The eigenvalues show good agreement, having an error of under 0.1 %. It is important that this error is small as it is likely of interest to detect mistuning on the order of 1 % of the change in an eigenvalue. In order to predict stress levels in blisks, it is necessary to obtain an accurate prediction of the response over the operating frequency range. Therefore, one of the main purposes of the ROM is to predict the frequency response. Figure 4.8 shows the frequency response of 10 DOF for all 24 blades. The frequency response shows good agreement for nearly all frequencies. It is noted that for a few specific frequencies, it appears that there are some amplitude discrepancies. However, the envelope of the response appears to be captured well.

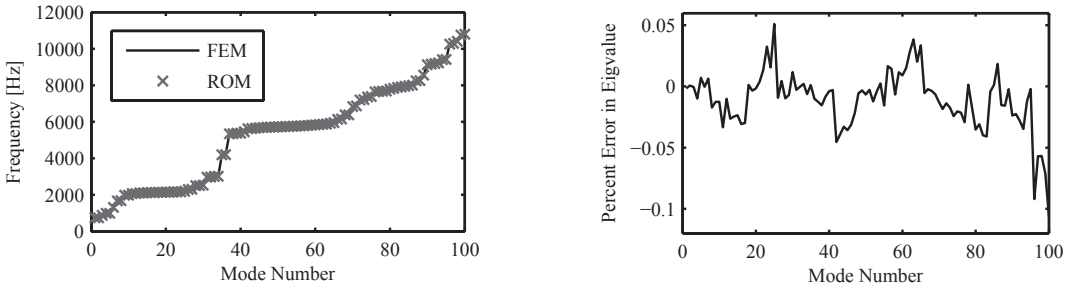

(a) Natural frequencies computed from FEM and ROM.

(b) Eigenvalue comparison for modes computed using FEM vs. ROM.

Figure 4.7: Comparison of eigenvalues computed using full FEM vs. ROM.

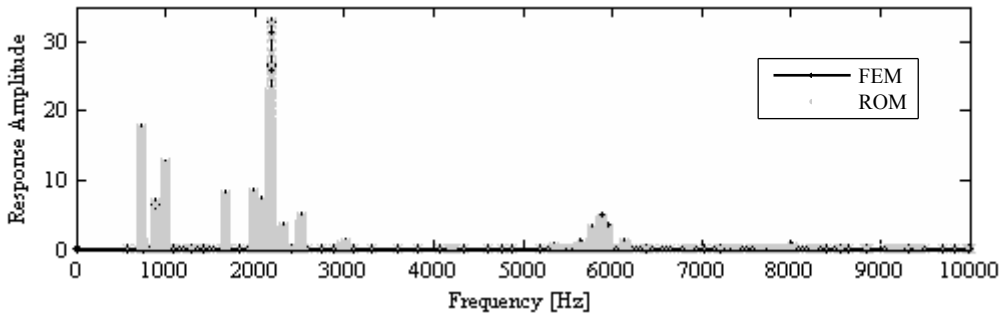

Figure 4.8: Comparison between FEM vs. ROM frequency response.

4.4 Conclusions and Future Work

This work introduced a new ROM for modeling large and small mistuning together. The ROM is based on CMM having nominal rogue system modes as a basis. It was demonstrated that the tuned system modes cannot serve as a basis for a system having large mistuning because the mode shapes between the large mistuned system and the tuned system are different. It was then shown that using nominal rogue system modes could be used to represent the modes of a system with large and small mistuning for a given frequency range. Therefore, the use of nominal rogue systems modes is justified as a basis for the CMM procedure.

Because the rogue system is not cyclically symmetric as would be the case if the system were tuned, CMS was used to compute the mode shapes. Because individual blades need to be isolated, and many DOF exist at the blade-disk interface which would result in a high number of constraint modes, the components were defined as the sectors. It was demonstrated that the modes can be computed using CMS without loss of accuracy as compared to FEM. To further improve efficiency of the CMS technique for computing nominal rogue modes, secondary reductions were considered. Both 2-sector and 4-sector nesting resulted in trade off between up front computational cost and computational costs associated with repeatability. The up front costs for 4-sector nesting are greater, but the 4-sector nesting method has the potential for lower computational costs if a number of components need to be changed and the ROM regenerated. Both nesting sizes result in accurate mode shapes relative to the full-order FEM mode shapes.

Finally, a the CMM-based large mistuning ROM was assembled and compared with FEM results. The eigenvalues were predicted within 0.1 % of the FEM. The frequency response predictions were accurate at almost all frequencies, and the envelope of the re-

sponse was captured well. The ROM will offer the possibility of getting accurate response amplitudes for a given system with large mistuning for random small mistuning.

One possible direction for future work is computation of the rogue system modes more efficiently than is done with CMS. Even with sector boundaries as interface DOF, the number of constraint modes results in matrices that are still moderately large and lack sparsity. Another suggestion for future work is to explore improvements to CMM, namely adding constraint modes at the interface of the blade and disk for the projection of mistuning. This might improve the amplitude predictions for the frequencies that were not predicted with high accuracy. Finally, this approach will only handle one discrete large mistuning scenario. To explore another large mistuning case, the nominal rogue system mode basis must be recomputed. A possible direction for future work is to parameterize the large damage which will allow for rapid exploration of large mistuning cases in conjunction with random small mistuning.

CHAPTER V

Pristine, Rogue, Interface Modal Expansion (PRIME): A Reduced Order Modeling Approach For Blisks With Large Mass, Stiffness And Geometric Mistuning

5.1 Introduction

Industrial turbomachinery blisks are often nominally cyclically symmetric by design. Deviations to the cyclic symmetry of these blisks is common due to manufacturing, general wear, and damage. These deviations, called mistuning, can lead to dramatically increased forced response for a few of the blades of the blisks. Because of the need to predict the forced response and the need to avoid high stress situations, various techniques to construct reduced order models (ROM) have been developed. These techniques can be divided into two categories. The first tackles small mistuning only. These methods assume that the mistuning is small enough to be modeled as small frequency deviations of the blades (e.g. 10% change in blade alone frequencies). Small mistuning has been studied extensively, and several efficient approaches for reduced-order modeling of mistuned bladed disks have been developed [14, 16–18, 21–23]. The second category tackles large mistuning. In contrast to small mistuning, large mistuning cannot be accurately modeled by only small frequency deviations. Blisks with large mistuning are usually characterized by simultaneous large mass, stiffness, and geometric changes to the nominally tuned sys-

tem. Such mistuning occurs for cases where blades have large deformations or missing material.

Limited work has been done for developing ROMs for blisks with large mistuning. Lim et al. [22] developed a modeling technique to encompass both small and large mistuning. Those ROMs use tuned modes and virtual mistuned components in a component mode synthesis (hybrid interface) technique. The resulting basis consists of a truncated set of tuned normal modes, tuned-system attachment modes, and constraint modes for the mistuning components. However, this method results in prohibitively large models. Following their work, an approach to address large mistuning specifically in order to reduce the model size was proposed [44] . This method projects the blisk dynamics onto a basis of tuned system modes compensated using quasi-static modes according to a mode acceleration approach. The models obtained by this approach are much smaller, but they do not consider small, random mistuning. Ganine et al. [45] added the small, random mistuning to the static mode compensation (SMC) approach in a similar manner to component mode mistuning (CMM) [23]. This was followed by a study of the convergence properties of the SMC technique and a suggestion for a new technique based on a Jacobi-Davidson correction of the modes [46] . It was noted that SMC is most appropriate only when modes are closely spaced and the finite element model (FEM) is not too large, whereas the Jacobi-Davidson had better convergence for large scale FEM and regions where mode family interaction is important. A unique approach was suggested by Sinha [47, 48] where tuned modes are chosen for the basis based on proper orthogonal decomposition (POD) features. The ROM size generated by that approach can be larger than SMC based ROMs since it is the product of the number of tuned modes and the number of POD features, but the approach allows for the possibility to model random large mistuning. These approaches all make use of full system modes or variations of full system modes for a basis.

An exciting approach was introduced recently by Mbaye et al. [49, 50] to consider blisks with intentional geometric mistuning with the possibility of adding random mistuning [51]. In this approach, cyclic symmetry analysis is applied to each individual sector to compute modes to be used in the basis for reduction. Cyclic symmetry modes are then strategically assembled according to the physical degrees of freedom (DOFs) corresponding to each sector to build up each full mode shape. To do this, it was necessary to introduce a modal scale factor to match phases and ultimately modify the modes of each sector before compatibility was enforced on the interface. This unique approach offers a convenient and efficient way to model a system that is intentionally geometrically mistuned.

The work of Mbaye et al. [49] focuses on intentional mistuning. The current work builds on that by extending the cyclic modes approach and improving the basis to accurately model all varieties of geometric mistuning, notably large bends and missing material. These improvements are important needed generalizations for a variety of reasons. For example, in the approach by Mbaye et al. [49], the modal scaling factor is computed using the inner product between a nominal sector and the sectors of the actual system. This factor cannot be directly applied to a system having missing material because the number of DOFs do not match from sector to sector. For systems with bends, this factor could also lead to a false phase matching because the actual location of the DOFs between adjacent sectors are different. Additionally, since each of the cyclic modes for each sector are assembled for the same mode without additional normalization (other than enforcing compatibility at the interfaces), it is possible that the basis could be insufficient for certain systems which have large parameter changes. Such an example is a case where only the modulus of elasticity is changed for one entire sector. In this case, the mode shapes for the modified sector would be the same as the tuned sector. This would make the basis in this

approach precisely the tuned system modes. However, it is well known that the mistuned system with a large enough change in modulus of elasticity cannot be modeled using tuned system modes [23]. Finally, we found that the constraints imposed on the basis are overly constraining the model and they have to be relaxed to model large damage. Cyclic modes computed using cyclic symmetry analysis for each sector are assembled for each given mode in the basis. This likely leads to a full basis of modes that have non-localized behaviors even in the presence of cyclic rogue modes. That phenomenon leads to an inaccurate mode. For example, a case where some of the DOFs have a very small motion is likely to occur (especially in a localized mistuned system). An extreme example of this is a case where all of the energy is localized in a single sector, such as would likely occur when there is a single damaged blade.

The current work introduces a new reduced order modeling approach for both large and small mistuning. The method first determines a suitable set of basis vectors to model a nominal rogue system, upon which small mistuning will ultimately be projected. This approach makes use of a new basis composed of modes computed only from cyclic symmetry analyses (for the tuned and rogue sectors, where rogue sectors are the sectors having large differences from the tuned sector). This is similar to the method Mbaye et al. [49] from the viewpoint that this method needs only cyclic symmetric modes to reduce the system, but the basis is assembled differently to add flexibility to the system and improve accuracy. In our method, the system matrices are projected onto a three part basis. This basis has DOF associated with the three distinct portions of the system: the pristine portion which is geometrically the same as the nominal tuned system, the rogue portion which consists of the physical DOF of the system that has large mistuning, and the interface portion which consists of the physical DOF which interface the rogue and pristine physical DOF of the system. By allowing additional DOF associated with the distinct physical locations (the

interface), the basis can satisfy the compatibility between the pristine and rogue portions. Also, the need to match phases between physical DOF of the system is eliminated. Furthermore, the additional DOFs prevent the reduced system from becoming overly stiff (or locking) and therefore can model extreme cases of energy localization.

ROMS are computed by first projecting only sector level system matrices onto sector level cyclic mode shapes, thus preventing high computational cost while forming the basis. After a ROM is formed, a series of computationally efficient transformations are applied to effectively remove unnecessary DOF in a manner that further reduces the system without overly constraining it. The result is a compact basis that can serve as a set of nominal modes not unlike that suggested in work by Yang et al. [18]. Also, this approach is particularly efficient in regions of high modal density [56].

The new set of modes can serve as a basis of nominal modes upon which an extension of CMM can be applied. The extension of CMM was first suggested by Ganine et al. [45] in which the modes associated with blades having geometric mistuning are projected onto cantilevered blade modes of that geometrically mistuned blade. Using this concept, the mode shapes of the new basis are projected on the corresponding tuned or rogue cantilevered blade modes for the mistuned portion of the system matrices. This final ROM has the key advantages that it requires only cyclic sector-level or blade alone computations, and it uses only sector-level information and data manipulation. Hence, the model reduction can be applied to highly refined, realistic models of industrial size with low computational costs.

5.2 Modeling

This section introduces a novel methodology to accurately and efficiently model the dynamics of a system having both large and small mistuning. First, a new reduced basis

upon which the equations of motion of a system with large mistuning can be projected to accurately model the dynamics is discussed. It is also discussed how this basis can model small mistuning by an extension of the CMM method [23]. Next, a methodology is presented to demonstrate how this projection can be done using only sector level calculations. Finally, a method for further reducing the ROM size based on intermediate subspace projections is described.

5.2.1 Pristine-Rogue-Interface Modal Expansion (PRIME)

The equations of motion of a full blisk can be reduced by projecting the mass and stiffness matrices onto the nominal system modes [18], and then further projecting the mistuned portions of the mass and stiffness matrices onto appropriate cantilevered blade modes through the nominal system modes. The pristine-rogue-interface modal expansion (PRIME) methodology is shown schematically in Figs. 5.1 and 5.2. First, it is well known that the full geometrically mistuned mode shape cannot be represented by a basis of tuned system modes [23]. This is shown in Fig. 5.1. However, it is assumed that the physical DOFs represented by the pristine portion of the geometrically mistuned mode can be represented by the corresponding physical DOFs from a tuned modal basis, as shown in Fig. 5.1. Similarly, it is clear that the full geometrically mistuned mode shape cannot be represented by a basis of cyclic rogue system modes, as shown on the bottom of Fig. 5.2. By the same reasoning as for the pristine DOFs of the system, it is assumed that the rogue DOFs of the full mode shape can be represented by the rogue DOF of the cyclic rogue modes as in Fig. 5.2. For simplicity, consider the equation of motion of an undamped rogue blisk expressed for harmonic forcing as

$$\left[-\omega^2\mathbf{M}+\mathbf{K}\right]\mathbf{x}=\mathbf{f}. \tag{5.1}$$

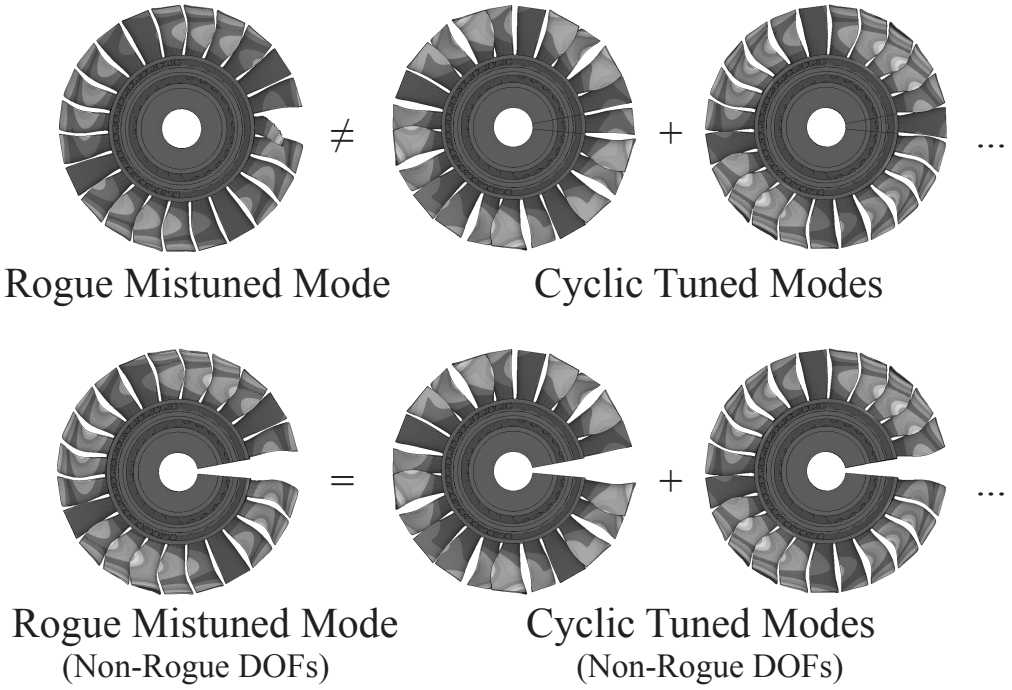

Figure 5.1: Evaluation of tuned system modes as a basis.

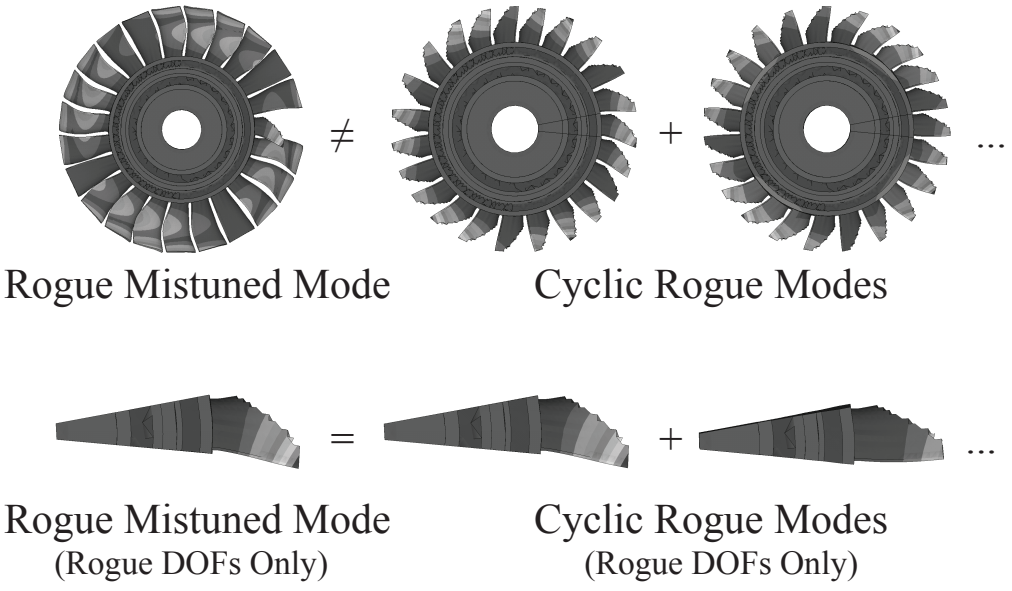

Figure 5.2: Evaluation of cyclic rogue system modes as a basis.

The equations can be partitioned as follows:

$$\left\{ -\omega^2 \begin{bmatrix} \mathbf{M}^{PP} & \mathbf{M}^{PR} & \mathbf{M}^{PI} \\ \mathbf{M}^{RP} & \mathbf{M}^{RR} & \mathbf{M}^{RI} \\ \mathbf{M}^{IP} & \mathbf{M}^{IR} & \mathbf{M}^{II} \end{bmatrix} + ... \right. \\ \left. ... + \begin{bmatrix} \mathbf{K}^{PP} & \mathbf{K}^{PR} & \mathbf{K}^{PI} \\ \mathbf{K}^{RP} & \mathbf{K}^{RR} & \mathbf{K}^{RI} \\ \mathbf{K}^{IP} & \mathbf{K}^{IR} & \mathbf{K}^{II} \end{bmatrix} \right\} \begin{bmatrix} \mathbf{x}^P \\ \mathbf{x}^R \\ \mathbf{x}^I \end{bmatrix} = \begin{bmatrix} \mathbf{f}^P \\ \mathbf{f}^R \\ \mathbf{f}^I \end{bmatrix}, \tag{5.2}$$

where P denotes the pristine (or non-rogue) portion of the blisk, R is the rogue portion of the blisk, and I is the interface between the pristine and rogue parts of the system. It is now proposed that the system matrices be projected onto a new basis using the transformation

$$\mathbf{x} = \begin{bmatrix} \mathbf{x}^P \\ \mathbf{x}^R \\ \mathbf{x}^I \end{bmatrix} = \begin{bmatrix} \mathbf{\Phi}^P & \mathbf{0} & \mathbf{0} \\ \mathbf{0} & \mathbf{\Phi}^R & \mathbf{0} \\ \mathbf{0} & \mathbf{0} & \mathbf{\Phi}^I \end{bmatrix} \begin{bmatrix} \mathbf{p}_{\phi_P} \\ \mathbf{p}_{\phi_R} \\ \mathbf{p}_{\phi_I} \end{bmatrix} = \mathbf{\Phi}^{PRI}\mathbf{p}, \tag{5.3}$$

where $\mathbf{\Phi}^P$ is a truncated set of cyclic modes (assembled) for the pristine sectors, $\mathbf{\Phi}^R$ is a truncated set of cyclic modes for the rogue sectors, and $\mathbf{\Phi}^I$ is a truncated set of cyclic modes for the interface between rogue and pristine sectors. A key feature of this basis is that the pristine, rogue, and interface physical DOFs all have separate DOFs in the modal space. This is critical because it allows the basis to effectively span the subspace of the original modes of the geometrically mistuned system without locking certain DOFs or overly constraining the system. Projecting the equations of motion yields the reduced

system

$$
\begin{aligned}
\mathbf{M}_{PRI} &= \begin{bmatrix} \boldsymbol{\Phi}^{P\mathrm{T}}\mathbf{M}^{PP}\boldsymbol{\Phi}^{P} & \boldsymbol{\Phi}^{P\mathrm{T}}\mathbf{M}^{PR}\boldsymbol{\Phi}^{R} & \boldsymbol{\Phi}^{P\mathrm{T}}\mathbf{M}^{PI}\boldsymbol{\Phi}^{I} \\ \boldsymbol{\Phi}^{R\mathrm{T}}\mathbf{M}^{RP}\boldsymbol{\Phi}^{P} & \boldsymbol{\Phi}^{R\mathrm{T}}\mathbf{M}^{RR}\boldsymbol{\Phi}^{R} & \boldsymbol{\Phi}^{R\mathrm{T}}\mathbf{M}^{RI}\boldsymbol{\Phi}^{I} \\ \boldsymbol{\Phi}^{I\mathrm{T}}\mathbf{M}^{IP}\boldsymbol{\Phi}^{P} & \boldsymbol{\Phi}^{I\mathrm{T}}\mathbf{M}^{IR}\boldsymbol{\Phi}^{R} & \boldsymbol{\Phi}^{I\mathrm{T}}\mathbf{M}^{II}\boldsymbol{\Phi}^{I} \end{bmatrix}, \\
\mathbf{K}_{PRI} &= \begin{bmatrix} \boldsymbol{\Phi}^{P\mathrm{T}}\mathbf{K}^{PP}\boldsymbol{\Phi}^{P} & \boldsymbol{\Phi}^{P\mathrm{T}}\mathbf{K}^{PR}\boldsymbol{\Phi}^{R} & \boldsymbol{\Phi}^{P\mathrm{T}}\mathbf{K}^{PI}\boldsymbol{\Phi}^{I} \\ \boldsymbol{\Phi}^{R\mathrm{T}}\mathbf{K}^{RP}\boldsymbol{\Phi}^{P} & \boldsymbol{\Phi}^{R\mathrm{T}}\mathbf{K}^{RR}\boldsymbol{\Phi}^{R} & \boldsymbol{\Phi}^{R\mathrm{T}}\mathbf{K}^{RI}\boldsymbol{\Phi}^{I} \\ \boldsymbol{\Phi}^{I\mathrm{T}}\mathbf{K}^{IP}\boldsymbol{\Phi}^{P} & \boldsymbol{\Phi}^{I\mathrm{T}}\mathbf{K}^{IR}\boldsymbol{\Phi}^{R} & \boldsymbol{\Phi}^{I\mathrm{T}}\mathbf{K}^{II}\boldsymbol{\Phi}^{I} \end{bmatrix}, \qquad (5.4) \\
\mathbf{F}_{PRI} &= \begin{bmatrix} \boldsymbol{\Phi}^{P\mathrm{T}}\mathbf{f}^{P} \\ \boldsymbol{\Phi}^{R\mathrm{T}}\mathbf{f}^{R} \\ \boldsymbol{\Phi}^{I\mathrm{T}}\mathbf{f}^{I} \end{bmatrix}.
\end{aligned}
$$

PRIME-Based ROMs Computed Using Sector Level Calculations.

Formation of ROMs can be computationally expensive in itself due the increasing model sizes being used for industrial blisks. Furthermore, it is becoming increasingly more common to use Matlab to rapidly manipulate and form ROMs. However, memory usage can become prohibitive to forming bases associated with industrial models. For this purpose, we present next a technique to form the PRIME basis using *only sector level calculations*, which ultimately eliminates the need to form large memory-consuming matrices.

Let us first consider the projection of the mass matrix of a tuned blisk onto the normal modes of the system. The standard projection in Fig. 5.3 shows the assembled mass matrix and corresponding mode shapes. Figure 5.4 shows a disassembled projection. The mass matrix is comprised of block matrices $\mathbf{M}_1 \cdots \mathbf{M}_N$ for N sectors. Each matrix $\mathbf{M}_i$ is the free-interface mass matrix for a sector. The modal matrix is similarly composed of $\boldsymbol{\Phi}_1 \cdots \boldsymbol{\Phi}_N$, where each $\boldsymbol{\Phi}_i$ has the system level mode shape for all of the DOFs for a

sector (including its interfaces with adjacent sectors. It should be noted that there is duplicated modal information at each sector interface of $\mathbf{\Phi}_i$. To assemble the matrix in Fig. 5.4 according to a finite element assembly, the parts of the mass matrix corresponding to interface DOFs are summed, and the duplicate interface modal information is removed from each $\mathbf{\Phi}_i$. Consider the expressions which represent mathematically the two projections

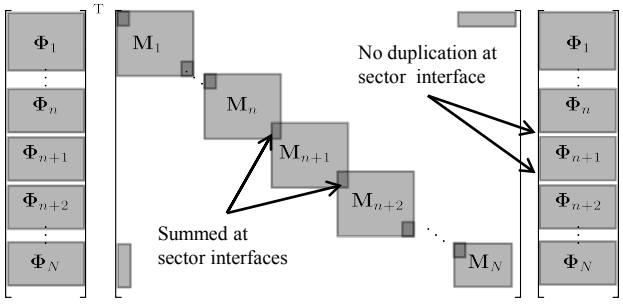

Figure 5.3: Standard modal projection of mass matrix onto normal modes.

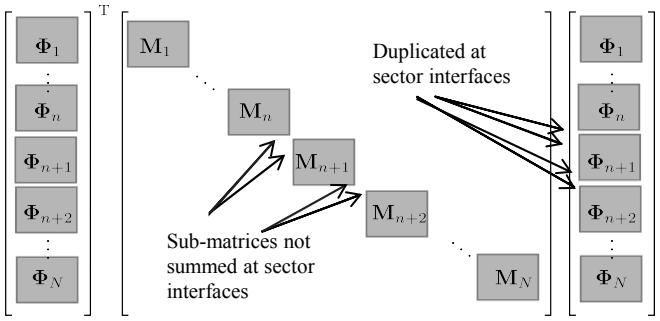

Figure 5.4: Expanded modal projection of mass matrix onto normal modes.

(at interface DOFs) shown in Figs. 5.3 and 5.4, respectively

$$\mathbf{\Phi}_i^{\Gamma\mathrm{T}} \left[\mathbf{M}_i^{\Gamma} + \mathbf{M}_{i+1}^{\Gamma}\right] \mathbf{\Phi}_i^{\Gamma}, \tag{5.5}$$

and

$$\mathbf{\Phi}_i^{\Gamma\mathrm{T}} \mathbf{M}_i^{\Gamma} \mathbf{\Phi}_i^{\Gamma} + \mathbf{\Phi}_{i+1}^{\Gamma\ \mathrm{T}} \mathbf{M}_{i+1}^{\Gamma} \mathbf{\Phi}_{i+1}^{\Gamma}, \tag{5.6}$$

where Γ denotes interface DOF. It is clear that if $\mathbf{\Phi}_{i+1}^{\Gamma} = \mathbf{\Phi}_{i}^{\Gamma}$, then the expressions in Eqns. 5.5 and 5.6 are also equal. The equality of the duplicate modal interfaces and the summation in the mass matrix interfaces upon assembly makes the projections in Figs. 5.3 and 5.4 precisely identical. Therefore, we turn our attention to the expanded projection in Fig. 5.4. It has the advantageous property that it can be computed using only free-interface sector mass matrices, and sector level portions of the system modal matrices. The entire expansion can be done by only forming matrices and vectors having the size of the number of DOFs in a single sector. It is clear that this concept can be applied to the stiffness matrix as well. This principle works especially well for projections involving tuned cyclic models because the entire mode shape is *never* computed.

This idea is applied to the PRIME basis. First, we must replace the appropriate pristine sector mass matrices in Fig. 5.4 with the rogue sector mass matrix for the rogue portions of the system. Similarly, we replace the corresponding sector level tuned mode shapes with the sector level rogue mode shapes (which are computed from cyclic symmetry analysis). Only the interfaces between the rogue and pristine sector mode shapes do not precisely match. However, it is assumed that all of the rogue sector interfaces can be expressed as a linear combination of pristine interfaces. This allows for the PRIME basis to be computed fully having only matrices of the size of a single sector model necessary in memory, thus expanding the possible models that can be handled.

Large and Small Mistuning: Extended CMM with PRIME

Consider the equation of motion of a system having both large and small mistuning

$$\left[-\omega^2 \left(\mathbf{M} + \mathbf{M}^{\delta}\right) + \left(\mathbf{K} + \mathbf{K}^{\delta}\right)\right] \mathbf{x} = \mathbf{f}, \tag{5.7}$$

where δ denotes the presence of mistuning in the blade portion of the system only. The entire mistuned system is projected onto the PRIME basis, which results in the following

reduction

$$\begin{aligned}\Big[-\omega^2 {\mathbf{\Phi}^{PRI}}^{\mathrm{T}} \left(\mathbf{M}+\mathbf{M}^{\delta}\right) \mathbf{\Phi}^{PRI} + ... \\ ... + {\mathbf{\Phi}^{PRI}}^{\mathrm{T}} \left(\mathbf{K}+\mathbf{K}^{\delta}\right) \mathbf{\Phi}^{PRI}\Big] \mathbf{p} = {\mathbf{\Phi}^{PRI}}^{\mathrm{T}} \mathbf{f},\end{aligned} \tag{5.8}$$

and can be written as

$$\begin{aligned}\Big[-\omega^2 \left(\mathbf{M}^{PRI} + {\mathbf{\Phi}^{PRI}}^{\mathrm{T}} \mathbf{M}^{\delta} \mathbf{\Phi}^{PRI}\right) + ... \\ ... + \left(\mathbf{K}^{PRI} + {\mathbf{\Phi}^{PRI}}^{\mathrm{T}} \mathbf{K}^{\delta} \mathbf{\Phi}^{PRI}\right)\Big] \mathbf{p} = {\mathbf{\Phi}^{PRI}}^{\mathrm{T}} \mathbf{f}.\end{aligned} \tag{5.9}$$

At this point, the mistuned portion of the system matrices are projected onto either pristine or rogue cantilevered blade normal modes (neglecting constraint modes) in a modified CMM [23] approach by allowing the PRIME modal basis to be represented by a combination of cantilever blade modes. The projection is only necessary for blade DOFs since mistuning is only present in the blades for this study. The projection has the following form

$$\begin{aligned}\mathbf{\Phi}^{P} = \mathrm{Bdiag}\left[\mathbf{\Phi}_{cb}^{P}\right] \mathbf{q}^{P}, \\ \mathbf{\Phi}^{R} = \mathrm{Bdiag}\left[\mathbf{\Phi}_{cb}^{R}\right] \mathbf{q}^{R},\end{aligned} \tag{5.10}$$

where $\mathrm{Bdiag}[\cdot]$ refers to a block diagonal matrix, cb denotes cantilevered blade, and the vectors $\mathbf{q}^{P}$ and $\mathbf{q}^{R}$ have distinct entries for each cantilevered blade mode used for each blade on the blisk. The resulting reduced system matrices can be written as

$$\begin{aligned}\mathbf{M}^{red} &= \mathbf{M}^{PRI} + \sum_{n=1}^{N} \mathbf{q}_n^{\mathrm{T}} {\mathbf{\Phi}_n^{cb}}^{\mathrm{T}} \mathbf{M}_n^{\delta} \mathbf{\Phi}_n^{cb} \mathbf{q}_n, \\ \mathbf{K}^{red} &= \mathbf{K}^{PRI} + \sum_{n=1}^{N} \mathbf{q}_n^{\mathrm{T}} {\mathbf{\Phi}_n^{cb}}^{\mathrm{T}} \mathbf{K}_n^{\delta} \mathbf{\Phi}_n^{cb} \mathbf{q}_n,\end{aligned} \tag{5.11}$$

where the mistuned portion of the system can be written as a sum of the projections over each of the N blades. By ignoring mass mistuning and assuming that the motion of each blade is dominated by a single cantilevered blade mode, the matrices in Eqn. 5.11 can be reduced as done by Lim et al. [23] to obtain

$$\begin{aligned} \mathbf{M}^{red} &= \mathbf{M}^{PRI}, \\ \mathbf{K}^{red} &= \mathbf{K}^{PRI} + \sum_{n=1}^{N} \mathbf{q}_n^{\mathrm{T}} \delta\mathbf{\Lambda}^{cb} \mathbf{q}_n, \end{aligned} \tag{5.12}$$

where $\delta\mathbf{\Lambda}^{cb}$ are the eigenvalue deviations of the mistuned cantilevered blade modes from the tuned ones. The portion of the system with small mistuning requires only the solution of the rogue and tuned cantilevered blade eigenvalue problem and simple projections to compute the participation factors as follows

$$\begin{aligned} \mathbf{q}^{P} &= {\mathbf{\Lambda}_{cb}^{P}}^{-1} {\mathbf{\Phi}_{cb}^{P}}^{\mathrm{T}} \mathbf{K}_b \mathbf{\Phi}_b^{R}, \\ \mathbf{q}^{R} &= {\mathbf{\Lambda}_{cb}^{R}}^{-1} {\mathbf{\Phi}_{cb}^{R}}^{\mathrm{T}} \mathbf{K}_b \mathbf{\Phi}_b^{P}, \end{aligned} \tag{5.13}$$

where the subscript b denotes blade DOFs. The ROM in Eqn. 5.12 represents a complete model which efficiently and accurately models large geometric mistuning and damage as well as small mistuning.

PRIME Conditioning

The PRIME basis introduced in Eqn. 5.3 has several differences from that suggested by Mbaye et al. [49], most notably that the pristine, rogue, and interface DOFs in the physical space are each also allowed separate DOFs in the modal space. This approach removes the need to do phase matching between sector interfaces, eliminates the need to have a criteria to match mode families and nodal diameter content of each sector, and ultimately allows for a model that is flexible enough to model extreme cases of geometric modification.

However, there are two aspects of the new method which can be improved. The first, and most obvious, is that the resulting ROM has additional DOFs which reduce efficiency when doing probabilistic studies using the ROM. The second is that the matrix shown in Eqn. 5.3 has the potential to be rank deficient. Consider the full cyclic rogue system matrix $\boldsymbol{\phi}^R \in \mathbb{R}^{\gtrdot \curvearrowright \gtrdot}$ and the submatrix $\tilde{\boldsymbol{\Phi}}^R \in \mathbb{R}^{\alpha \curvearrowright \gtrdot}$ which is used in PRIME (before truncation). Here, m denotes the number of physical DOF for a full system, and α denotes the physical DOF for a single sector. It is clear that $rank\{\tilde{\boldsymbol{\Phi}}^R\} < m$. This is an extreme example of how the PRIME basis can become ill-conditioned. That is more likely to occur when there is low disk motion within a mode family because of the similarity amongst the mode shapes. Two important improvements are presented next to address these issues.

Consider Eqn. 5.5 which shows the PRIME ROM. We first consider the reduced mass matrix with the understanding that the same operations are applied to the stiffness and forcing terms. Substitute $\boldsymbol{\mu}^{xy} = \boldsymbol{\Phi}^{x\mathrm{T}}\mathbf{M}^{xy}\boldsymbol{\Phi}^{y}$ for notational convenience such that

$$\mathbf{M}_{PRI} = \begin{bmatrix} \boldsymbol{\mu}^{PP} & \boldsymbol{\mu}^{PR} & \boldsymbol{\mu}^{PI} \\ \boldsymbol{\mu}^{RP} & \boldsymbol{\mu}^{RR} & \boldsymbol{\mu}^{RI} \\ \boldsymbol{\mu}^{IP} & \boldsymbol{\mu}^{IR} & \boldsymbol{\mu}^{II} \end{bmatrix}. \tag{5.14}$$

Next, perform a transformation to constrain the DOFs in the system as follows

$$\begin{aligned} \boldsymbol{\mu} &= \begin{bmatrix} \mathbf{I} & \mathbf{0} \\ \mathbf{I} & \mathbf{I} \\ \mathbf{I} & \mathbf{0} \end{bmatrix}^{\mathrm{T}} \begin{bmatrix} \boldsymbol{\mu}^{PP} & \boldsymbol{\mu}^{PR} & \boldsymbol{\mu}^{PI} \\ \boldsymbol{\mu}^{RP} & \boldsymbol{\mu}^{RR} & \boldsymbol{\mu}^{RI} \\ \boldsymbol{\mu}^{IP} & \boldsymbol{\mu}^{IR} & \boldsymbol{\mu}^{II} \end{bmatrix} \begin{bmatrix} \mathbf{I} & \mathbf{0} \\ \mathbf{I} & \mathbf{I} \\ \mathbf{I} & \mathbf{0} \end{bmatrix}, \\ &= \begin{bmatrix} \tilde{\boldsymbol{\mu}}^{PRI} & \tilde{\boldsymbol{\mu}}^{R\Gamma} \\ \tilde{\boldsymbol{\mu}}^{R\Gamma^{\mathrm{T}}} & \tilde{\boldsymbol{\mu}}^{RR} \end{bmatrix}, \end{aligned} \tag{5.15}$$

where

$$\begin{aligned}
\tilde{\boldsymbol{\mu}}^{PRI} &= \boldsymbol{\mu}^{PP} + \boldsymbol{\mu}^{PR} + \boldsymbol{\mu}^{PI} + \boldsymbol{\mu}^{RP} + ... \\
&... \quad + \boldsymbol{\mu}^{RR} + \boldsymbol{\mu}^{RI} + \boldsymbol{\mu}^{IP} + \boldsymbol{\mu}^{IR} + \boldsymbol{\mu}^{II}, \\
\tilde{\boldsymbol{\mu}}^{R\Gamma} &= \boldsymbol{\mu}^{RP} + \boldsymbol{\mu}^{RR} + \boldsymbol{\mu}^{RI}, \\
\tilde{\boldsymbol{\mu}}^{RR} &= \boldsymbol{\mu}^{RR}.
\end{aligned}$$

At this point, the model has a disadvantage similar to that of Mbaye et al. [49] where the system is overly constrained. From the viewpoint of the PRIME basis, one could write this last transformation as a

$$\mathbf{p}_{red} = \begin{bmatrix} \boldsymbol{\Phi}^P & \mathbf{0} \\ \boldsymbol{\Phi}^R & \boldsymbol{\Phi}^R \\ \boldsymbol{\Phi}^I & \mathbf{0} \end{bmatrix} \begin{bmatrix} \mathbf{p}_{\phi_{PRI}} \\ \mathbf{p}_{\phi_R} \end{bmatrix}. \tag{5.16}$$

Note that there is no matching of mode families for the sector modes in the left hand column. The main problem is that the modal DOFs associated with the rogue information, $\mathbf{p}_{\phi_R}$ are not completely free to move relative to the rest of the DOFs, $\mathbf{p}_{\phi_{PRI}}$. Due to this it is necessary to keep only the portion of $\boldsymbol{\Phi}^R$ associated with the portion of $\mathbf{p}_{\phi_R}$ which is in the numerical null space of the interface motion. This will essentially completely unlock the $\mathbf{p}_{\phi_R}$ DOFs, thus increasing the space of admissible displacements. The projection onto the null space is done by first solving the generalized eigenvalue problem of $\boldsymbol{\mu}^{II}\mathbf{V}^I = \boldsymbol{\Lambda}^I\mathbf{V}^I$. We have chosen to use the mass matrix eigenvalue problem to approximate the null space to ensure that the norm of the vectors is similar to the rest of the basis. By selecting the eigenvectors $\tilde{\mathbf{V}}^I$ associated with eigenvalues $\tilde{\boldsymbol{\Lambda}}^I$ that are essentially zero, it is possible to

form a null space of the interface. This leads to the transformation

$$\begin{aligned}\overline{\boldsymbol{\mu}} &= \begin{bmatrix} \mathbf{I} & \mathbf{0} \\ \mathbf{0} & \tilde{\mathbf{V}}^I \end{bmatrix}^{\mathrm{T}} \begin{bmatrix} \tilde{\boldsymbol{\mu}}^{PRI} & \tilde{\boldsymbol{\mu}}^{R\Gamma} \\ \tilde{\boldsymbol{\mu}}^{R\Gamma^{\mathrm{T}}} & \tilde{\boldsymbol{\mu}}^{RR} \end{bmatrix} \begin{bmatrix} \mathbf{I} & \mathbf{0} \\ \mathbf{0} & \tilde{\mathbf{V}}^I \end{bmatrix} \\ &= \begin{bmatrix} \tilde{\boldsymbol{\mu}}^{PRI} & \tilde{\boldsymbol{\mu}}^{R\Gamma}\tilde{\mathbf{V}}^I \\ \tilde{\mathbf{V}}^{I^{\mathrm{T}}}\tilde{\boldsymbol{\mu}}^{R\Gamma^{\mathrm{T}}} & \tilde{\mathbf{V}}^{I^{\mathrm{T}}}\tilde{\boldsymbol{\mu}}^{RR}\tilde{\mathbf{V}}^I \end{bmatrix}.\end{aligned} \tag{5.17}$$

Finally, to avoid the potential rank deficiency, the rogue modal DOFs are further projected onto the range space of the rogue DOFs. To accomplish this, in a similar fashion as for Eqn. 5.17, the eigenvalue problem $\left[\tilde{\mathbf{V}}^{R^{\mathrm{T}}}\tilde{\boldsymbol{\mu}}^{RR}\tilde{\mathbf{V}}^I\right]\mathbf{V}^R = \boldsymbol{\Lambda}^R\mathbf{V}^R$ is solved and the eigenvectors $\tilde{\mathbf{V}}^R$ associated with the largest eigenvalues $\tilde{\boldsymbol{\Lambda}}^R$ are retained. This leads to a similar transformation

$$\begin{aligned}\boldsymbol{\mu}_{red} &= \begin{bmatrix} \mathbf{I} & \mathbf{0} \\ \mathbf{0} & \tilde{\mathbf{V}}^R \end{bmatrix}^{\mathrm{T}} \begin{bmatrix} \tilde{\boldsymbol{\mu}}^{PRI} & \tilde{\boldsymbol{\mu}}^{R\Gamma}\tilde{\mathbf{V}}^I \\ \tilde{\mathbf{V}}^{I^{\mathrm{T}}}\tilde{\boldsymbol{\mu}}^{R\Gamma^{\mathrm{T}}} & \tilde{\mathbf{V}}^{I^{\mathrm{T}}}\tilde{\boldsymbol{\mu}}^{RR}\tilde{\mathbf{V}}^I \end{bmatrix} \begin{bmatrix} \mathbf{I} & \mathbf{0} \\ \mathbf{0} & \tilde{\mathbf{V}}^R \end{bmatrix} \\ &= \begin{bmatrix} \tilde{\boldsymbol{\mu}}^{PRI} & \tilde{\boldsymbol{\mu}}^{R\Gamma}\tilde{\mathbf{V}}^I\tilde{\mathbf{V}}^R \\ \tilde{\mathbf{V}}^{R^{\mathrm{T}}}\tilde{\mathbf{V}}^{I^{\mathrm{T}}}\tilde{\boldsymbol{\mu}}^{R\Gamma^{\mathrm{T}}} & \tilde{\mathbf{V}}^{R^{\mathrm{T}}}\tilde{\mathbf{V}}^{I^{\mathrm{T}}}\tilde{\boldsymbol{\mu}}^{RR}\tilde{\mathbf{V}}^I\tilde{\mathbf{V}}^R \end{bmatrix}.\end{aligned} \tag{5.18}$$

A similar reduced matrix can be computed for the stiffness matrix. The resulting ROM is significantly smaller than the original PRIME model. Furthermore, the matrices are well conditioned and result in accurate predictions. Note that the conditioning steps are done entirely in a reduced dimensional space. Hence, this step requires very small amounts of memory and the computational time is very low.

5.3 Results and Discussion

The PRIME methodology is applied to an industrial blisk with 23 blades shown in Fig. 5.5. For simplicity the system is considered to be undamped and to have only small stiffness mistuning. Nonetheless, the missing material is large and leads to large mistuning. Three cases are considered, each having different amounts of mass removed as shown

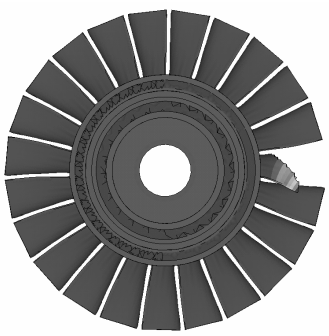

Figure 5.5: A mode shape localized at a rogue blade (mode index 70 in Fig. 5.7).

Fig. 5.6. The case having 90% missing mass from the blade represents an extreme case which demonstrates the effectiveness of the PRIME method. For convenience, a blisk having only missing mass is referred to as a rogue blisk, whereas a blisk having both missing mass and small mistuning is referred to has a rogue mistuned blisk.

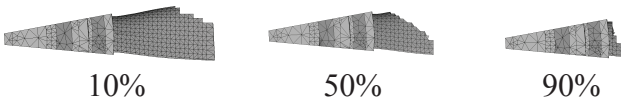

Figure 5.6: Rogue sectors with 10%, 50%, and 90% missing mass.

The first case considered is that of a rogue blisk having 50% missing mass from a single blade. Figure 5.7 shows a percent difference in the system natural frequencies between a full-order FEM and PRIME of less than 0.03%. The PRIME ROM size of 147 modes was used to model 79 modes. As noted earlier, relaxation of the constraints of the current approach is critical to be able to predict a highly localized mode shape at a rogue sector. Figure 5.5 represents the mode of index 70 (in Fig. 5.7). Although, this mode has the highest error, the accuracy is still good, thus demonstrating that PRIME can handle this extreme case. Another case noted earlier is one in which an entire sector has a uniform change in the modulus of elasticity. Because the modified sector has the same mode shapes as the nominally tuned system, the basis of Mbaye et al. will be one of

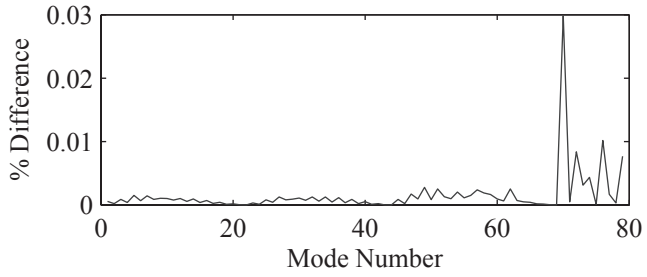

Figure 5.7: PRIME vs. FEM comparison of natural frequencies of a rogue mistuned blisk having a sector with 50% missing mass.

tuned system modes. However, if the change in the modulus of elasticity is large enough, a basis of tuned system modes is not capable of providing high-accuracy results. The conditioning feature of PRIME described in the methodology unlocks the model, thus preventing the PRIME basis from viewing that rogue sector as tuned. Figure 5.8 shows the percent difference in natural frequencies for a case where a single sector has a 40% modulus of elasticity increase. Again, even for this extreme case, the PRIME ROM predict the natural frequencies to within 0.25% error.

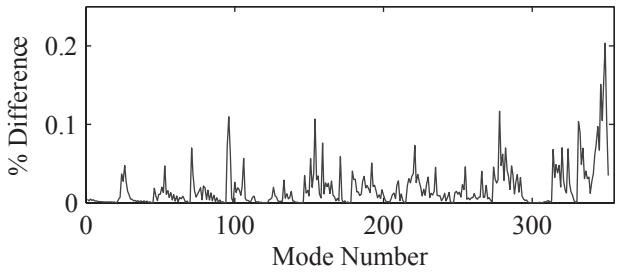

Figure 5.8: PRIME vs. FEM comparison of natural frequencies of a rogue mistuned blisk having a sector with 40% modulus of elasticity increase.

The PRIME methodology can also be used to approximate systems with both large and small mistuning. Figure 5.9(a) shows the natural frequency comparison from a system having small mistuning and a single sector with 10% missing mass. The ROM has a total of 478 DOFs which can accurately model 354 modes. Note that the accuracy begins

to decrease near the higher frequencies. However, the basis used contains pristine and interface modes only from 0-30kHz, which is the frequency range of natural frequencies compared. It is also notable that in the case of missing mass, the rogue sector natural frequencies dramatically increase, and therefore frequency content greater than 30kHz was used for the rogue cyclic modes only. For clarity, we kept the same number of rogue modes as pristine modes for these results. However, this likely results in a model that is larger than necessary to capture the natural frequencies in the range 0-30kHz. Similar results are shown for 50% and 90% missing mass in Figs. 5.9(b) and 5.9(c), respectively. The case with 10% missing mass requires a model with 510 DOFs to capture all frequencies from 0-30kHz, and the case with 90% missing mass requires 544 DOFs. Both cases show excellent accuracy especially away from the higher frequency range. Also of note is that the tuned system natural frequencies of these systems can be as much as 20% different from those of the mistuned system. An example of this can be seen in Fig. 5.10, where it is obvious that the mistuned rogue natural frequencies deviate significantly from the tuned natural frequencies. The values of natural frequency are plotted relative to a reference frequency value.

To demonstrate that the PRIME methodology fully captures the system dynamics for a rogue mistuned blisk, the mode shapes are compared. To do this, we compare the FEM mode with the PRIME mode for a node of two localized modes. The first mode is the mode shape is shown in Fig. 5.11 and the second mode shape is shown in Fig. 5.7. The mode shapes for the node (R, θ, and Z directions) shown in Fig. 5.11 are plotted in Fig. 5.12. The Z-axis is along the blisk center of rotation, the R-direction is outward from the blisk center of rotation, and the θ-direction is in the circumferential direction about the blisk center of rotation. It is clear that the PRIME basis can accurately predict the mode shapes of the rogue mistuned blisk even in the presence of localization. Furthermore, it can predict the

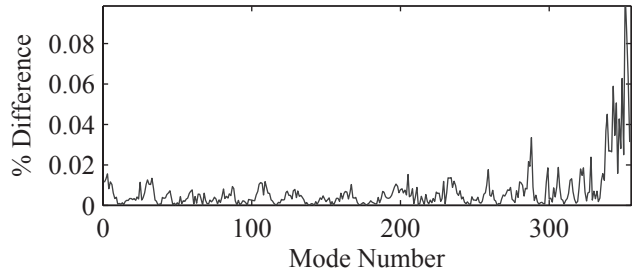

(a) 10% Mass Reduction.

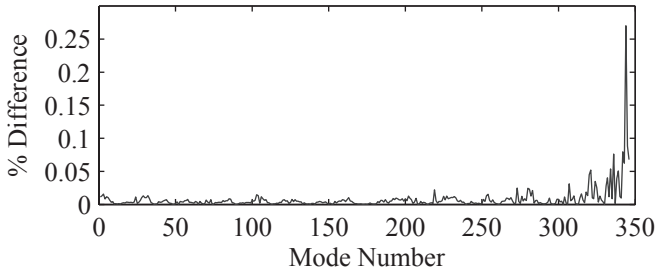

(b) 50% Mass Reduction.

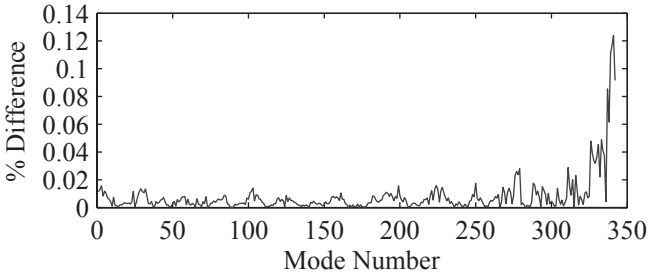

(c) 90% Mass Reduction.

Figure 5.9: PRIME vs. FEM comparison of natural frequencies of a rogue mistuned blisk having missing mass.

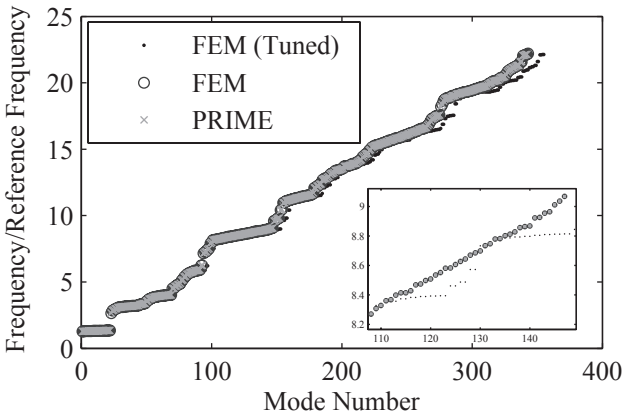

Figure 5.10: Natural frequencies of a rogue mistuned blisk having a sector with 90% missing mass.

mode shape when there is localization in the rogue blade. Finally, it is important to note

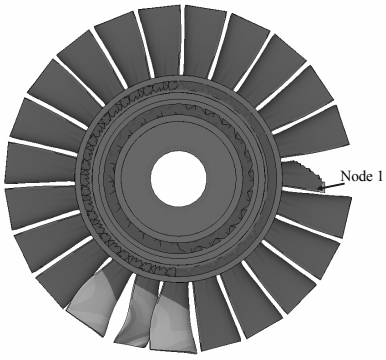

Figure 5.11: Mode shape localized at a blade with no missing mass (Mode index 66 in Fig. 5.9(b)).

that these effects of large mistuning are not well captured using CMM frequency mistuning modeling. Figure 5.13 shows that the frequencies as predicted by CMM have much lower accuracy than those predicted using PRIME. Furthermore, as expected, the mode shapes (arbitrarily normalized) predicted by CMM cannot capture the localized mode shape.

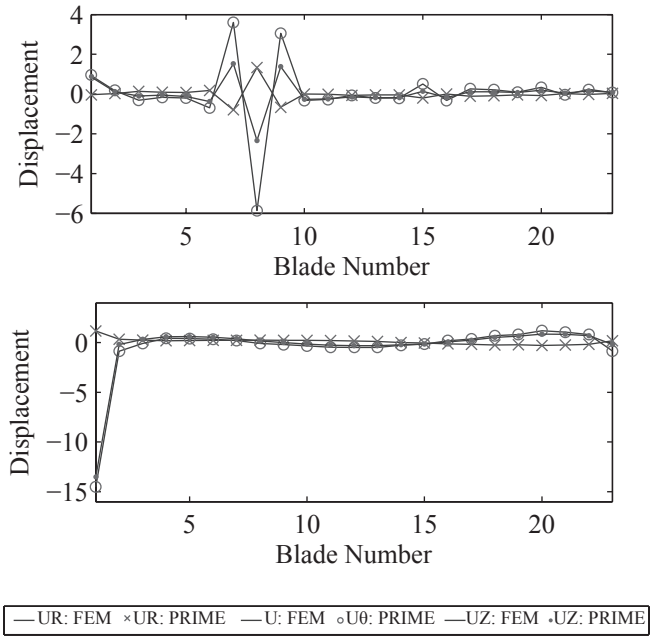

Figure 5.12: PRIME vs. FEM comparison of localized mode shapes (Mode index 66 and 70 in Fig. 5.9(b)). Localized modes shown in Figs. 5.11 and 5.7, respectively.

5.4 Conclusions

There is an important need to accurately and efficiently model large mistuning (such as large geometric changes or missing material) in the presence of small mistuning for the analysis of damaged blisks or for the design of new blisks. A novel reduced order modeling methodology (PRIME) was presented and demonstrated to address this need. The results highlight that:

- A basis comprised of modes computed from cyclic symmetry analysis of tuned and rogue sectors can be assembled to represent the corresponding DOFs in the physical space. The basis can be expanded (allowing additional DOFs in the modal space) to avoid over constraining the system.

- Conditioning of the basis is essential to unlocking the model while keeping the system matrices well conditioned.

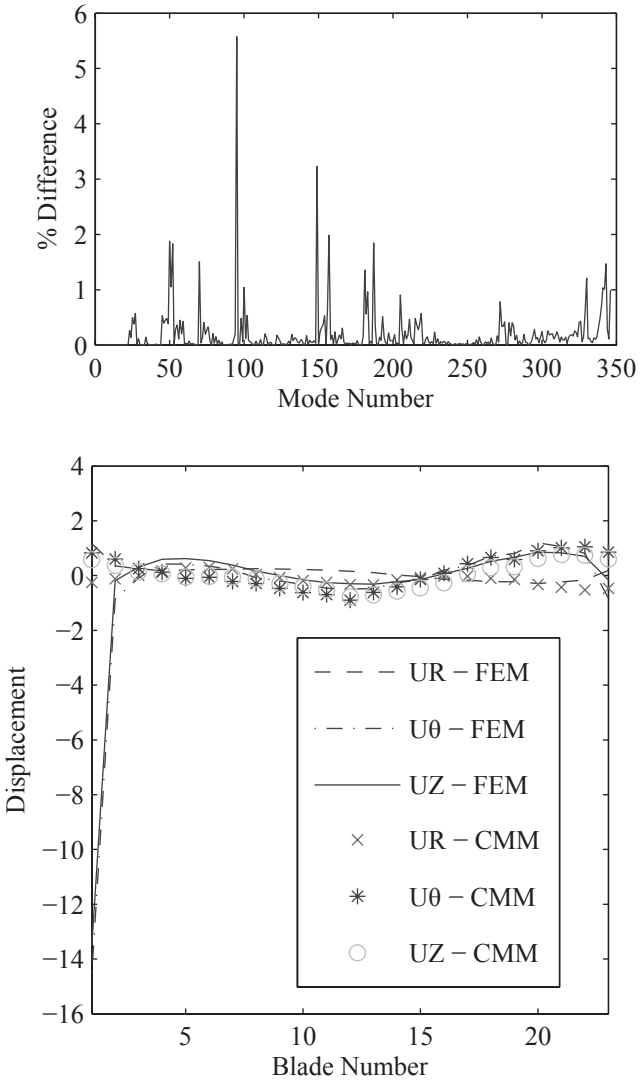

Figure 5.13: CMM vs. FEM comparison of natural frequencies and localized mode shape (Mode index 70 in Fig. 5.9(b))

.

- The PRIME basis can be formulated such that the ROM can be generated using only sector level calculations, generalizing the type of allowable finite element meshes and enabling the rapid generation of ROMs.

- Both large mistuning (up to 100% of a blade missing) and small mistuning can be accurately modeled using PRIME.

- The natural frequencies and mode shapes of blisks with complex geometry suffering from both large damage and small mistuning can be captured accurately using PRIME.

CHAPTER VI

Conclusions and Future Work

6.1 Contributions

The work in this dissertation presents several algorithms and methodologies for predicting the dynamic system response and identifying parameters of turbomachinery. The original contributions of this work can be summarized as follows:

- In Chapter II the concept of IROM was introduced. It was demonstrated that using a standard DROM results in inaccurate mistuning identification. To address this, the novel concept of the IROM was employed. A new metric called the selection ratio was introduced to systematically categorize modes in a way that minimized negative effects of CMM-ROM approximations, while maximizing the sensitivity to mistuning. The effect of using a limited number of experimental measurement points per blade was studied. It was noted that a rank deficiency in the modal matrix would cause an inaccuracy in the physical to modal transformation needed for CMM mistuning identification. It was determined that using too few points can result in a rank deficiency of the modal matrix. This is especially true if multiple modes having the same nodal diameter content are included in the basis. Therefore, it is necessary to either add additional measurement points or avoid using modes that could result in ill-conditioning of the modal matrix. In addition, a novel technique is introduced

to automatically determine a suitable IROM size to accurately predict mistuning values. This idea is based on using surrogate data generated using the DROM to then interrogate the IROM. First, the mistuning used in the DROM was randomly generated. Then the DROM was used to generated surrogate data in the modal space, upon which noise was added. This surrogate data was plugged into each IROM size available. The mistuning parameters were identified and then compared with the original random mistuning used in the DROM. Using this technique, it was demonstrated that it was possible to automatically identify mistuning with high accuracy.

- In Chapter III the CMM-based mistuning identification procedure was extended to higher frequency ranges. It was noted that mistuning identification in higher frequency ranges is affected by two key factors. The first was that the motion of the blisk has increasingly complex topologies and blade-disk interactions. The second was that there are no longer regions of high modal density where modes will be highly sensitive to mistuning. This issue was addressed by increasing the importance on measurement point selection. Measurement points were selected using the EIDV procedure for each possible IROM size. These measurement points were shown to be more sensitive to mistuning and better able to represent the mode shapes used in the reduced-order model for predictions. Then each IROM was evaluated using the surrogate data process. Ultimately, it was demonstrated that it is possible to identify unique mistuning patterns for multiple cantilevered blade mode families in higher frequency ranges. The resulting mistuning patterns could then be used with a novel approach to identify physical parameter variations in different portions of the blades. A technique was suggested to address possible conditioning issues with this approach. Finally, it was demonstrated that changes in the modulus of elasticity in

different geometric locations of the blade could be identified using only mistuning patterns.

- In Chapter IV a new approach to modeling of blisks having both large and small mistuning was introduced. First, it was demonstrated that a basis of tuned modes was insufficient to serve as a basis for a system having large mistuning. Then it was demonstrated that a basis of nominally rogue modes was sufficient to serve as a basis for a system with rogue modes. The basis of rogue system modes was first computed using CMS with each sector as a component. The modes are computed in the reduced CMS space and then expanded to the full order system. These modes accurately predicted the response of the mistuned system. In order, to reduce the number of DOFs in the CMS ROM space and while still allowing for rapid swapping of rogue sectors, a secondary substructuring was suggested. This secondary analysis performed CMS on both 2-sector and 4-sector components, while leaving rogue sectors in the original reduced state. This would allow for rogue sectors to be changed so that other rogue systems could be studied. The secondary reduction showed an improvement in computational time at the reduced modal step. However, clear drawbacks to this approach were demonstrated. First, computational time for the reduction process alone was prohibitive for large systems. Also, for extremely large systems, memory consumption and files generated by the ANSYS® were too great and the analysis would not complete. For completeness, an extended CMM approach was included in this methodology to model small mistuning. The rogue portion of the mistuned system was projected onto rogue cantilevered blade modes. This resulted in excellent accuracy in the eigenvalues and forced response of the system.

- In Chapter V introduced a novel ROM based on the pristine, rogue, interface modal expansion (PRIME). The new ROM was based on computing the basis strictly from sector level quantities to avoid computation concerns related to generating ROMs for large mistuning. To do this, modes computed from cyclic symmetry of the pristine, rogue and interface portions were used as a basis for the pristine, rogue and interface DOFs. All three entities were given separate DOFs in the modal domain to add flexibility to the model. A technique based on expanded sector calculations was introduced to allow for computing the ROM while keeping only a single sector's worth of information in the memory at a time. Then it was demonstrated that the extended CMM procedure introduced in Chapter IV could be applied to this ROM. Finally, a further reduction and conditioning of the basis was introduced. The results show an extremely accurate prediction of the eigenvalues and mode shapes of a system having moderate and severe damage.

6.2 Future Research

The following are topics of future research which have been generated in the process of doing the work presented in this dissertation.

- **Improved Measurement Point Selection**

  It is clear from the work done in Chapters II and III that measurement point selection is of critical importance to mistuning identification. First, it is important because it has a dramatic effect on the accuracy of the mistuning predicted. Also, it is important because experimentally measuring additional points can be costly in terms of time. The current measurement point selection is based on EIDV, which essentially chooses points that make the mode shapes most linearly independent. However, sometimes this algorithm will pick adjacent points. This demonstrates a weakness

in this method. Future work would include an exploration of other measurement point selection techniques, especially those that more directly choose points that are sensitive to mistuning.

- **Mistuning Identification Using Engine Data**

  Currently, mistuning is identified by fixing a blisk in a stationary fashion and applying some excitation. However, this requires the removal of a blisk from the operating environment and extra effort to create a rig that can accommodate the experimental procedure. However, engine data is often readily available to manufacturers of turbomachinery. Future work could include attempting to build a mistuning identification procedure around the use of engine data. This could enable more rapid mistuning identification and also evaluation of mistuning of blisks in operation. It would then be possible to determine possible causes of changing dynamics of the system over the course of the life of the blisk.

- **Multiple Rogue Sector Large Mistuning**

  The PRIME methodology has currently only been tested for a single rogue sector. In practice, large mistuning usually occurs in multiple sectors either because of damage or manufacturing. Therefore, it is necessary to extend the PRIME methodology to allow for multiple rogue blades. This would enable a more realistic model of the dynamics of blisks having both large and small mistuning.

APPENDIX

APPENDIX A

Extended Formulation of CMM-Based ROM for Large Mistuning

Consider the equation of motion of a damped, forced, rogue blisk expressed as

$$\mathbf{M}^r\ddot{\mathbf{X}} + \mathbf{K}^r\mathbf{X} = \mathbf{F} + \mathbf{F}_{sd}, \tag{A.1}$$

where $\mathbf{F}_{sd}$ denotes the force caused by structural damping. It is assumed that there is mistuning in this system and that the system can be split into a tuned component and a mistuned component as per the CMM approach by Lim et al. [23], with the exception that the tuned system is now the rogue system. One obtains

rogue:

$$\mathbf{M}^r\ddot{\mathbf{X}}^r + \mathbf{K}^r\mathbf{X}^r = \mathbf{F}^r + \mathbf{F}^r_{sd}, \tag{A.2}$$

mistuned (Small):

$$\mathbf{M}^\delta\ddot{\mathbf{X}}^\delta + \mathbf{K}^\delta\mathbf{X}^\delta = \mathbf{0}. \tag{A.3}$$

For the nominal rogue system let

$$\mathbf{X}^r = \begin{bmatrix} \mathbf{X}^r_\Omega \\ \mathbf{X}^r_\Gamma \end{bmatrix} = \begin{bmatrix} \mathbf{\Phi}^r_\Omega\ \mathbf{\Psi}^r_\Omega \\ \mathbf{\Phi}^r_\Gamma\ \mathbf{\Psi}^r_\Gamma \end{bmatrix} \begin{bmatrix} \mathbf{P}^r_\Phi \\ \mathbf{P}^r_\Psi \end{bmatrix} = \begin{bmatrix} \mathbf{\Phi}^r_\Omega\ \mathbf{\Psi}^r_\Omega \\ \mathbf{\Phi}^r_\Gamma\ \mathbf{\Psi}^r_\Gamma \end{bmatrix} \mathbf{P}^r, \tag{A.4}$$

where Ω denotes the disk portion of the nominal rogue system, and Γ represents the blade portion of the nominal rogue system.

Substituting Eq. A.4 into Eq. A.2 and premultiplying yields

$$\begin{bmatrix} \boldsymbol{\Phi}_\Omega^{r\,\mathrm{T}} & \boldsymbol{\Phi}_\Gamma^{r\,\mathrm{T}} \\ \boldsymbol{\Psi}_\Omega^{r\,\mathrm{T}} & \boldsymbol{\Psi}_\Gamma^{r\,\mathrm{T}} \end{bmatrix} \begin{bmatrix} \mathbf{M}_{\Omega\Omega}^r & \mathbf{M}_{\Omega\Gamma}^r \\ \mathbf{M}_{\Gamma\Omega}^r & \mathbf{M}_{\Gamma\Gamma}^r \end{bmatrix} \begin{bmatrix} \boldsymbol{\Phi}_\Omega^r & \boldsymbol{\Psi}_\Omega^r \\ \boldsymbol{\Phi}_\Gamma^r & \boldsymbol{\Psi}_\Gamma^r \end{bmatrix} \begin{bmatrix} \mathbf{P}_\Phi^r \\ \mathbf{P}_\Psi^r \end{bmatrix} + \begin{bmatrix} \boldsymbol{\Phi}_\Omega^{r\,\mathrm{T}} & \boldsymbol{\Phi}_\Gamma^{r\,\mathrm{T}} \\ \boldsymbol{\Psi}_\Omega^{r\,\mathrm{T}} & \boldsymbol{\Psi}_\Gamma^{r\,\mathrm{T}} \end{bmatrix} \begin{bmatrix} \mathbf{K}_{\Omega\Omega}^r & \mathbf{K}_{\Omega\Gamma}^r \\ \mathbf{K}_{\Gamma\Omega}^r & \mathbf{K}_{\Gamma\Gamma}^r \end{bmatrix} \begin{bmatrix} \boldsymbol{\Phi}_\Omega^r & \boldsymbol{\Psi}_\Omega^r \\ \boldsymbol{\Phi}_\Gamma^r & \boldsymbol{\Psi}_\Gamma^r \end{bmatrix} \begin{bmatrix} \mathbf{P}_\Phi^r \\ \mathbf{P}_\Psi^r \end{bmatrix} = \begin{bmatrix} \boldsymbol{\Phi}_\Omega^{r\,\mathrm{T}} & \boldsymbol{\Phi}_\Gamma^{r\,\mathrm{T}} \\ \boldsymbol{\Psi}_\Omega^{r\,\mathrm{T}} & \boldsymbol{\Psi}_\Gamma^{r\,\mathrm{T}} \end{bmatrix} \mathbf{F}^r + \begin{bmatrix} \boldsymbol{\Phi}_\Omega^{r\,\mathrm{T}} & \boldsymbol{\Phi}_\Gamma^{r\,\mathrm{T}} \\ \boldsymbol{\Psi}_\Omega^{r\,\mathrm{T}} & \boldsymbol{\Psi}_\Gamma^{r\,\mathrm{T}} \end{bmatrix} \mathbf{F}_{sd}^r. \quad \text{(A.5)}$$

Equation A.5 can be simplified as

$$\begin{bmatrix} \boldsymbol{\Phi}^{r\,\mathrm{T}}\mathbf{M}^r\boldsymbol{\Phi}^r & \boldsymbol{\Phi}^{r\,\mathrm{T}}\mathbf{M}^r\boldsymbol{\Psi}^r \\ \boldsymbol{\Psi}^{r\,\mathrm{T}}\mathbf{M}^r\boldsymbol{\Phi}^r & \boldsymbol{\Psi}^{r\,\mathrm{T}}\mathbf{M}^r\boldsymbol{\Psi}^r \end{bmatrix} \begin{bmatrix} \mathbf{P}_\Phi^r \\ \mathbf{P}_\Psi^r \end{bmatrix} + \begin{bmatrix} \boldsymbol{\Phi}^{r\,\mathrm{T}}\mathbf{K}^r\boldsymbol{\Phi}^r & \boldsymbol{\Phi}^{r\,\mathrm{T}}\mathbf{K}^r\boldsymbol{\Psi}^r \\ \boldsymbol{\Psi}^{r\,\mathrm{T}}\mathbf{K}^r\boldsymbol{\Phi}^r & \boldsymbol{\Psi}^{r\,\mathrm{T}}\mathbf{K}^r\boldsymbol{\Psi}^r \end{bmatrix} \begin{bmatrix} \mathbf{P}_\Phi^r \\ \mathbf{P}_\Psi^r \end{bmatrix} \quad \text{(A.6)}$$

$$= \begin{bmatrix} \boldsymbol{\Phi}_\Omega^{r\,\mathrm{T}} & \boldsymbol{\Phi}_\Gamma^{r\,\mathrm{T}} \\ \boldsymbol{\Psi}_\Omega^{r\,\mathrm{T}} & \boldsymbol{\Psi}_\Gamma^{r\,\mathrm{T}} \end{bmatrix} \mathbf{F}^r + \begin{bmatrix} \boldsymbol{\Phi}_\Omega^{r\,\mathrm{T}} & \boldsymbol{\Phi}_\Gamma^{r\,\mathrm{T}} \\ \boldsymbol{\Psi}_\Omega^{r\,\mathrm{T}} & \boldsymbol{\Psi}_\Gamma^{r\,\mathrm{T}} \end{bmatrix} \mathbf{F}_{sd}^r, \quad \text{(A.7)}$$

or

$$\begin{bmatrix} \mathbf{I} & \boldsymbol{\Phi}^{r\,\mathrm{T}}\mathbf{M}^r\boldsymbol{\Psi}^r \\ \boldsymbol{\Psi}^{r\,\mathrm{T}}\mathbf{M}^r\boldsymbol{\Phi}^r & \boldsymbol{\Psi}^{r\,\mathrm{T}}\mathbf{M}^r\boldsymbol{\Psi}^r \end{bmatrix} \begin{bmatrix} \mathbf{P}_\Phi^r \\ \mathbf{P}_\Psi^r \end{bmatrix} + \begin{bmatrix} \boldsymbol{\Lambda}^r & \boldsymbol{\Phi}^{r\,\mathrm{T}}\mathbf{K}^r\boldsymbol{\Psi}^r \\ \boldsymbol{\Psi}^{r\,\mathrm{T}}\mathbf{K}^r\boldsymbol{\Phi}^r & \boldsymbol{\Psi}^r \end{bmatrix} \begin{bmatrix} \mathbf{P}_\Phi^r \\ \mathbf{P}_\Psi^r \end{bmatrix} \quad \text{(A.8)}$$

$$= \begin{bmatrix} \boldsymbol{\Phi}_\Omega^{r\,\mathrm{T}} & \boldsymbol{\Phi}_\Gamma^{r\,\mathrm{T}} \\ \boldsymbol{\Psi}_\Omega^{r\,\mathrm{T}} & \boldsymbol{\Psi}_\Gamma^{r\,\mathrm{T}} \end{bmatrix} \mathbf{F}^r + \begin{bmatrix} \boldsymbol{\Phi}_\Omega^{r\,\mathrm{T}} & \boldsymbol{\Phi}_\Gamma^{r\,\mathrm{T}} \\ \boldsymbol{\Psi}_\Omega^{r\,\mathrm{T}} & \boldsymbol{\Psi}_\Gamma^{r\,\mathrm{T}} \end{bmatrix} \mathbf{F}_{sd}^r. \quad \text{(A.9)}$$

Next, consider the mistuned model, which contains only DOF from the blade, that is

$$\mathbf{X}^\delta = \begin{bmatrix} \mathbf{X}_\Omega^\delta \\ \mathbf{X}_\Gamma^\delta \end{bmatrix} = \begin{bmatrix} \boldsymbol{\Phi}_\Omega^\delta & \boldsymbol{\Psi}_\Omega^\delta \\ \boldsymbol{\Phi}_\Gamma^\delta & \boldsymbol{\Psi}_\Gamma^\delta \end{bmatrix} \begin{bmatrix} \mathbf{P}_\Phi^\delta \\ \mathbf{P}_\Psi^\delta \end{bmatrix}. \quad \text{(A.10)}$$

In this case, all DOF are part of the boundary DOF. Therefore the interior DOF/normal modes do not exist for the mistuned model, so that

$$\mathbf{X}^\delta = \mathbf{X}_\Gamma^\delta = \boldsymbol{\Psi}_\Gamma^\delta \mathbf{P}_\Psi^\delta = \mathbf{I}\mathbf{P}_\Psi^\delta. \quad \text{(A.11)}$$

Hence, the equation of motion for a mistuned component can be expressed as

$$\mathbf{M}^{\delta}\mathbf{P}_{\Psi}^{\delta} + \mathbf{K}^{\delta}\mathbf{P}_{\Psi}^{\delta} = \mathbf{0}. \tag{A.12}$$

Next, one may to define a coordinate vector P' as

$$\mathbf{P}' = \begin{bmatrix} \mathbf{P}_{\Phi}^{r} \\ \mathbf{P}_{\Psi}^{r} \\ \mathbf{P}_{\Psi}^{\delta} \end{bmatrix}, \tag{A.13}$$

and transformed mass and stiffness matrices as

$$\boldsymbol{\mu}^{r} = \begin{bmatrix} \mathbf{I} & \boldsymbol{\Phi}^{r\mathrm{T}}\mathbf{M}^{r}\boldsymbol{\Psi}^{r} \\ \boldsymbol{\Psi}^{r\mathrm{T}}\mathbf{M}^{r}\boldsymbol{\Phi}^{r} & \boldsymbol{\Psi}^{r\mathrm{T}}\mathbf{M}^{r}\boldsymbol{\Psi}^{r} \end{bmatrix}, \quad \boldsymbol{\kappa}^{r} = \begin{bmatrix} \boldsymbol{\Lambda}^{r} & \boldsymbol{\Phi}^{r\mathrm{T}}\mathbf{K}^{r}\boldsymbol{\Psi}^{r} \\ \boldsymbol{\Psi}^{r\mathrm{T}}\mathbf{K}^{r}\boldsymbol{\Phi}^{r} & \boldsymbol{\Psi}^{r} \end{bmatrix}, \tag{A.14}$$

$$\boldsymbol{\mu}^{\delta} = \mathbf{M}^{\delta}, \qquad \boldsymbol{\kappa}^{\delta} = \mathbf{K}^{\delta}, \tag{A.15}$$

$$\boldsymbol{\mu} = \begin{bmatrix} \boldsymbol{\mu}^{r} & \mathbf{0} \\ \mathbf{0} & \boldsymbol{\mu}^{\delta} \end{bmatrix}, \qquad \boldsymbol{\kappa} = \begin{bmatrix} \boldsymbol{\kappa}^{r} & \mathbf{0} \\ \mathbf{0} & \boldsymbol{\kappa}^{\delta} \end{bmatrix}. \tag{A.16}$$

The constraint equation which makes the dependent coordinates compatible is

$$\mathbf{X}_{\Gamma}^{r} = \mathbf{X}_{\Gamma}^{\delta}, \tag{A.17}$$

and can be written as

$$\boldsymbol{\Phi}_{\Gamma}^{r}\mathbf{P}_{\Phi}^{r} + \boldsymbol{\Psi}_{\Gamma}^{r}\mathbf{P}_{\Psi}^{r} - \mathbf{P}_{\Psi}^{\delta} = \mathbf{0}, \tag{A.18}$$

or

$$\begin{bmatrix} \boldsymbol{\Phi}_{\Gamma}^{r} & \boldsymbol{\Psi}_{\Gamma}^{r} & \mathbf{I} \end{bmatrix} \begin{bmatrix} \mathbf{P}_{\Phi}^{r} \\ \mathbf{P}_{\Psi}^{r} \\ \mathbf{P}_{\Psi}^{\delta} \end{bmatrix} = \mathbf{0}. \tag{A.19}$$

The components will be synthesized into the system using Lagrange's equation with the constraint applied using Langrange multipliers. The Lagrangian is

$$L = T - V + \boldsymbol{\lambda}\mathbf{C}\mathbf{p}' = \frac{1}{2}\left(\dot{\mathbf{P}}'^{\mathrm{T}}\boldsymbol{\mu}\dot{\mathbf{P}}' - \mathbf{P}'^{\mathrm{T}}\boldsymbol{\kappa}\mathbf{P}'\right) + \boldsymbol{\sigma}^{\mathrm{T}}\begin{bmatrix} \boldsymbol{\Phi}_{\Gamma}^{r} & \boldsymbol{\Psi}_{\Gamma}^{r} & -\mathbf{I} \end{bmatrix}\mathbf{P}'. \quad \text{(A.20)}$$

Lagrange's equation becomes

$$\frac{d}{dt}\left(\frac{\partial L}{\partial \dot{\xi}_r}\right) - \frac{\partial L}{\partial \xi_r} = Q_r, \quad \text{(A.21)}$$

which yields

$$\boldsymbol{\mu}\ddot{\mathbf{P}}' + \boldsymbol{\kappa}\mathbf{P}' = \begin{bmatrix} \boldsymbol{\Phi}_{\Omega}^{r\,\mathrm{T}} & \boldsymbol{\Phi}_{\Gamma}^{r\,\mathrm{T}} & \mathbf{0} \\ \boldsymbol{\Psi}_{\Omega}^{r\,\mathrm{T}} & \boldsymbol{\Psi}_{\Gamma}^{r\,\mathrm{T}} & \mathbf{0} \\ \mathbf{0} & \mathbf{0} & \mathbf{0} \end{bmatrix}\begin{bmatrix} \mathbf{F}^{r} \\ \mathbf{0} \end{bmatrix} + \begin{bmatrix} \boldsymbol{\Phi}_{\Omega}^{r\,\mathrm{T}} & \boldsymbol{\Phi}_{\Gamma}^{r\,\mathrm{T}} & \mathbf{0} \\ \boldsymbol{\Psi}_{\Omega}^{r\,\mathrm{T}} & \boldsymbol{\Psi}_{\Gamma}^{r\,\mathrm{T}} & \mathbf{0} \\ \mathbf{0} & \mathbf{0} & \mathbf{0} \end{bmatrix}\begin{bmatrix} \mathbf{F}_{sd}^{r} \\ \mathbf{0} \end{bmatrix} + \begin{bmatrix} \boldsymbol{\Phi}_{\Gamma}^{r} \\ \boldsymbol{\Psi}_{\Gamma}^{r} \\ -\mathbf{I} \end{bmatrix}\boldsymbol{\sigma}, \quad \text{(A.22)}$$

$$\boldsymbol{\Phi}_{\Gamma}^{r}\mathbf{P}_{\Phi}^{r} + \boldsymbol{\Psi}_{\Gamma}^{r}\mathbf{P}_{\Psi}^{r} - \mathbf{P}_{\Psi}^{\delta} = \mathbf{0}. \quad \text{(A.23)}$$

Next, the coordinate transformation is applied to eliminate dependent coordinates. One obtains

$$\begin{bmatrix} \mathbf{P}_{\Phi}^{r} \\ \mathbf{P}_{\Psi}^{r} \\ \mathbf{P}_{\Psi}^{\delta} \end{bmatrix} = \begin{bmatrix} \mathbf{I} & \mathbf{0} \\ \mathbf{0} & \mathbf{I} \\ \boldsymbol{\Phi}_{\Gamma}^{r} & \boldsymbol{\Psi}_{\Gamma}^{r} \end{bmatrix}\begin{bmatrix} \mathbf{P}_{\Phi}^{r} \\ \mathbf{P}_{\Psi}^{r} \end{bmatrix}. \quad \text{(A.24)}$$

Plugging Eq. A.24 into Eq. A.22 and premultiplying by the transpose of the transformation matrix results in

$$\begin{bmatrix} \mathbf{I} & \mathbf{0} & {\boldsymbol{\Phi}_\Gamma^r}^{\mathrm{T}} \\ \mathbf{0} & \mathbf{I} & {\boldsymbol{\Psi}_\Gamma^r}^{\mathrm{T}} \end{bmatrix} \begin{bmatrix} \mathbf{I} & {\boldsymbol{\Phi}^r}^{\mathrm{T}}\mathbf{M}^r\boldsymbol{\Psi}^r & \mathbf{0} \\ {\boldsymbol{\Psi}^r}^{\mathrm{T}}\mathbf{M}^r\boldsymbol{\Phi}^r & {\boldsymbol{\Psi}^r}^{\mathrm{T}}\mathbf{M}^r\boldsymbol{\Psi}^r & \mathbf{0} \\ \mathbf{0} & \mathbf{0} & \mathbf{M}^\delta \end{bmatrix} \begin{bmatrix} \mathbf{I} & \mathbf{0} \\ \mathbf{0} & \mathbf{I} \\ \boldsymbol{\Phi}_\Gamma^r & \boldsymbol{\Psi}_\Gamma^r \end{bmatrix} \begin{bmatrix} \ddot{\mathbf{P}}_\Phi^r \\ \ddot{\mathbf{P}}_\Psi^r \end{bmatrix} +$$
$$+ \begin{bmatrix} \mathbf{I} & \mathbf{0} & {\boldsymbol{\Phi}_\Gamma^r}^{\mathrm{T}} \\ \mathbf{0} & \mathbf{I} & {\boldsymbol{\Psi}_\Gamma^r}^{\mathrm{T}} \end{bmatrix} \begin{bmatrix} \boldsymbol{\Lambda}^r & {\boldsymbol{\Phi}^r}^{\mathrm{T}}\mathbf{K}^r\boldsymbol{\Psi}^r & \mathbf{0} \\ {\boldsymbol{\Psi}^r}^{\mathrm{T}}\mathbf{K}^r\boldsymbol{\Phi}^r & \boldsymbol{\Psi}^r & \mathbf{0} \\ \mathbf{0} & \mathbf{0} & \mathbf{K}^\delta \end{bmatrix} \begin{bmatrix} \mathbf{I} & \mathbf{0} \\ \mathbf{0} & \mathbf{I} \\ \boldsymbol{\Phi}_\Gamma^r & \boldsymbol{\Psi}_\Gamma^r \end{bmatrix} \begin{bmatrix} \mathbf{P}_\Phi^r \\ \mathbf{P}_\Psi^r \end{bmatrix}$$

$$= \begin{bmatrix} \mathbf{I} & \mathbf{0} & {\boldsymbol{\Phi}_\Gamma^r}^{\mathrm{T}} \\ \mathbf{0} & \mathbf{I} & {\boldsymbol{\Psi}_\Gamma^r}^{\mathrm{T}} \end{bmatrix} \begin{bmatrix} {\boldsymbol{\Phi}_\Omega^r}^{\mathrm{T}} & {\boldsymbol{\Phi}_\Gamma^r}^{\mathrm{T}} & \mathbf{0} \\ {\boldsymbol{\Psi}_\Omega^r}^{\mathrm{T}} & {\boldsymbol{\Psi}_\Gamma^r}^{\mathrm{T}} & \mathbf{0} \\ \mathbf{0} & \mathbf{0} & \mathbf{0} \end{bmatrix} \begin{bmatrix} \mathbf{F}^r \\ \mathbf{0} \end{bmatrix} +$$
$$+ \begin{bmatrix} \mathbf{I} & \mathbf{0} & {\boldsymbol{\Phi}_\Gamma^r}^{\mathrm{T}} \\ \mathbf{0} & \mathbf{I} & {\boldsymbol{\Psi}_\Gamma^r}^{\mathrm{T}} \end{bmatrix} \begin{bmatrix} {\boldsymbol{\Phi}_\Omega^r}^{\mathrm{T}} & {\boldsymbol{\Phi}_\Gamma^r}^{\mathrm{T}} & \mathbf{0} \\ {\boldsymbol{\Psi}_\Omega^r}^{\mathrm{T}} & {\boldsymbol{\Psi}_\Gamma^r}^{\mathrm{T}} & \mathbf{0} \\ \mathbf{0} & \mathbf{0} & \mathbf{0} \end{bmatrix} \begin{bmatrix} \mathbf{F}_{sd}^r \\ \mathbf{0} \end{bmatrix} + \begin{bmatrix} \mathbf{I} & \mathbf{0} & {\boldsymbol{\Phi}_\Gamma^r}^{\mathrm{T}} \\ \mathbf{0} & \mathbf{I} & {\boldsymbol{\Psi}_\Gamma^r}^{\mathrm{T}} \end{bmatrix} \begin{bmatrix} \boldsymbol{\Phi}_\Gamma^r \\ \boldsymbol{\Psi}_\Gamma^r \\ -\mathbf{I} \end{bmatrix} \boldsymbol{\sigma}^{\mathrm{T}}$$

Simplifying, one obtains

$$\begin{bmatrix} \mathbf{I} + \boldsymbol{\Phi}_\Gamma^{r\,\mathrm{T}}\mathbf{M}^\delta\boldsymbol{\Phi}_\Gamma^r & {\boldsymbol{\Phi}^r}^{\mathrm{T}}\mathbf{M}^r\boldsymbol{\Psi}^r + \boldsymbol{\Phi}_\Gamma^{r\,\mathrm{T}}\mathbf{M}^\delta\boldsymbol{\Psi}_\Gamma^r \\ {\boldsymbol{\Psi}^r}^{\mathrm{T}}\mathbf{M}^r\boldsymbol{\Phi}^r + \boldsymbol{\Psi}_\Gamma^{r\,\mathrm{T}}\mathbf{M}^\delta\boldsymbol{\Phi}_\Gamma^r & {\boldsymbol{\Psi}^r}^{\mathrm{T}}\mathbf{M}^r\boldsymbol{\Psi}^r + \boldsymbol{\Psi}_\Gamma^{r\,\mathrm{T}}\mathbf{M}^\delta\boldsymbol{\Psi}_\Gamma^r \end{bmatrix} \begin{bmatrix} \ddot{\mathbf{P}}_\Phi^r \\ \ddot{\mathbf{P}}_\Psi^r \end{bmatrix} +$$
$$\begin{bmatrix} \boldsymbol{\Lambda}^r + \boldsymbol{\Phi}_\Gamma^{r\,\mathrm{T}}\mathbf{K}^\delta\boldsymbol{\Phi}_\Gamma^r & {\boldsymbol{\Phi}^r}^{\mathrm{T}}\mathbf{K}^r\boldsymbol{\Psi}^r + \boldsymbol{\Phi}_\Gamma^{r\,\mathrm{T}}\mathbf{K}^\delta\boldsymbol{\Psi}_\Gamma^r \\ {\boldsymbol{\Psi}^r}^{\mathrm{T}}\mathbf{K}^r\boldsymbol{\Phi}^r + \boldsymbol{\Psi}_\Gamma^{r\,\mathrm{T}}\mathbf{K}^\delta\boldsymbol{\Phi}_\Gamma^r & \boldsymbol{\Psi}^r + \boldsymbol{\Psi}_\Gamma^{r\,\mathrm{T}}\mathbf{K}^\delta\boldsymbol{\Psi}_\Gamma^r \end{bmatrix} \begin{bmatrix} \mathbf{P}_\Phi^r \\ \mathbf{P}_\Psi^r \end{bmatrix} \tag{A.27}$$
$$= \begin{bmatrix} {\boldsymbol{\Phi}_\Omega^r}^{\mathrm{T}} & {\boldsymbol{\Phi}_\Gamma^r}^{\mathrm{T}} \\ {\boldsymbol{\Psi}_\Omega^r}^{\mathrm{T}} & {\boldsymbol{\Psi}_\Gamma^r}^{\mathrm{T}} \end{bmatrix} \mathbf{F}^r + \begin{bmatrix} {\boldsymbol{\Phi}_\Omega^r}^{\mathrm{T}} & {\boldsymbol{\Phi}_\Gamma^r}^{\mathrm{T}} \\ {\boldsymbol{\Psi}_\Omega^r}^{\mathrm{T}} & {\boldsymbol{\Psi}_\Gamma^r}^{\mathrm{T}} \end{bmatrix} \mathbf{F}_{sd}^r$$

Next, one may assume harmonic motion to obtain

$$\mathbf{P}^r = \mathbf{p}^r e^{j\omega t}, \tag{A.28}$$

$$\mathbf{F}^r = \mathbf{f}^r e^{j\omega t}, \tag{A.29}$$

$$\begin{aligned} \begin{bmatrix} \boldsymbol{\Phi}_\Omega^{r\,\mathrm{T}} & \boldsymbol{\Phi}_\Gamma^{r\,\mathrm{T}} \\ \boldsymbol{\Psi}_\Omega^{r\,\mathrm{T}} & \boldsymbol{\Psi}_\Gamma^{r\,\mathrm{T}} \end{bmatrix} \mathbf{F}_{sd}^r = \\ -j\gamma \begin{bmatrix} \boldsymbol{\Lambda}^r + \boldsymbol{\Phi}_\Gamma^{r\,\mathrm{T}} \mathbf{K}^\delta \boldsymbol{\Phi}_\Gamma^r & \boldsymbol{\Phi}^{r\,\mathrm{T}} \mathbf{K}^r \boldsymbol{\Psi}^r + \boldsymbol{\Phi}_\Gamma^{r\,\mathrm{T}} \mathbf{K}^\delta \boldsymbol{\Psi}_\Gamma^r \\ \boldsymbol{\Psi}^{r\,\mathrm{T}} \mathbf{K}^r \boldsymbol{\Phi}^r + \boldsymbol{\Psi}_\Gamma^{r\,\mathrm{T}} \mathbf{K}^\delta \boldsymbol{\Phi}_\Gamma^r & \boldsymbol{\Psi}^r + \boldsymbol{\Psi}_\Gamma^{r\,\mathrm{T}} \mathbf{K}^\delta \boldsymbol{\Psi}_\Gamma^r \end{bmatrix} \mathbf{p} e^{j\omega t}, \end{aligned} \tag{A.30}$$

so that

$$\begin{aligned} -\omega^2 \begin{bmatrix} \mathbf{I} + \boldsymbol{\Phi}_\Gamma^{r\,\mathrm{T}} \mathbf{M}^\delta \boldsymbol{\Phi}_\Gamma^r & \boldsymbol{\Phi}^{r\,\mathrm{T}} \mathbf{M}^r \boldsymbol{\Psi}^r + \boldsymbol{\Phi}_\Gamma^{r\,\mathrm{T}} \mathbf{M}^\delta \boldsymbol{\Psi}_\Gamma^r \\ \boldsymbol{\Psi}^{r\,\mathrm{T}} \mathbf{M}^r \boldsymbol{\Phi}^r + \boldsymbol{\Psi}_\Gamma^{r\,\mathrm{T}} \mathbf{M}^\delta \boldsymbol{\Phi}_\Gamma^r & \boldsymbol{\Psi}^{r\,\mathrm{T}} \mathbf{M}^r \boldsymbol{\Psi}^r + \boldsymbol{\Psi}_\Gamma^{r\,\mathrm{T}} \mathbf{M}^\delta \boldsymbol{\Psi}_\Gamma^r \end{bmatrix} \begin{bmatrix} \mathbf{p}_\Phi^r \\ \mathbf{p}_\Psi^r \end{bmatrix} + \\ (1 + j\gamma) \begin{bmatrix} \boldsymbol{\Lambda}^r + \boldsymbol{\Phi_\Gamma}^{r\,\mathrm{T}} \mathbf{K}^\delta \boldsymbol{\Phi}_\Gamma^r & \boldsymbol{\Phi}^{r\,\mathrm{T}} \mathbf{K}^r \boldsymbol{\Psi}^r + \boldsymbol{\Phi}_\Gamma^{r\,\mathrm{T}} \mathbf{K}^\delta \boldsymbol{\Psi}_\Gamma^r \\ \boldsymbol{\Psi}^{r\,\mathrm{T}} \mathbf{K}^r \boldsymbol{\Phi}^r + \boldsymbol{\Psi}_\Gamma^{r\,\mathrm{T}} \mathbf{K}^\delta \boldsymbol{\Phi}_\Gamma^r & \boldsymbol{\Psi}^r + \boldsymbol{\Psi}_\Gamma^{r\,\mathrm{T}} \mathbf{K}^\delta \boldsymbol{\Psi}_\Gamma^r \end{bmatrix} \begin{bmatrix} \mathbf{p}_\Phi^r \\ \mathbf{p}_\Psi^r \end{bmatrix} \\ = \begin{bmatrix} \boldsymbol{\Phi}_\Omega^{r\,\mathrm{T}} & \boldsymbol{\Phi}_\Gamma^{r\,\mathrm{T}} \\ \boldsymbol{\Psi}_\Omega^{r\,\mathrm{T}} & \boldsymbol{\Psi}_\Gamma^{r\,\mathrm{T}} \end{bmatrix} \mathbf{f}^r. \end{aligned} \tag{A.31}$$

Note that mistuned modes in a high modal density region can be represented using tuned modes in the same region [56]. We further this assumption that the system modes of a nominally rogue system with small mistuning can be represented using the rogue modes without small mistuning. This means that all static constraint modes may be ignored as follows

$$-\omega^2 \begin{bmatrix} \mathbf{I} + \boldsymbol{\Phi}_\Gamma^{r\,\mathrm{T}} \mathbf{M}^\delta \boldsymbol{\Phi}_\Gamma^r \end{bmatrix} \mathbf{p}_\Phi^r + (1 + j\gamma) \begin{bmatrix} \boldsymbol{\Lambda}^r + \boldsymbol{\Phi_\Gamma}^{r\,\mathrm{T}} \mathbf{K}^\delta \boldsymbol{\Phi}_\Gamma^r \end{bmatrix} \mathbf{p}_\Phi^r = \boldsymbol{\Phi}^{r\,\mathrm{T}} \mathbf{f}^r. \tag{A.32}$$

It is desirable to represent the blade portion of the system normal modes with a set of component modes of a tuned blade or rogue blade in this extension of the method. For

convenience, Eq. A.32 can be expressed as

$$\begin{gathered} -\omega^2 \left[\mathbf{I} + {\boldsymbol{\Phi}_\Gamma^r}^{\mathrm{T}} \begin{bmatrix} \mathbf{M}_{ii}^\delta & \mathbf{M}_{ib}^\delta \\ \mathbf{M}_{bi}^\delta & \mathbf{M}_{bb}^\delta \end{bmatrix} \boldsymbol{\Phi}_\Gamma^r \right] \mathbf{p}_\Phi^r + \\ (1+j\gamma) \left[\boldsymbol{\Lambda}^r + {\boldsymbol{\Phi}_\Gamma^r}^{\mathrm{T}} \begin{bmatrix} \mathbf{K}_{ii}^\delta & \mathbf{K}_{ib}^\delta \\ \mathbf{K}_{bi}^\delta & \mathbf{K}_{bb}^\delta \end{bmatrix} \boldsymbol{\Phi}_\Gamma^r \right] \mathbf{p}_\Phi^r = {\boldsymbol{\Phi}^r}^{\mathrm{T}} \mathbf{f}^r. \end{gathered} \tag{A.33}$$

Lim et al. [23] minimizes the contribution of the constraint modes and found the following relationship between the blade portion of the system modes and the component modes of the cantilevered blade modes

$$\boldsymbol{\Phi}_\Gamma^r = \begin{cases} \left(\mathbf{I} \otimes \begin{bmatrix} \boldsymbol{\Phi}^b & \boldsymbol{\Psi}^{b,m} \\ \mathbf{0} & \mathbf{I} \end{bmatrix} \right) \begin{bmatrix} \mathbf{q}_\Phi^m \\ \mathbf{q}_\Psi^m \end{bmatrix} \\ \text{or} \\ \left(\mathbf{I} \otimes \begin{bmatrix} \boldsymbol{\Phi}^b & \boldsymbol{\Psi}^{b,k} \\ \mathbf{0} & \mathbf{I} \end{bmatrix} \right) \begin{bmatrix} \mathbf{q}_\Phi^k \\ \mathbf{q}_\Psi^k \end{bmatrix} \end{cases}, \tag{A.34}$$

where b denotes cantilevered blade. Substituting Eq. A.34 into Eq. A.34, yields

$$\begin{gathered} -\omega^2 \left\{ \mathbf{I} + \begin{bmatrix} \mathbf{q}_\Phi^m \\ \mathbf{q}_\Psi^m \end{bmatrix}^{\mathrm{T}} \left(\mathbf{I} \otimes \begin{bmatrix} {\boldsymbol{\Phi}^b}^{\mathrm{T}} & \mathbf{0} \\ {\boldsymbol{\Psi}^{b,m}}^{\mathrm{T}} & \mathbf{I} \end{bmatrix} \right) \begin{bmatrix} \mathbf{M}_{ii}^\delta & \mathbf{M}_{ib}^\delta \\ \mathbf{M}_{bi}^\delta & \mathbf{M}_{bb}^\delta \end{bmatrix} \left(\mathbf{I} \otimes \begin{bmatrix} \boldsymbol{\Phi}^b & \boldsymbol{\Psi}^{b,m} \\ \mathbf{0} & \mathbf{I} \end{bmatrix} \right) \begin{bmatrix} \mathbf{q}_\Phi^m \\ \mathbf{q}_\Psi^m \end{bmatrix} \right\} \mathbf{p}_\Phi^r + \\ (1+j\gamma) \left\{ \boldsymbol{\Lambda}^r + \begin{bmatrix} \mathbf{q}_\Phi^k \\ \mathbf{q}_\Psi^k \end{bmatrix}^{\mathrm{T}} \left(\mathbf{I} \otimes \begin{bmatrix} {\boldsymbol{\Phi}_o^b}^{\mathrm{T}} & \mathbf{0} \\ {\boldsymbol{\Psi}^{b,k}}^{\mathrm{T}} & \mathbf{I} \end{bmatrix} \right) \begin{bmatrix} \mathbf{K}_{ii}^\delta & \mathbf{K}_{ib}^\delta \\ \mathbf{K}_{bi}^\delta & \mathbf{K}_{bb}^\delta \end{bmatrix} \left(\mathbf{I} \otimes \begin{bmatrix} \boldsymbol{\Phi}^b & \boldsymbol{\Psi}^{b,k} \\ \mathbf{0} & \mathbf{I} \end{bmatrix} \right) \begin{bmatrix} \mathbf{q}_\Phi^k \\ \mathbf{q}_\Psi^k \end{bmatrix} \right\} \mathbf{p}_\Phi^r \\ = {\boldsymbol{\Phi}^r}^{\mathrm{T}} \mathbf{f}^r, \end{gathered} \tag{A.35}$$

which becomes

$$-\omega^2 \left\{ \mathbf{I} + \sum_{n=1}^{N} \begin{bmatrix} {\mathbf{q}^m_{\Phi,n}}^{\mathrm{T}} & {\mathbf{q}^m_{\Psi,n}}^{\mathrm{T}} \end{bmatrix} \begin{bmatrix} {\boldsymbol{\Phi}^b}^{\mathrm{T}} & \mathbf{0} \\ {\boldsymbol{\Psi}^{b,m}}^{\mathrm{T}} & \mathbf{I} \end{bmatrix} \begin{bmatrix} \mathbf{M}^\delta_{ii,n} & \mathbf{M}^\delta_{ib,n} \\ \mathbf{M}^\delta_{bi,n} & \mathbf{M}^\delta_{bb,n} \end{bmatrix} \begin{bmatrix} \boldsymbol{\Phi}^b & \boldsymbol{\Psi}^{b,m} \\ \mathbf{0} & \mathbf{I} \end{bmatrix} \begin{bmatrix} \mathbf{q}^m_{\Phi,n} \\ \mathbf{q}^m_{\Psi,n} \end{bmatrix} \right\} \mathbf{p}^r_\Phi + \cdots$$

$$+ (1 + j\gamma) \left\{ \boldsymbol{\Lambda}^r + \sum_{n=1}^{N} \begin{bmatrix} {\mathbf{q}^k_{\Phi,n}}^{\mathrm{T}} & {\mathbf{q}^k_{\Psi,n}}^{\mathrm{T}} \end{bmatrix} \begin{bmatrix} {\boldsymbol{\Phi}^b}^{\mathrm{T}} & \mathbf{0} \\ {\boldsymbol{\Psi}^{b,k}}^{\mathrm{T}} & \mathbf{I} \end{bmatrix} \begin{bmatrix} \mathbf{K}^\delta_{ii,n} & \mathbf{K}^\delta_{ib,n} \\ \mathbf{K}^\delta_{bi,n} & \mathbf{K}^\delta_{bb,n} \end{bmatrix} \begin{bmatrix} \boldsymbol{\Phi}^b & \boldsymbol{\Psi}^{b,k} \\ \mathbf{0} & \mathbf{I} \end{bmatrix} \begin{bmatrix} \mathbf{q}^k_{\Phi,n} \\ \mathbf{q}^k_{\Psi,n} \end{bmatrix} \right\} \mathbf{p}^r_\Phi \tag{A.36}$$

$$= {\boldsymbol{\Phi}^r}^{\mathrm{T}} \mathbf{f}^r.$$

This can be expanded as

$$-\omega^2 \left\{ \mathbf{I} + \sum_{n=1}^{N} \begin{bmatrix} {\mathbf{q}^m_{\Phi,n}}^{\mathrm{T}} & {\mathbf{q}^m_{\Psi,n}}^{\mathrm{T}} \end{bmatrix} \begin{bmatrix} {\boldsymbol{\Phi}^b}^{\mathrm{T}} \mathbf{M}^\delta_{ii,n} \boldsymbol{\Phi}^b & {\boldsymbol{\Phi}^b}^{\mathrm{T}} \mathbf{M}^\delta_{ii,n} \boldsymbol{\Psi}^b + {\boldsymbol{\Phi}^b}^{\mathrm{T}} \mathbf{M}^\delta_{ib,n} \\ \left({\boldsymbol{\Phi}^b}^{\mathrm{T}} \mathbf{M}^\delta_{ii,n} \boldsymbol{\Psi}^b + {\boldsymbol{\Phi}^b}^{\mathrm{T}} \mathbf{M}^\delta_{ib,n} \right)^{\mathrm{T}} & {\boldsymbol{\Psi}^b}^{\mathrm{T}} \mathbf{M}^\delta_{ii,n} \boldsymbol{\Psi}^b + {\boldsymbol{\Psi}^b}^{\mathrm{T}} \mathbf{M}^\delta_{ib,n} + {\mathbf{M}^\delta_{ib,n}}^{\mathrm{T}} \boldsymbol{\Psi}^b + \mathbf{M}^\delta_{bb,n} \end{bmatrix} \begin{bmatrix} \mathbf{q}^m_{\Phi,n} \\ \mathbf{q}^m_{\Psi,n} \end{bmatrix} \right\} \mathbf{p}^s_\Phi + \tag{A.37}$$

$$(1 + j\gamma) \left\{ \boldsymbol{\Lambda}^s + \sum_{n=1}^{N} \begin{bmatrix} {\mathbf{q}^k_{\Phi,n}}^{\mathrm{T}} & {\mathbf{q}^k_{\Psi,n}}^{\mathrm{T}} \end{bmatrix} \begin{bmatrix} {\boldsymbol{\Phi}^b_o}^{\mathrm{T}} \mathbf{K}^\delta_{ii,n} \boldsymbol{\Phi}^b & {\boldsymbol{\Phi}^b_o}^{\mathrm{T}} \mathbf{K}^\delta_{ii,n} \boldsymbol{\Psi}^b + {\boldsymbol{\Phi}^b_o}^{\mathrm{T}} \mathbf{K}^\delta_{ib,n} \\ \left({\boldsymbol{\Phi}^b}^{\mathrm{T}} \mathbf{K}^\delta_{ii,n} \boldsymbol{\Psi}^b + {\boldsymbol{\Phi}^b}^{\mathrm{T}} \mathbf{K}^\delta_{ib,n} \right)^{\mathrm{T}} & {\boldsymbol{\Psi}^b}^{\mathrm{T}} \mathbf{K}^\delta_{ii,n} \boldsymbol{\Psi}^b + {\boldsymbol{\Psi}^b}^{\mathrm{T}} \mathbf{K}^\delta_{ib,n} + {\mathbf{K}^\delta_{ib,n}}^{\mathrm{T}} \boldsymbol{\Psi}^b + \mathbf{K}^\delta_{bb,n} \end{bmatrix} \begin{bmatrix} \mathbf{q}^k_{\Phi,n} \\ \mathbf{q}^k_{\Psi,n} \end{bmatrix} \right\} \mathbf{p}^r_\Phi \tag{A.38}$$

$$= {\boldsymbol{\Phi}^s}^{\mathrm{T}} \mathbf{f}^s, \tag{A.39}$$

where one may note that the mass and stiffness matrices of the cantilevered blade modes are symmetric. If one assumes that the boundary portion of the blade motion is relatively

small, and one ignores the contribution of boundary modes, Eq. A.40 becomes

$$\begin{aligned} -\omega^2 \left[\mathbf{I} + \sum_{n=1}^{N} {\mathbf{q}_{\Phi,n}^{m}}^{\mathrm{T}} {\mathbf{\Phi}^{b}}^{\mathrm{T}} \mathbf{M}_{ii,n}^{\delta} \mathbf{\Phi}^{b} \mathbf{q}_{\Phi,n}^{m} \right] \mathbf{p}_{\Phi}^{r} + \\ (1+j\gamma) \left[\mathbf{\Lambda}^{r} + \sum_{n=1}^{N} {\mathbf{q}_{\Phi,n}^{k}}^{\mathrm{T}} {\mathbf{\Phi}^{b}}^{\mathrm{T}} \mathbf{K}_{ii,n}^{\delta} \mathbf{\Phi}^{b} \mathbf{q}_{\Phi,n}^{k} \right] \mathbf{p}_{\Phi}^{r} \\ = {\mathbf{\Phi}^{r}}^{\mathrm{T}} \mathbf{f}^{r}, \end{aligned} \tag{A.40}$$

where the blade portion of the rogue system normal mode is represented solely using a basis of cantilevered blade normal modes. Finally, one ignores mass mistuning, and approximates ${\mathbf{\Phi}^{b}}^{\mathrm{T}} \mathbf{K}_{ii,n}^{\delta} \mathbf{\Phi}^{b}$ with $\mathbf{\Lambda}_{n}^{\delta,b}$ to obtain

$$-\omega^2 \mathbf{p}_{\Phi}^{r} + (1+j\gamma) \left[\mathbf{\Lambda}^{r} + \sum_{n=1}^{N} {\mathbf{q}_{\Phi,n}^{k}}^{\mathrm{T}} \mathbf{\Lambda}_{n}^{\delta,b} \mathbf{q}_{\Phi,n}^{k} \right] \mathbf{p}_{\Phi}^{r} = {\mathbf{\Phi}^{r}}^{\mathrm{T}} \mathbf{f}^{r}, \tag{A.41}$$

where $\mathbf{\Lambda}_{n}^{\delta,b}$ are the differences in the tuned cantilevered blade eigenvalues from the mistuned cantilevered blade eigenvalues.

BIBLIOGRAPHY

BIBLIOGRAPHY

[1] P. W. Anderson. Absence of diffusion in certain random lattices. *Physical Review*, 109(5):1492–1505, 1958.

[2] C. H. Hodges. Confinement of vibration by structural irregularity. *Journal of Sound and Vibration*, 82(3):411–424, 1982.

[3] D. S. Whitehead. The maximum factor by which forced vibration of blades can increase due to mistuning. *Journal of Engineering for Gas Turbines and Power*, 120(1):115–119, 1998.

[4] Daniel E. Thomson and Joseph T. Griffin. The national turbine engine high cycle fatigue program. *Global Gas Turbine News*, 39(1):14–17, 1999.

[5] J. T. Wagner. Coupling of turbomachine blade vibrations through the rotor. *Journal of Engineering for Power*, 89(3):502–512, 1967.

[6] R. C. F. Dye and T. A. Henry. Vibration amplitudes of compressor blades resulting from scatter in blade natural frequencies. *Journal of Engineering for Power*, 91(3):182–188, 1969.

[7] D. J. Ewins. The effects of detuning upon the forced vibrations of bladed disks. *Journal of Sound and Vibration*, 9(1):65–79, 1969.

[8] D. J. Ewins. A study of resonance coincidence in bladed discs. *Journal of Mechanical Engineering Science*, 12(5):305–312, 1970.

[9] L. E. El-Bayoumy and A. V. Srinivasan. Influence of mistuning on rotor-blade vibrations. *AIAA Journal*, 13(4):460–464, 1975.

[10] J. H. Griffin and T. M. Hoosac. Model development and statistical investigation of turbine blade mistuning. *Journal of Vibration, Acoustics, Stress and Reliability in Design*, 106(2):204–210, 1984.

[11] S.-T. Wei and C. Pierre. Localization phenomena in mistuned assemblies with cyclic symmetry, part i: Free vibrations. *Journal of Vibration, Acoustics, Stress and Reliability in Design*, 110(4):429–438, 1988.

[12] S.-T. Wei and C. Pierre. Localization phenomena in mistuned assemblies with cyclic symmetry, part ii: Forced vibrations. *Journal of Vibration, Acoustics, Stress and Reliability in Design*, 110(4):439–449, 1988.

[13] H. Irretier. Spectral analysis of mistuned bladed disk assemblies by component mode synthesis. In *Vibrations of Bladed Disk Assemblies*, pages 115–125. American Society of Mechanical Engineers, New York, 1983.

[14] M. P. Castanier, G. Óttarsson, and C. Pierre. A reduced order modeling technique for mistuned bladed disks. *Journal of Vibration and Acoustics*, 119(3):439–447, 1997.

[15] R. Bladh, M. P. Castanier, and C. Pierre. Reduced order modeling and vibration analysis of mistuned bladed disk assemblies with shrouds. *Journal of Engineering for Gas Turbines and Power*, 121(3):515–522, 1999.

[16] R. Bladh, M. P. Castanier, and C. Pierre. Component-mode-based reduced order modeling techniques for mistuned bladed disks—part i:theoretical models. *Journal of Engineering for Gas Turbines and Power*, 123(1):89–99, 2001.

[17] R. Bladh, M. P. Castanier, and C. Pierre. Component-mode-based reduced order modeling techniques for mistuned bladed disks—part ii: Application. *Journal of Engineering for Gas Turbines and Power*, 123(1):100–108, 2001.

[18] M.-T. Yang and J. H. Griffin. A reduced-order model of mistuning using a subset of nominal system modes. *Journal of Engineering for Gas Turbines and Power*, 123(4):893–900, 2001.

[19] R. Bladh, C. Pierre, M. P. Castanier, and M. J. Kruse. Dynamic response predictions for a mistuned industrial turbomachinery rotor using reduced-order modeling. *Journal of Engineering for Gas Turbines and Power*, 124(2):311–324, 2002.

[20] F. Moyroud, G. Jacquet-Richardet, and T. Fransson. A comparison of two finite element reduction techniques for mistuned bladed disks. *Journal of Engineering for Gas Turbines and Power*, 124(4):942–952, 2002.

[21] D. M. Feiner and J. H. Griffin. A fundamental model of mistuning for a single family of modes. *Journal of Turbomachinery*, 124(4):597–605, 2002.

[22] S. Lim, R. Bladh, M. P. Castanier, and C. Pierre. A compact, generalized component mode mistuning representation for modeling bladed disk vibration. In *Collection of Technical Papers — AIAA/ASME/ASCE/AHS/ASC Structures, Structural Dynamics and Materials Conference*, volume 2, pages 1359–1380, Reston, VA, 2003. AIAA.

[23] S. Lim, R. Bladh, M. P. Castanier, and C. Pierre. Compact, generalized component mode mistuning representation for modeling bladed disk vibration. *AIAA Journal*, 45(9):2285–2298, 2007.

[24] M. P. Castanier and C. Pierre. Modeling and analysis of mistuned bladed disk vibration: Status and emerging directions. *Journal of Propulsion and Power*, 22(2):384–396, 2006.

[25] M. P. Mignolet and C.-C. Lin. Identification of structural parameters in mistuned bladed disks. *Journal of Vibration and Acoustics*, 119(3):428–438, 1997.

[26] F Pichot, F Thouverez, L Jezequel, and E Seinturier. Mistuning parameters identification of a bladed disk. *Key Engineering Materials*, 204-205:123–132, 2001.

[27] J. Judge, C. Pierre, and S. L. Ceccio. Experimental identification of mistuning in blisks. In *Proceedings of the 6th National Turbine Engine High Cycle Fatigue Conference*, Dayton, OH, 2001. Universal Technology Corporation.

[28] J. Judge, C. Pierre, and S. L. Ceccio. Experimental validation of mistuning identification techniques and vibration predictions in bladed disks. In *Proceedings of the International Forum on Aeroelasticity and Structural Dynamics*, Madrid, Spain, 2001.

[29] J. A. Judge, C. Pierre, and S. L. Ceccio. Mistuning identification in bladed disks. In *Proceedings of the International Conference on Structural Dynamics Modelling*, Madeira, Portugal, 2002.

[30] C. Pierre, J. Judge, S. L. Ceccio, and M. P. Castanier. Experimental investigation of the effects of random and intentional mistuning on the vibration of bladed disks. In *Proceedings of the 7th National Turbine Engine High Cycle Fatigue Conference*, Dayton, OH, 2002. Universal Technology Corporation.

[31] J. A. Judge. *Experimental Investigations of the Effects of Mistuning on Bladed Disk Dynamics*. PhD thesis, The University of Michigan, Ann Arbor, 2002.

[32] D. M. Feiner and J.H. Griffin. A completely experimental method of mistuning identification in integrally bladed rotors. In *Proceedings of the 8th National Turbine Engine High Cycle Fatigue Conference*, pages 1.1–1.13, Dayton, OH, 2003. Universal Technology Corporation.

[33] N. E. Kim and J.H. Griffin. System identification in higher modal density regions of bladed disks. In *Proceedings of the 8th National Turbine Engine High Cycle Fatigue Conference*, pages 1.68–1.82, Dayton, OH, 2003. Universal Technology Corporation.

[34] D.M. Feiner and J.H. Griffin. Mistuning identification of bladed disks using a fundamental mistuning model—part i: Theory. *Journal of Turbomachinery*, 126(1):150–158, 2004.

[35] D.M. Feiner and J.H. Griffin. Mistuning identification of bladed disks using a fundamental mistuning model—part ii: Application. *Journal of Turbomachinery*, 126(1):159–165, 2004.

[36] S. Lim, M. P. Castanier, and C. Pierre. Mistuning identification and reduced-order model updating for bladed disks based on a component mode mistuning technique. In *Proceedings of the 9th National Turbine Engine High Cycle Fatigue Conference*, Dayton, OH, 2004. Universal Technology Corporation.

[37] S.-H. Lim. *Dynamic Analysis and Design Strategies for Mistuned Bladed Disks*. PhD thesis, The University of Michigan, Ann Arbor, April 2005.

[38] Jia Li, C. Pierre, and S. L. Ceccio. Validation of a new technique for mistuning identification and model updating based on experimental results for an advanced bladed disk prototype. In *Evaluation, Control and Prevention of High Cycle Fatigue in Gas Turbine Engines for Land, Sea and Air Vehicles (Meeting Proceedings RTO-MP-AVT-121)*, pages 36–1–36–16, Neuilly-sur-Seine, France, 2005. NATO Research and Technology Organisation.

[39] S. H. Song, M. P. Castanier, and C. Pierre. System identification of multistage turbine engine rotors. In *Proceedings of the ASME Turbo Expo*, volume 5, pages 569–582, New York, 2007. American Society of Mechanical Engineers.

[40] A. Sinha, B. Hall, B. Cassenti, and G. Hilbert. Vibratory parameters of blades from coordinate measurement machine data. *ASME Journal of Turbomachinery*, 130:011013–1 – 011013–8, January 2008.

[41] F. Pichot, D. Laxalde, J. J. Sinou, F. Thouverez, and J. P. Lombard. Mistuning identification for industrial blisks based on the best achievable eigenvector. *Computers & Structures*, 84(29–30):2033–2049, 2006.

[42] Tae W. Lim and Thomas A. L. Kashangaki. Structural damage detection of space truss structures using best achievable eigenvectors. *AIAA Journal*, 32(5):1049–1057, 1994.

[43] R. R. Craig, Jr. and M. C. C. Bampton. Coupling of substructures for dynamic analyses. *AIAA Journal*, 6(7):1313–1319, 1968.

[44] S.-H. Lim, M. P. Castanier, and C. Pierre. Vibration modeling of bladed disks subject to geometric mistuning and design changes. In *Collection of Technical Papers — AIAA/ASME/ASCE/AHS/ASC Structures, Structural Dynamics and Materials Conference*, volume 3, pages 1931–1950, Reston, VA, 2004. AIAA.

[45] V. Ganine, M. Legrand, C. Pierre, and H. Michalska. Efficient component mode synthesis with a new interface reduction method. In *The 12th International Symposium on Transport Phenomena and Dynamics of Rotating Machinery*, Honolulu, Hawaii, 2008. ISROMAC 2008-20158.

[46] V. Ganine, M. Legrand, H. Michalska, and C. Pierre. A sparse preconditioned iterative method for vibration analysis of geometrically mistuned bladed disks. *Computers and Structures*, 87:342–354, 2009.

[47] A. Sinha. Reduced-order model of a bladed rotor with geometric mistuning. *ASME Journal of Turbomachinery*, 131:031007–1 – 031007–7, July 2009.

[48] Alok Sinha. Reduced-order model of a bladed rotor with geometric mistuning. In *Proceedings of the ASME Turbo Expo*, volume 5, pages 307–314, New York, 2007. American Society of Mechanical Engineers.

[49] M. Mbaye, C. Soize, and J. Ousty. A reduced-order model of detuned cyclic dynamical systems with geometric modifications using a basis of cyclic modes. *Journal of Engineering for Gas Turbines and Power*, 132(11):112502, Nov. 2010.

[50] M. Mbaye, C. Soize, J. Ousty, and E. Capiez-Lernout. A reduced-order model of detuned cyclic dynamical systems with geometric modifications using a basis of cyclic modes. In *Proceedings of the XIII International Symposium of Dynamic Problems of Mechanics*, 2009. paper DIN09-0133.

[51] M. Mbaye, C. Soize, J. Ousty, and E. Capiez-Lernout. Robust analysis of design in vibration of turbomachines. In *Proceedings of ASME Turbo Expo 2009*, pages 387–396, June 2009.

[52] D. C. Kammer. Sensor placement for on-orbit modal identifiction and correlation of large space structures. *Journal of Guidance, Control, and Dynamics*, 14(2):251–259, 1991.

[53] J. E. T. Penny, M. I. Friswell, and S. D. Garvey. Automatic choice of measurement locations for dynamic testing. *AIAA Journal*, 32(2):407–414, 1994.

[54] R. R. Craig, Jr. *Structural Dynamics: An Introduction to Computer Methods*, chapter 19. John Wiley & Sons, New York, NY, 1981.

[55] W. C. Hurty. Dynamic analysis of structural systems using component modes. *AIAA Journal*, 3(4):678–685, 1965.

[56] M.-T. Yang and J. H. Griffin. A normalized modal eigenvalue approach for resolving modal interaction. *Journal of Engineering for Gas Turbines and Power*, 119(3):647–650, 1997.

[57] A. Madden, M. Castanier, and B. Epureanu. Reduced-order model construction procedure for robust mistuning identification of blisks. *AIAA*, 46(11):2890–2898, 2009.